Brigham Young University

BYU ScholarsArchive

2012-12-06

Comparison of 3-D Friction Stir Welding Viscoplastic Finite Element Model with Weld Data and Physically-Simulated Data

Maria Posada

Brigham Young University - Provo

Comparison of 3-D Friction Stir Welding Viscoplastic Finite Element Model with Weld Data

and Physically-Simulated Data

Maria Posada

A dissertation submitted to the faculty of
Brigham Young University
in partial fulfillment of the requirements for the degree of

Doctor of Philosophy

Carl D. Sorensen, Chair
Tracy W. Nelson
Timothy W. McLain
Brent W. Webb
Michael P. Miles

Department of Mechanical Engineering

Brigham Young University

November 2012

ABSTRACT

Comparison of 3-D Friction Stir Welding Viscoplastic Finite Element Model with Weld Data
and Physically-Simulated Data

Maria Posada
Department of Mechanical Engineering, BYU
Doctor of Philosophy

Models (both physical and numerical) of the friction stir (FS) welding process are used to develop a greater understanding of the influence of independent process parameters on dependent process output variables, such as torque, power, specific weld energy, peak temperature, cooling rates and various metallurgical factors (e.g., grain size and precipitates). An understanding of how the independent process parameters influence output variables and ultimately their effect on resultant properties (e.g., strength, hardness, etc..) is desirable. Most models developed have been validated primarily for aluminum alloys with relatively small amounts of experimental data. Fewer models have been validated for steels or stainless steels, particularly since steels and stainless steels have proven more challenging to friction stir than aluminum alloys.

The Gleeble system is also a powerful tool with the capability to perform thermomechanical simulations in a known and controlled environment and provide physical representation of resultant microstructure and hardness values. The coupling of experimental data and physical simulated data can be extremely useful in assessing the capabilities of friction stir numerical process models.

The overall approach is to evaluate Isaiah an existing three-dimensional finite element code developed at Cornell University by comparing against experimental and physically-simulated data to determine how well the code output relates to real FS data over a range of nine processing conditions. Physical simulations replicating select thermomechanical streamline histories were conducted to provide a physical representation of resultant metallurgy and hardness. Isaiah shows promise in predicting qualitative trends over a limited range of parameters and is not recommended for use as a predictive tool but rather a complimentary tool, Once properly calibrated, the Isaiah code can be a powerful tool to gain insight into the process, strength evolution during the process and coupled with a texture evolution model may also provide insight into microstructural and texture evolution over a range for which it is calibrated.

ACKNOWLEDGEMENTS

TABLE OF CONTENTS

LIST OF TABLES

LIST OF FIGURES

xiv

1   INTRODUCTION

Beginning shortly after the invention of friction stir welding (FSW) by Wayne Thomas at TWI in 1991, FSW has been modeled extensively. FSW models are becoming increasingly robust as more knowledge and insight into the process is acquired and as more computational capabilities become available. The motivation for continued model development stems from uncertainties associated with the complex nature of the process and the drive to use modeling as a predictive tool to reduce the amount of experimental welding trials to optimize processing parameters to obtain desired mechanical properties.

The high temperatures and strain rates experienced during friction stir (FS) are analogous to other hot deformation processes that have been modeled extensively. With friction stir however, the high temperatures and strain rates are not as homogeneous as those with other hot deformation models. In friction stir, the highest temperatures and strain rates occur at the interface between the tool and the workpiece, i.e., surface(s) and centerline, and decrease as the distance away from these interfaces increase. Although a significant effort by many authors have been dedicated to modeling this process, there are still many aspects by which models can be improved upon but unless proper evaluation and validation is performed, the model is self-limiting.

This effort represents a systematic approach in evaluating a model over a large processing window using a computational model domain that is representative of actual tool size

1

and geometry (convex shoulder and tapered probe design) and processing conditions, i.e., single-sided, partial penetration processing in 304L SS plate. This evaluation is unlike a large number of published papers that evaluate model responses against published data performed by others in aluminum or steels. In those studies, the authors did not describe how well the computational domain matched actual boundary conditions and in some cases, the computational domain was not representative of the physical boundary conditions, such as no backing anvil, tool geometry, workpiece dimensions, among others. The scope of this effort is to determine if Isaiah, a 3-D finite element viscoplastic, is a suitable model for such an undertaking.

1.1 Friction Stir Welding and Processing

Friction stir welding (FSW), invented by TWI in 1991, is a relatively new and revolutionary technology that is now used in manufacturing applications that go beyond its original intent for joining materials.. This process traditionally uses a rotating, non-consumable tool to literally mix one metal into the other as it travels along the seam in solid-state form. This technology offers significant benefits over conventional welding techniques such as reduced distortion, mitigation of fumes, welding or processing of traditional un-welded materials by conventional arc welding and potential for improved properties.

Friction stir processing (FSP), a variant of FSW, is used to locally modify the microstructure for purposes other than joining. Uses for processing include but are not limited to selective alloying, homogenization of microconstituents, redistribution of material to eliminate porosity or inclusions, and property enhancements such as, strengthening, increased ductility, increased fatigue life, desensitization, etc.

2

FSW and FSP are thermal and thermomechanical processes that involve extreme plastic deformation via solid-state stirring of material. The fundamental theory is the same whether used for welding or processing. In both cases, extreme plastic deformation and frictional heating generate sufficient heat to soften the material which allows material to move around the periphery of the tool.

1.2   Objective

The research objectives for this effort are to evaluate the thermal and thermo-mechanical performance of a three-dimensional (3-D) finite element viscoplastic code by comparing simulations output results against output results from experimentally friction stir processed 304 L SS and physically-simulations of controlled thermal and thermomechanical profiles and model streamline thermomechanical histories. The goal is to see how well Isaiah output relates to real FSW data and physically-simulated conditions to determine if the model can be relied upon to predict FSW.

1.3   About this Dissertation

Three major thrust areas, shown in Figure 1-1, are discussed in this dissertation. The thrust areas (experimental, physical simulations and model simulations) are labeled at the top of each column in Figure 1-1 and are discussed in the chapter listed below the thrust area title. Relationships between key input and output variables listed within each trust area are used for evaluation and discussed in their respective chapter. Comparisons are described in Chapter 4.

Each chapter corresponds to a technical paper that has been published or is planned to be published. The following paragraphs provide a brief synopsis of each chapter.

Experimental (FSP) Chapter 2

Input:

Process parameters

300, 400, 500 RPM

2, 4, 6 IPM

Friction stir process

Measureable Outputs
Process-related:
power
x-force
temperature
cooling rate

Microstructural-related:
grain size
hardness (strength)

Predicted (Model) Chapter 4

Input:
Material properites,
 boundry conditions,
process parameters,
300, 400, 500 RPM
2, 4, 6 IPM

non-linear, 3-D FEM

Measureable Outputs
Process-related:
power, x-force
cooling rate
temperature
strain , strain rate
flow stress

Microstructural-related:
hardness (strength)

Physically-Simulated (Gleeble) Chapter 3

Input:
(Strain, strain rate and temperature)

Uniaxial hot compression tests
Constant T and $\dot{\varepsilon}$
Streamline T and $\dot{\varepsilon}$

Measureable outputs
Process-related:
flow stress
peak stress
critical stress

Microstructural-related:
grain size
hardness (strength)

Figure 1-1 Roadmap of three major thrust areas discussed within this dissertation.

Chapter 2 describes the experimental friction stir processing trials conducted.   The measureable process output variables from these experimental trials, such as torque, power, force, temperature, cooling rates, grain size, and hardness were collected, computed, or

characterized. Linear regression analysis is used to develop fitted models that describe the relationship between the process input variables and measured process output variables.

Chapter 3 discusses physical simulations. Physical simulations, in the context of this dissertation, are simply the process by which a specimen is subjected to compression (i.e., deformation) at variable strain rates and temperatures in a machine called the Gleeble. In Chapter 3, a series of physical simulations were conducted at constant strain rates (four in total) to various peak temperatures (three in total). In Chapter 3, looks at trends in flow stress behavior and resultant microstructural development. Linear regression analysis is used to develop relationships, if any, between various flow-stress related variables, such as peak stress or critical stress, to grain size and hardness.

Chapter 4 describes and discusses the model, model simulations and predicted output response variables. In addition, Chapter 4 compares model predictions to experimental friction stir weld data over the nine processing conditions. This chapter also describes the physical simulation of a model streamline and compares its results to those of model predictions. In this experimental design, physical simulations provide a means to evaluate the model's constitutive equations since the Gleeble's boundary conditions are known.

This dissertation provides the following contributions (1) the development of high confidence fitted models for 304L SS (i.e., a material system other than an aluminum alloy) that are valid over a large processing window. These fitted model correlations were developed for spindle torque, spindle power, specific weld energy, cooling rate, peak HAZ temperature, grain size and hardness as a function of process parameters, namely travel and rotational speed, (2) the use of a realistic computational model domain that replicates the actual experimental trials being evaluated against, including a convex shoulder and tapered probe geometry and size, partial

penetration friction stir processing and simulations conducted over a large processing window and (3) the first use of uniaxial compression testing (via Gleeble) to evaluate the an intrinsic friction stir processing material model.

2   FRICTION STIR PROCESS CHARACTERIZATIONS AND DEVELOPMENT OF INDEPENDENT PROCESS PARAMETER RELATIONSHIPS TO DEPENDENT OUTPUT PROCESS VARIABLES

2.1   Abstract

While the physics of friction stir processes is the same across all material systems, the effect of independent variables on key process conditions may differ for different material systems. This chapter characterizes the microstructural and hardness distribution of friction stir processed 304L stainless steel (SS) over the range of processing conditions. Process outputs such as grain size, hardness, peak temperature and cooling rate were obtained. Relationships between independent process variables, rotational and travel speed, and various dependent process output variables were developed using linear regression techniques. High confidence models were developed for spindle torque, spindle power, specific weld energy and cooling rate while those for peak temperature, hardness and grain size had little to no correlation.

2.2   Introduction

A review of the literature, discussed in the next section, shows several studies that have developed and/or evaluated models relating independent processing parameters to output response variables in aluminum alloy systems. Comparable models for steels and stainless steels have not been performed to date.

This chapter describes observed microstructural, property and process response trends over a range of systematically-varied operating conditions in friction stir processed 304L stainless steel (SS). The goal of this chapter is to develop relationships in 304L SS as a function of processing parameters.

2.3 Previous Work

Numerous authors have characterized friction stir welds in various materials including 304L SS. Posada et al. [1], Okamoto et al. [2], Reynolds et al. [3, 4]and Park et al. [5] characterized the microstructure and mechanical properties of 304L stainless steels under FSW conditions. Generally speaking, distinct microstructural regions are observed in a weld cross-section. These regions correspond to the heat-affected zone (HAZ), thermomechanically-heat-affected zone (TMAZ), and stir zone (SZ). Mechanical properties of the weld tend to be higher than base metal properties at the expense of ductility, and hardness traverse measurements show either no change in hardness (perhaps due to static recrystallization) or increasing hardness from the base metal through the HAZ and TMAZ to the center of the SZ. Reynolds [3] performed residual stress measurements and found that the average through-thickness longitudinal stress inside the weld region was approximately the same magnitude as the base metal's yield strength (~300 MPa in tension) in comparison to the weld's transverse residual stress that was approximately 25 MPa in compression. The authors speculated that the relatively symmetric distribution of the stresses about the weld centerline are not due to differences in deformation between the advancing and retreating sides of the weld but rather dominated by its thermal history.

Sterling [6] found that the microstructure produced by friction stir processing of conventionally arc welded 304L SS increased the stress corrosion cracking (SCC) resistivity over standalone arc welded material. He attributed the increased SCC resistance to the modified fine-grained, equiaxed microstructure produced in the SZ, the break-up and reorientation of ferrite stringer characteristic of arc welds, and the introduction of twins. Sterling also discovered that a hard brittle intermetallic, called sigma phase, formed within the SZ region, but speculated that

although sigma is detrimental to SCC, the existence of it was sub-surface and discontinuous and therefore not critical to SCC.

Kokawa et al. [7] investigated the formation of ferrite and sigma phase during friction stir welding. They found that the ferrite was formed during the process and remained as ferrite in the stir zone due to the higher cooling rate associated with the thinner plate. In the thicker plate, the ferrite decomposed to sigma due to differences in cooling rates resulting from differences in the plate thickness.

Park et al. [8] reported banded regions within the stir zone. The banded structures manifested themselves in two distinct forms, similar to those reported by others [5, 9, 10]. The dark banded region of the flow lines appeared as an agglomeration of dark particles that they referred to as "type A" bands. The second type, referred to as "type B" was comprised of highly decorated grain boundaries of a dark etching microconstituent. SEM and TEM analysis confirmed that the dark etching products were sigma phase. The authors speculated that sigma phase was a transformation product from austenite to delta-ferrite with subsequent decomposition of the ferrite to sigma under high strain and dynamic recrystallization conditions.

In a separate study, Park et al. [11] also investigated corrosion properties of FS welded 304 stainless steel, particularly sensitization at the sub-surface grain boundaries due to the formation of deformation induced sigma phase. The authors found that the sigma phase present within the stir zone severely deteriorated the corrosion resistance.

Clark [9] found similar results in underwater friction stir welding runs of 304L SS. Clark reported that the formation of sigma phase is significantly reduced in underwater FS welds as compared to conventional FS welds produced in ambient air and that underwater FSW did not exhibit increased susceptibility to SCC at low concentration of NaCl.

On a more microscopic scale, Sato et al. [12] examined the recrystallization phenomenon that occurs during friction stir welding in 304L stainless steel. The authors conclude that 304L SS undergoes dynamic recrystallization due to severe deformation and high temperatures experienced. They add that the process produces an unequal distribution of dislocation densities within the microstructure but that during subsequent heating from the shoulder during an actual FSW run, those regions of high dislocation density undergo static recrystallization and exhibit a different orientation from the dominant texture components. In a post-weld heat treatment experiment, they observed statically recrystallized grains that exhibited grain growth and twinning, while dynamically recrystallized grains exhibited rotation along with grain growth and twinning.

In addition to microstructural characterization, several authors have attempted to develop relationships between processing parameters and process response variables that would allow them to tailor process response variables such as those described above (i.e., microstructural, mechanical, corrosion, etc.) by manipulating process parameters.

Sato et al. [13] evaluated the effect of tool rotational speed (ranging from 800 to 3600 RPM) at a given travel speed to hardness and microstructure within the weld nugget of 6063 aluminum friction stir welds. The authors reported that the peak temperature at the weld centerline below tool increased with increasing spindle speeds and that the time of the temperature transient was primarily driven by travel speed for all welding conditions examined. They noted that grain growth within the stir zone occurred after all deformation in that region completed. This observation led them to the development of an Arrhenius relationship that correlated grain size and peak temperature.

In 2003, Rhodes et al. [14], found that grain size increased as a function of rotational speed in aluminum. The authors of this study were in agreement with the mechanism described by Sato et al. regarding grain formation as an explanation for their observed results.

Yang et al. [15] found related the increased hardness distributions in stir zones of 2024 and 2524 aluminum alloys to increased weld temperatures. The authors attributed this increase in weld hardness to metallurgical effects of solution heat treatment during the process followed by a natural aging process post-welding.

Hassan et al. [16]observed that in 7010 aluminum FSWs, the grains size varied as a function of power. At low power, smaller grain sizes were observed relative to fabricated at higher power.

Reynolds et al. [17] friction stir welded 7050 aluminum using advance-per-revolution (APR) to develop relationships between weld parameters, hardness distribution and temperature profiles. The authors concluded (in the absence of considering the effects of strain history) that heating and cooling rates were solely a function of travel speed and that the best predictor of peak temperature was power for the set of welds evaluated but did offer a disclaimer that a ranking of peak temperature for a series of welds reliably by only looking at rotational speed, travel speed, APR, weld energy, or even power and that nugget hardness may be reasonably correlated with stir zone peak temperature.

Long et al. [18] performed bead-on-plate welds in a 2xxx, 5xxx, and 7xxx series aluminum alloys at a single travel speed over a range of rotational speeds ranging from approximately 50 to 2000 RPM.   Their experimental results showed an inversely proportional relationship between torque and grain size.

Kayla et al. [19] developed mechanistic models for spindle torque, power and specific weld energy as a function of travel sand rotational speeds for Al F-357 alloy. Numerical results exhibited good agreement against experimental data for spindle torque. The authors found the torque increased with increasing travel speed and decreased with increasing rotational speed. Power was found to be linearly proportional to both rotational and traverse speed and specific weld energy was inversely proportional to travel speed. The authors also found that peak temperature exhibited a linear relationship to weld energy.

Hamilton et al. [20], showed that variations in thermal diffusivity and thickness affect the slope, and by inference, would affect the y-intercept of X-Y linear relationship of parameters being plotted, that being peak temperature and weld energy in his study. Hamilton demonstrated this by plotting the peak temperature as a function of specific weld energy and the normalized peak temperature, i.e., $T_{peak}/T_{solidus}$, as a function of weld energy for various alloys in his study. The authors found that the data arranged itself based on thermal diffusivity and thickness when the peak temperature was normalized.

Cui et al. [21] rightfully points out that the mechanistic model developed by Kalya et al. [19] (and the model used in this study) has limitations since unrealistic values would be obtained as rotational speed approached zero in which case torque goes to infinity or as rotational speeds approached infinity in which case torque would equal zero. Instead, Cui et al. develop an exponential decay model as a function of travel and rotational speeds that exhibits a good fit with experimental data on A356 cast aluminum alloy as well as with other data published in the literature. Power and specific weld energy can be derived from the model that also show good fit over the entire range of rotational values.

The models presented herein are physical but rather experimentally-based and developed for 304L SS over a comprehensive set of processing parameters that comprise the processing envelope for this specific tool design, see Appendix A-1, material and material thickness combinations. Interpolation within this range of processing parameters is acceptable; however, extrapolating outside this range is dangerous and leads to unstable and inadequate metal flow and gross defect formation.

2.4   Experimental Details

2.4.1   Materials

AISI Type 304L SS plates measuring 8 inches wide by 24 inches long with a nominal thickness of 0.25 inch were used for this study. A polycrystalline cubic boron nitride (PCBN) tool was used for all welding trials. The MegaStir tool design is shown in Appendix A-1.

2.4.2   FS Processing Trials

The samples evaluated for the study were extracted from plates FS processed by Owen [22].   Plates instrumented with sixteen 0.032 in (0.8 mm) grounded type K thermocouples at a 0.133 in (3.4 mm) depth from the bottom side of the plate (see Figure 2-1) were placed at 0.157 in (4.0 mm), 0.225 in (5.7 mm), 0.34 in (8.6 mm) and 0.5 in (12.7 mm) from the weld centerline as shown in Figure 2-2. These plates were processed partially through the thickness of the plate over a range of operating conditions that consisted of three different rotational speeds (300, 400 and 500 RPM) and three different traverse speeds (2 IPM [0.85 mm/s], 4 IPM [1.69 mm/s] and 6 IPM [2.54 mm/s]).   A full description of the experimental processing details and thermocouple

techniques is included in reference [22]. Temperature profiles, peak temperature and cooling

rates from 800°C to 500°C were determined from thermocouple data.
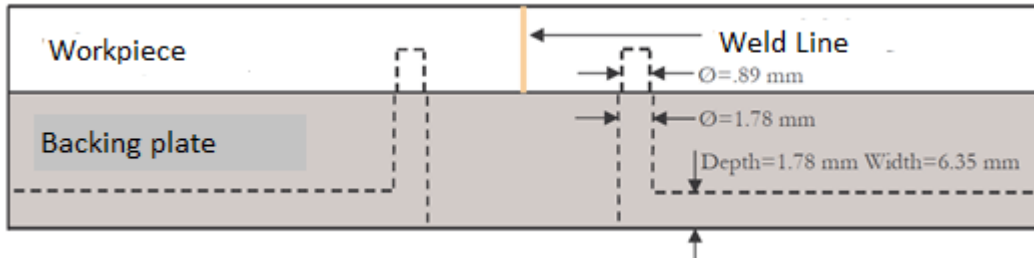
Figure 2-1 Schematic showing the cross-sectional, through-thickness placement of the thermocouples. Photo courtesy of Owen [22].
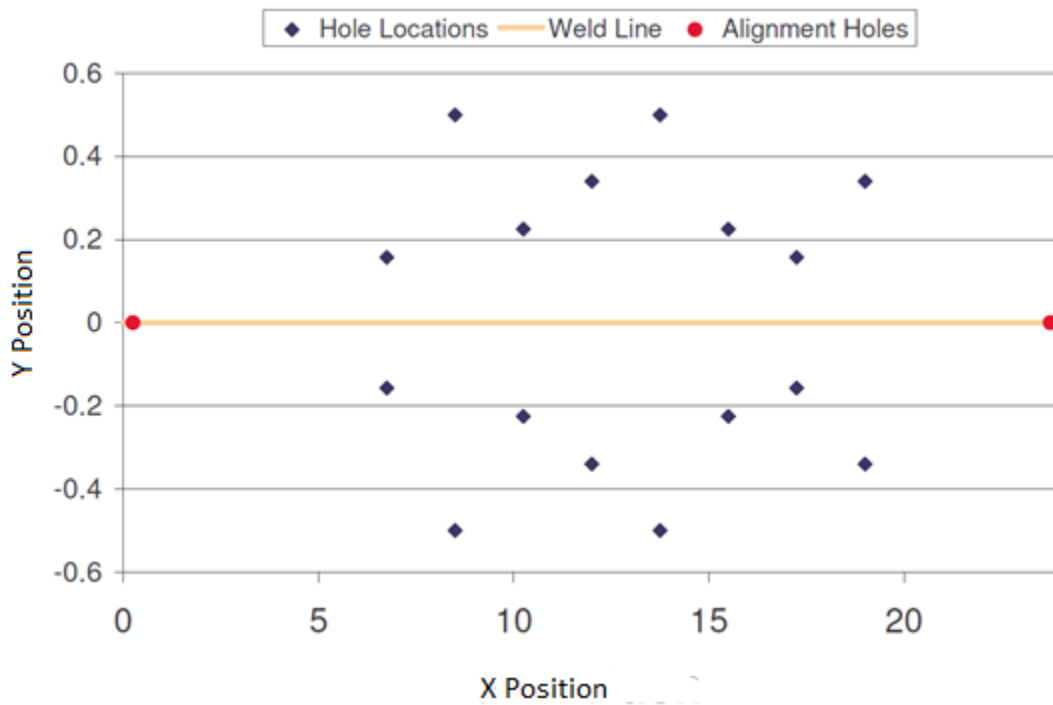
Figure 2-2 Schematic showing the plan view of thermocouple placement relative to the processing path centerline (Y position) and distance along the length of the plate (X position). Photo courtesy of Owen [22].

2.4.3 Chemical Analysis

Specimens from unaffected base material and from one friction stir processed region were sent to Luvak, Inc., an independent analytical testing laboratory, for chemical composition analysis. In addition to analyzing for intentional alloying elements of 304L SS, boron, an alloying element of the FS tool, was included in the analysis. Combustion infrared detection techniques were used for detection of carbon and sulfur, inert gas fusion techniques were used for detection of nitrogen and direct current plasma emission spectroscopy was used to detect all remaining alloying elements.

2.4.4 Metallography and Microhardness Characterization

One representative specimen from the unaffected base metal and one specimen from each of the FS processed regions was sectioned and prepared for metallographic and microhardness characterization. The orientation of the base metal specimen was transverse to the rolling direction and those of the friction stir processed metal were removed transverse to the tool's travel direction. The specimens were mounted in epoxy, metallographically prepared to a 1 μm finish and etched using Luca's reagent (150 mL HCl, 50 mL lactic acid, 3 g oxalic acid) to reveal microstructure and microconstituents.

Grain size was obtained via orientation image microscopy (OIM) in the scanning electron microscope (SEM). The mounted specimens were then re-ground and polished to a 1 μm finish then final polished in a colloidal silica suspension. A 250 x 250 μm area was scanned at the center of each specimen in the SEM using EBSD at a 20 keV accelerating voltage and a step-size of 0.5 μm.

Vicker's microhardness measurements were taken prior to etching at an incremental spacing of 0.250 mm along the through-thickness and transverse directions of the processed region and portions of the adjacent base metal. Pivot plots were generated from the microhardness data to produce a microhardness map showing its distribution across the FS processed nugget and surrounding material. Peak percent hardness and percent hardness of each hardness range in the color key code was calculated using a MATLAB.

2.4.5   Regression Analysis

Regression models were generated to determine best predictors for spindle torque, power, specific weld energy, peak temperature, cooling rate, grain size, and percent peak hardness. Similar to Kayla et al. [19], the general predictive model used for regression analysis uses two independent, correlating variables as expressed in Equation (2-1).

$$Y = A \left[\frac{\omega}{\omega_{max}}\right]^{\alpha} \left[\frac{v}{v_{max}}\right]^{\beta} = A\,\hat{\omega}^{\alpha}\hat{v}^{\beta} \qquad (2\text{-}1)$$

where Y is the response variable, ω is the rotational speed (RPM) , v is the travel speed (IPM), ω_o is the maximum rotational speed, v_{max} is the maximum travel speed, $\hat{\omega}$ is the normalized rotational speed, $\hat{v}_{max}$ is the normalized travel speed, and A, α and β are constants.

The two independent variables selected for this study were rotational speed and travel speed since these are primary control variables assuming all other variables remain constant. These variables are assumed to have no prior relationship with each other and all other processing parameters are assumed to be constant. The independent variables were normalized by their maximum value, i.e., all rotational speeds were divided by 500 RPM and all travel

16

speeds were divided by 6 IPM. The use of unit-less independent variables allows the

relationship to be described in units of the primary regression variable being evaluated.

The least squares regression method requires a linearized relationship between the parameters

and regression variables, thus Equation (2-2) can be expressed as

$$Ln(Y) = Ln(A) + \alpha \cdot Ln(\hat{\omega}) + \beta \cdot Ln(\hat{v}) \tag{2-2}$$

Section 2.5.4 discusses the development of regression models as a function of the independent

variables.

2.5   Results

2.5.1   Bulk Chemical Analysis

Table 2-1 lists the intentional alloying elements of 304L SS plus boron, a primary tool

alloying element, with their corresponding weight percentage. The chemical specification for

this alloy, ASTM A 240/A 240 M is also included for reference. Chemical analysis results do

not show any significant differences between the unaffected base metal and the friction stirred

material and both fall within the specified requirements.

2.5.2   Macro Cross-Sections

Representative macro cross-sections of each of the friction stir processed regions are

shown in Figure 2-3. The grain size measured at the center of each processed is listed in Table

2-2.   The processed regions are typical and show inhomogeneities characteristic of the stirring

nature of the process.

17

Table 2-1 Bulk Chemical Analysis of 304L SS Base Metal and FS Metal

Element	ASTM A 240/A 240M	Base Metal	FS Metal
	wt%	wt%	wt%
Carbon	0.030 max	0.019	0.014
Manganese	2.00 max	1.70	1.72
Silicon	0.75 max	0.28	0.27
Sulfur	0.030 max	0.001	0.001
Phosphorus	0.045 max	0.016	0.025
Nickel	8.0-12.0	8.16	8.58
Molybdenum	--	0.44	0.43
Chromium	18.0-20.0	18.76	18.13
Copper	--	0.29	0.29
Nitrogen	0.10 max	0.087	0.088
Boron	--	0.0048	0.0015

**Table 2-2 Average Grain Size Measured Using OIM at the Center
of the Stir Zone**

Rotational Speed (RPM)	Travel Speed (IPM)	Grain size (μm)
300	2	5.69
400	2	5.5
300	4	6.44
400	4	5.88
500	4	5.09
300	6	6.13

The most evident of these characteristics are more readily observed at higher

magnification. See Figure 2-4 through Figure 2-12.   A few commonalities were observed in all

cross-sections. First, the retreating side exhibits a diffuse interface between the stir zone to the

surrounding metal in contrast to the sharp, delineated interface on the advancing side between

the stir zone and surrounding metal. Second, the top surface in the region where the shoulder

was engaged within the workpiece, dark bands containing highly decorated grain boundaries

and/or dark flow lines are present. Third, microstructurally-distinct flow marks (alternating light

and dark lines) are present on the advancing side. These flow lines partially extend from the

bottom or side of the stirred-zone region towards the top surface.
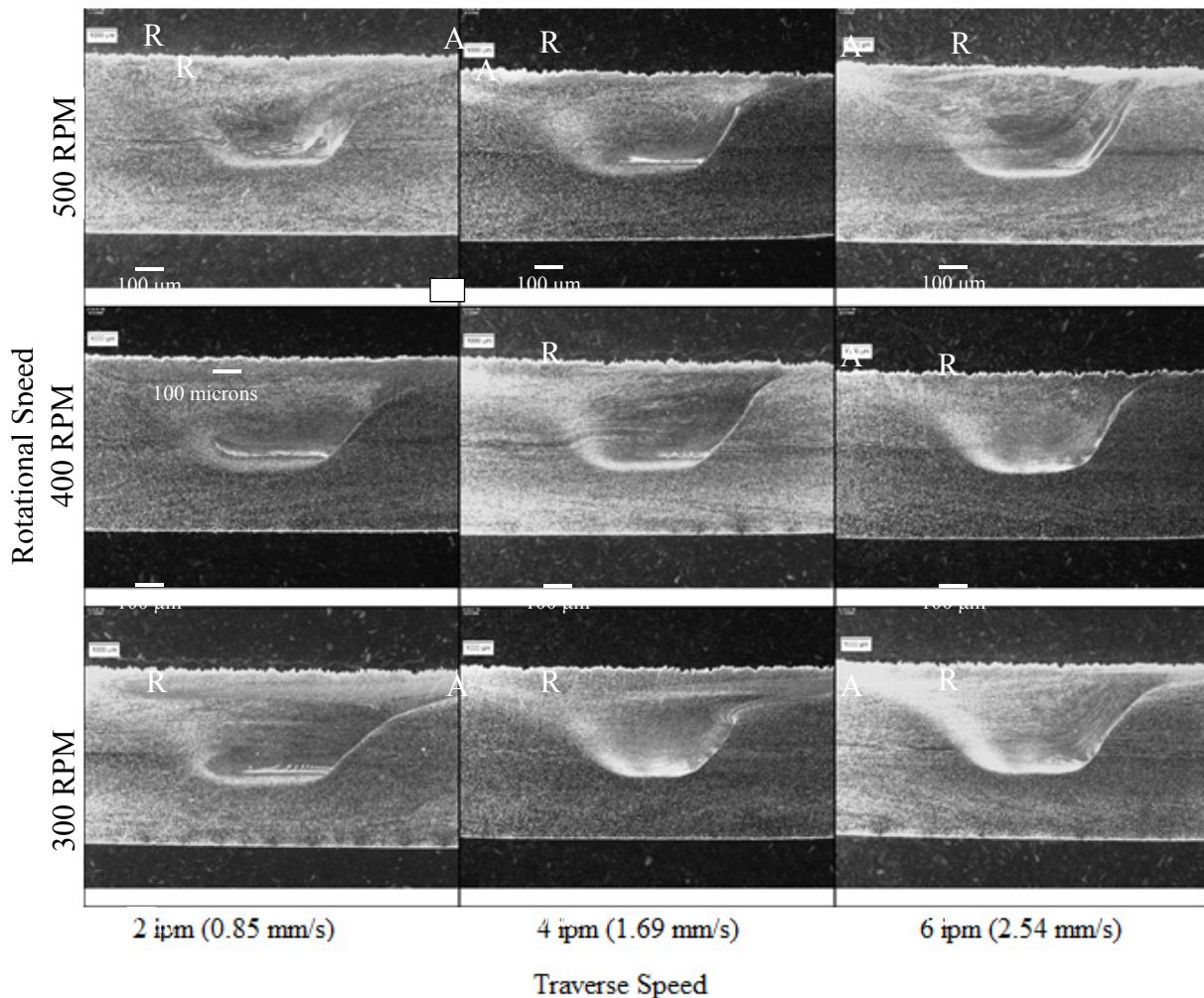
Figure 2-3 Representative macro cross-sections for nine friction stir processing conditions. Photo courtesy of Owen [22]. The retreating side is indicated by R and advancing side is indicated by A on each macro.

In this alloy, these flow patterns are inconsistent within the stir zone over the range of processing conditions. The flow patterns are nonexistent, faint, or turbulent and are either cyclic or random. These cause for these inconsistencies are not the focus of this study, but one can speculate that several factors would produce such variations. These factors include but not limited to (1) colder processing parameters represented by the faster forward travel speeds and slower rotational speeds, (2) worn features on probe resulting in inadequate and variable mixing, or (3) inconsistencies in applied forging forces through the length, (4) variable sectioning locations along the length of the processed path and (5) inconsistency in etching practices and or use of different etchants that reveal different microstructural features. Neither the welding tools nor processed plates are available to fully evaluate these proposed hypotheses.

At higher magnifications, volumetric discontinuities in the stir zone are at the three highest advance-per-revolution parameters. These are 300 RPM, 4 IPM (shown in Figure 2-5) 300 RPM, 6 IPM (shown in Figure 2-6), and 400 RPM, 6 IPM (shown in Figure 2-9). These volumetric discontinuities are located at or below the region previously occupied by the probe.

2.5.3   Microhardness

The microhardness distribution maps are shown in Figure 2-13. The region with an apparent highest hardness is seen at the top surface where the shoulder contacts the workpiece. Other high hardness regions are located on the retreating side and bottom of the stir zone. At the lowest two travel speeds, 2 and 4 IPM, hardness decreases with increasing rotational speed and decreasing travel speed.
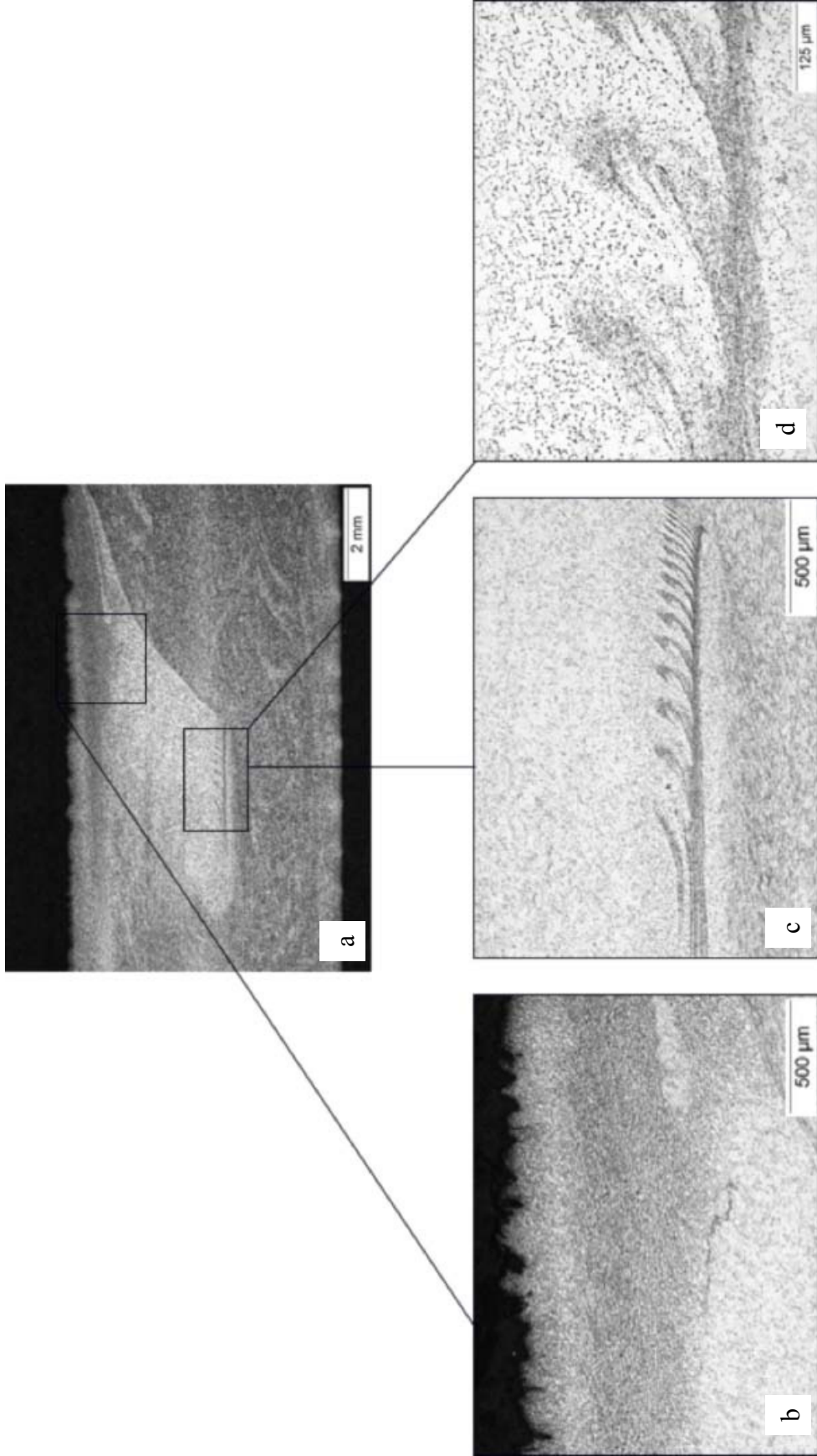
Figure 2-4 (a) Macro cross-section of processed region at 300 RPM and 2 IPM (b) micrograph showing dark flow lines and dark micro-constituents decorating grain boundaries (c) micrograph showing alternating dark and light flow pattern on the advancing side of the stir zone and (d) higher magnification of the flow pattern shown in (c).
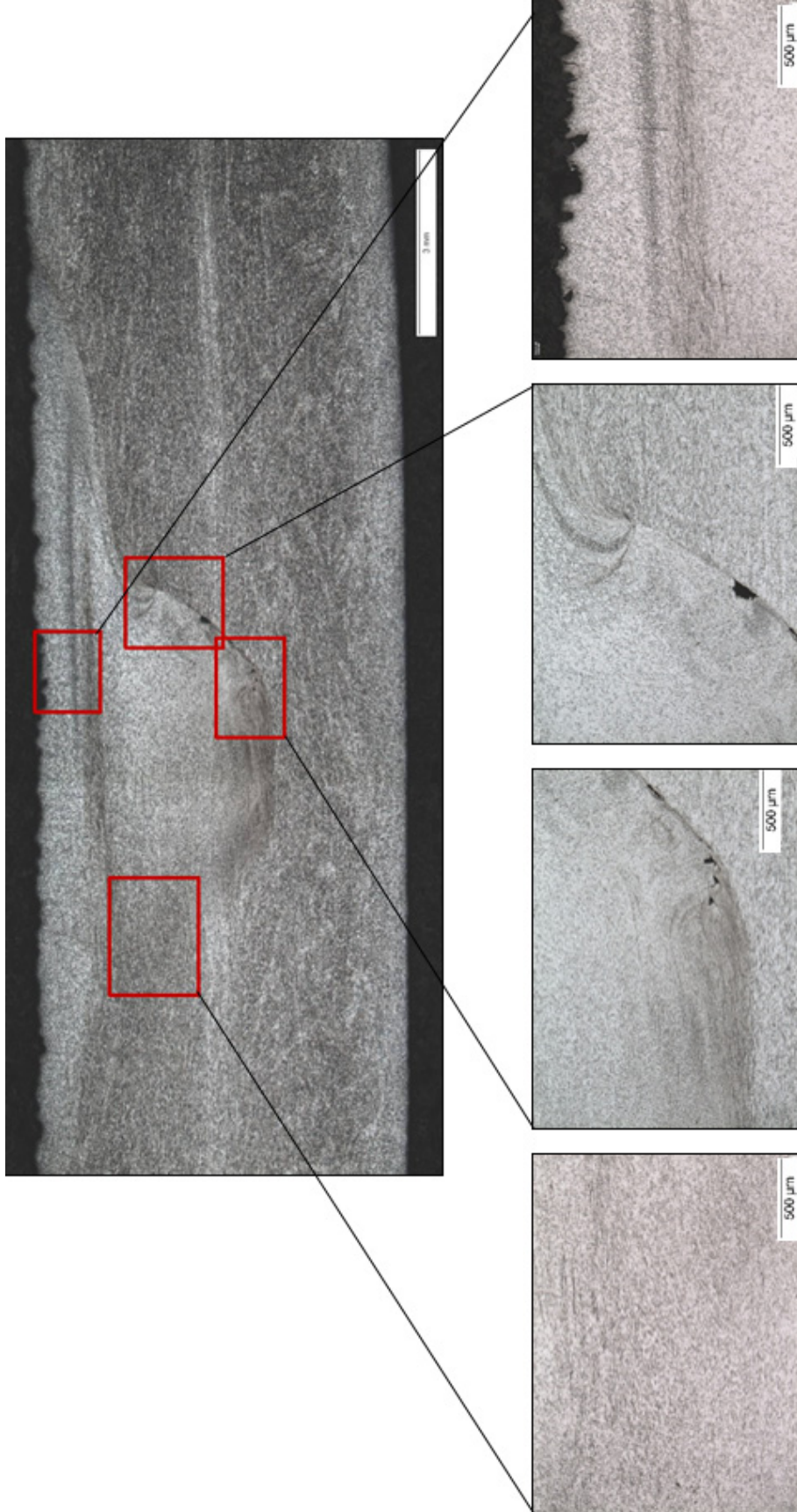
Figure 2-5 **(a) Macro cross-section of processed region at 300 RPM and 4 IPM along with higher magnification micrographs showing (b) diffuse retreating side interface, (c) bottom stir zone region showing small intermittent voids and sharp interface between the stir zone and surrounding material (d) sharp interface on advancing showing upward flow pattern at location where the shoulder and base of the probe meet and (e) darker banding at top surface.**
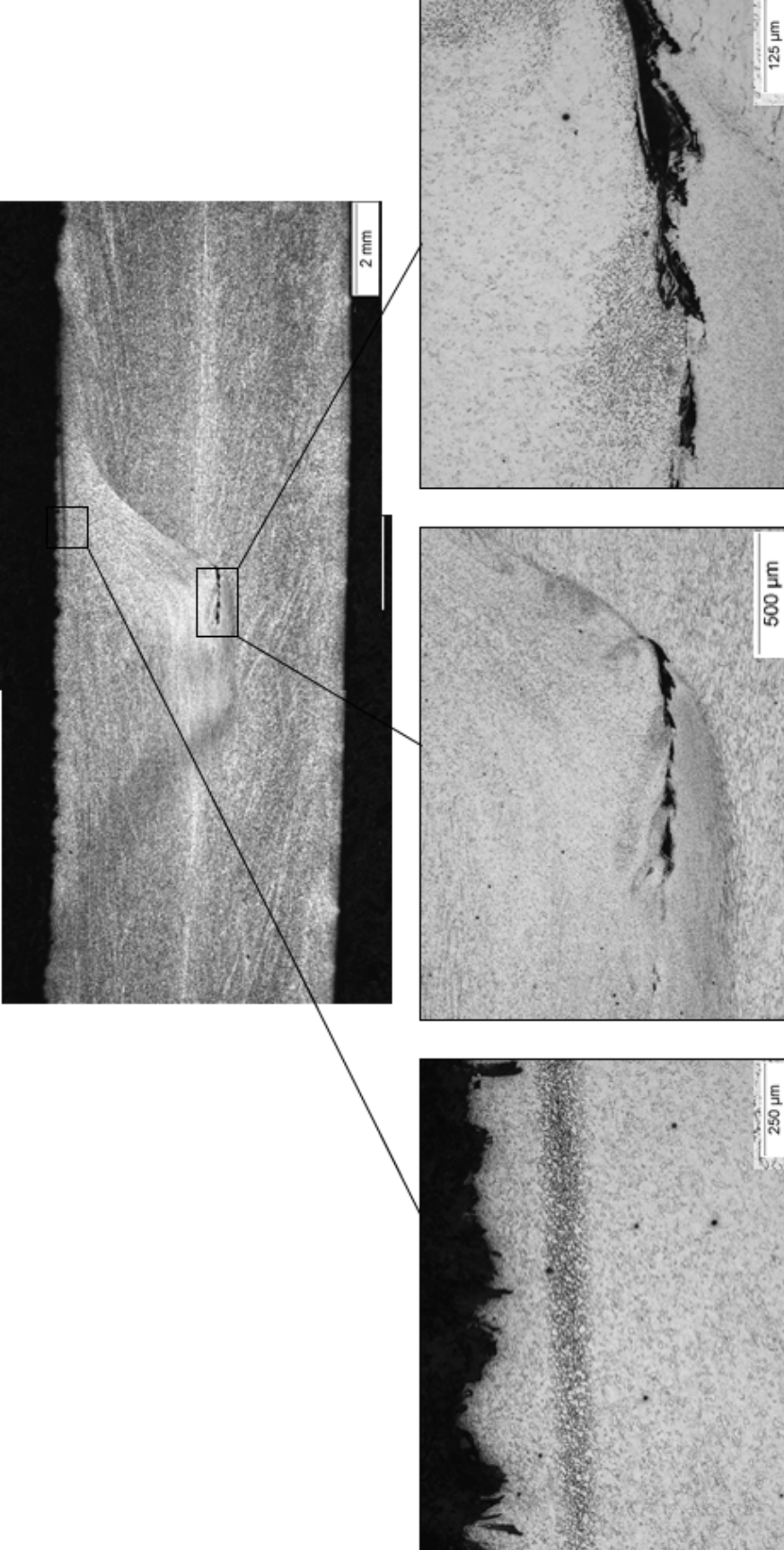
Figure 2-6 (a) Macro cross-section of processed region at 300 RPM and 6 IPM along with higher magnification micrographs showing (b) diffuse interface between retreating side stir zone and surrounding material, (c) flow pattern towards bottom of stir zone, (d) sharp interface between advancing side stir zone region and surrounding material, and (e) band of highly decorated grain boundaries along the top surface.
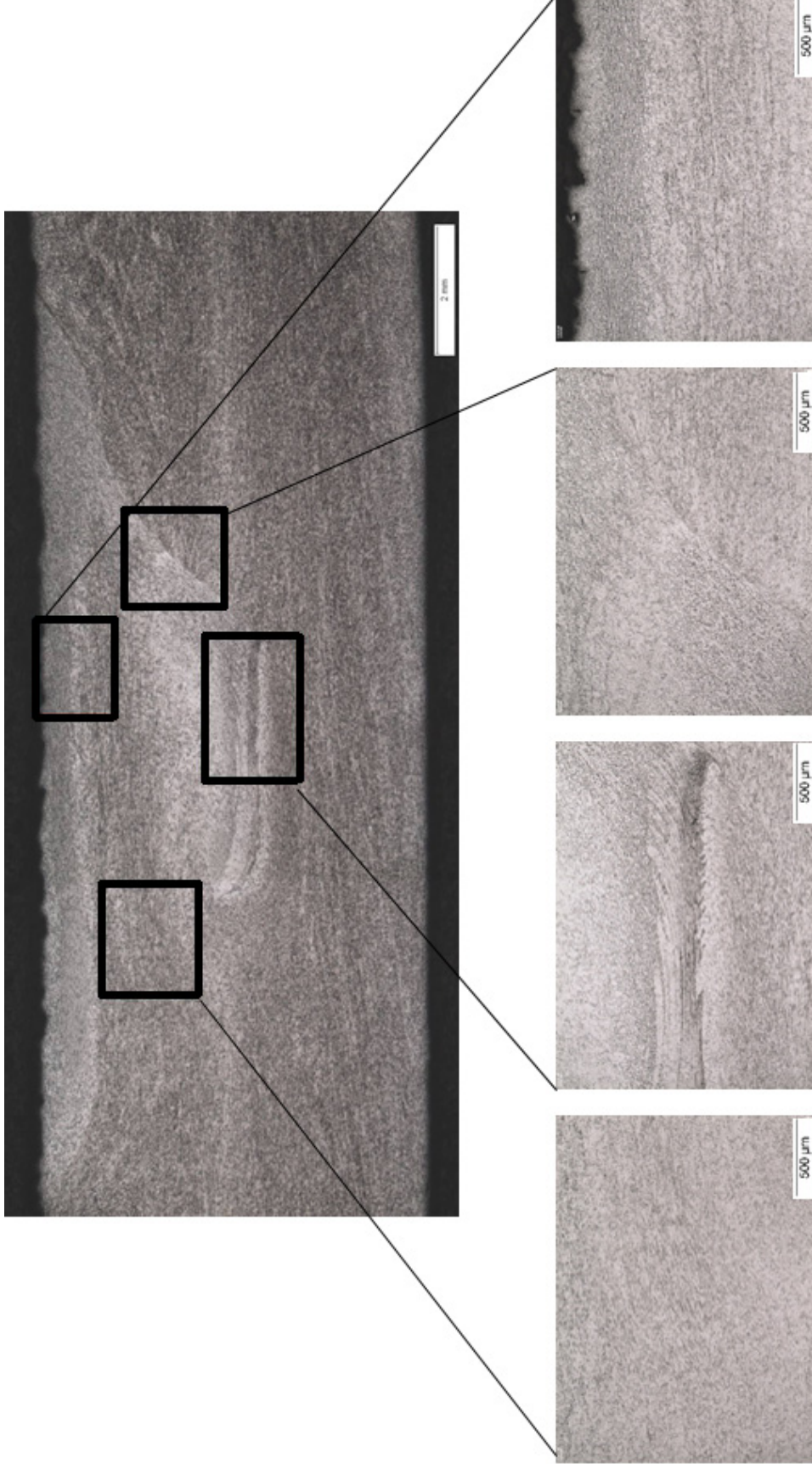
Figure 2-7 (a) Macro cross-section of processed region at 400 RPM and 2 IPM along with higher magnification micrographs showing (b) diffuse interface between retreating side stir zone and surrounding material, (c) flow pattern towards bottom of stir zone, (d) sharp interface between advancing side stir zone region and surrounding material, and (e) band of highly decorated grain boundaries along the top surface.
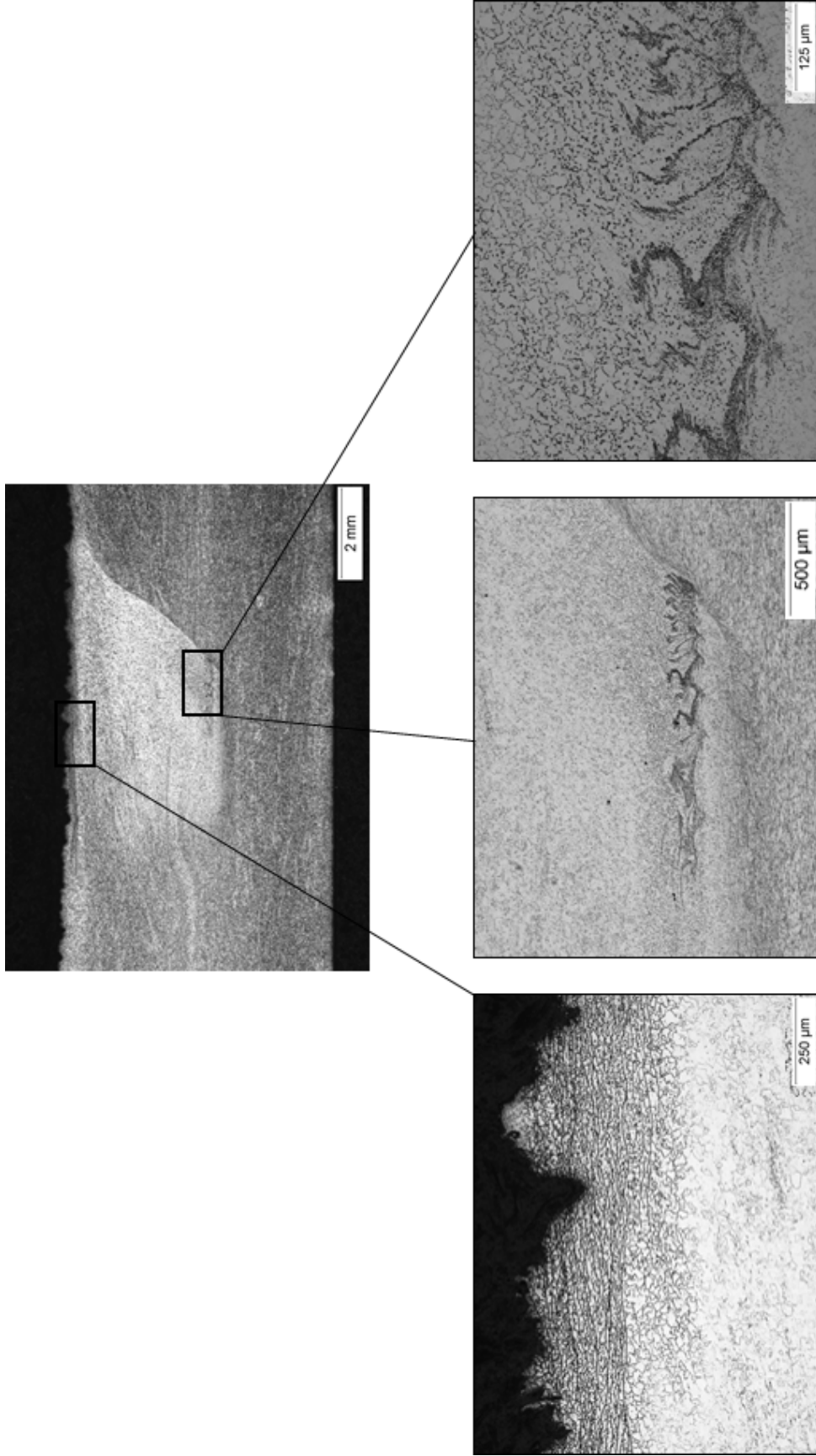
Figure 2-8 (a) Macro cross-section of processed region at 400 RPM and 4 IPM along with higher magnification micrographs showing (b) a band of dark phase microconstituents decorating grain boundaries along the top surface, (c) flow pattern towards bottom of the stir zone region, (d) higher magnification of flow pattern showing dark bands and dark microconstituents decorating boundaries.
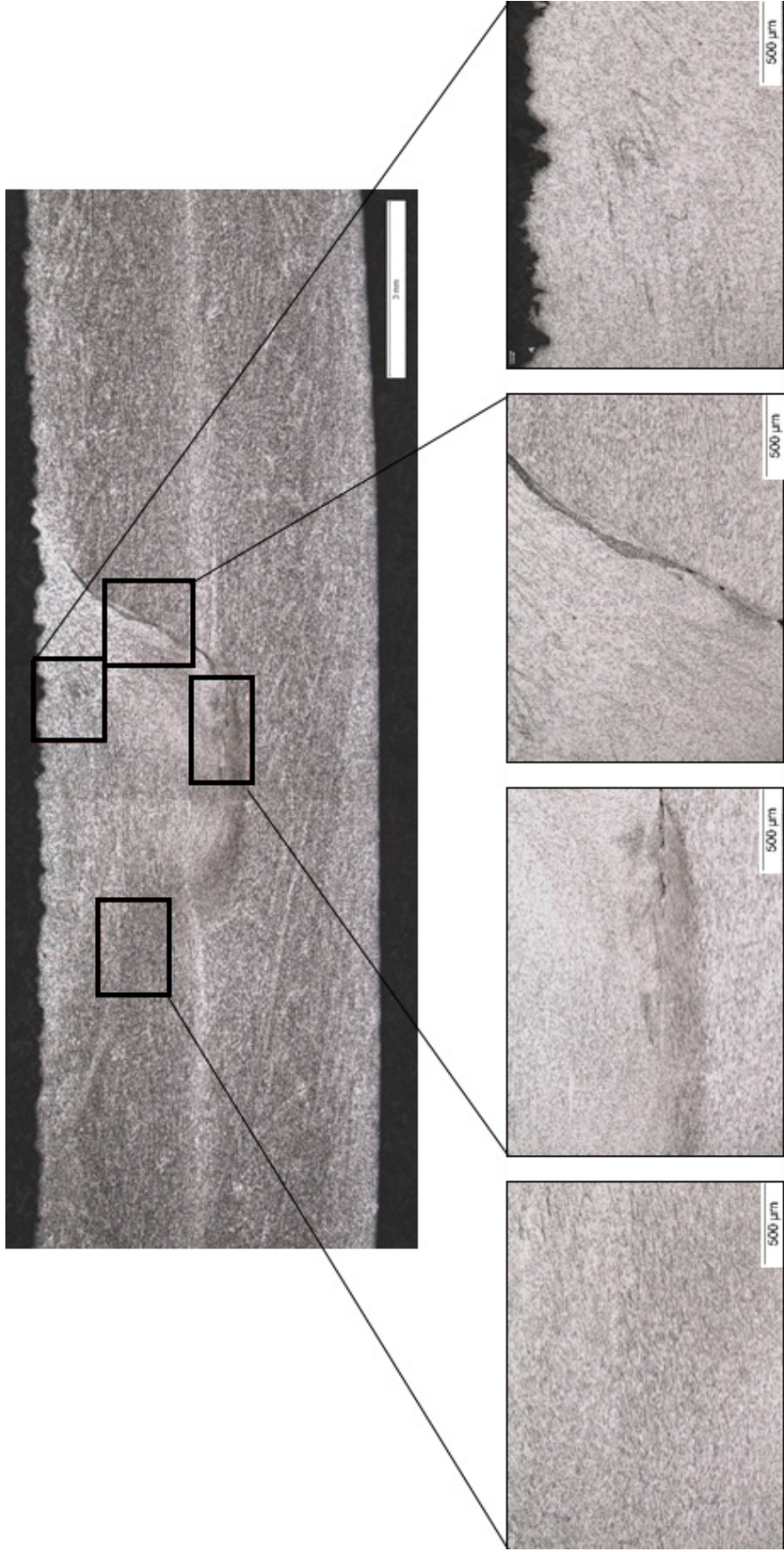
Figure 2-9 (a) Macro cross-section of processed region at 400 RPM and 6 IPM and higher magnification micrographs showing (b) diffuse retreating side interface between stir zone and surrounding material, (c) presence of small intermittent voids towards bottom of stir zone (d) sharp interface and dark band between the advancing side stir zone region and surrounding material and (e) slight zig-zag band of dark phase particles at top surface.
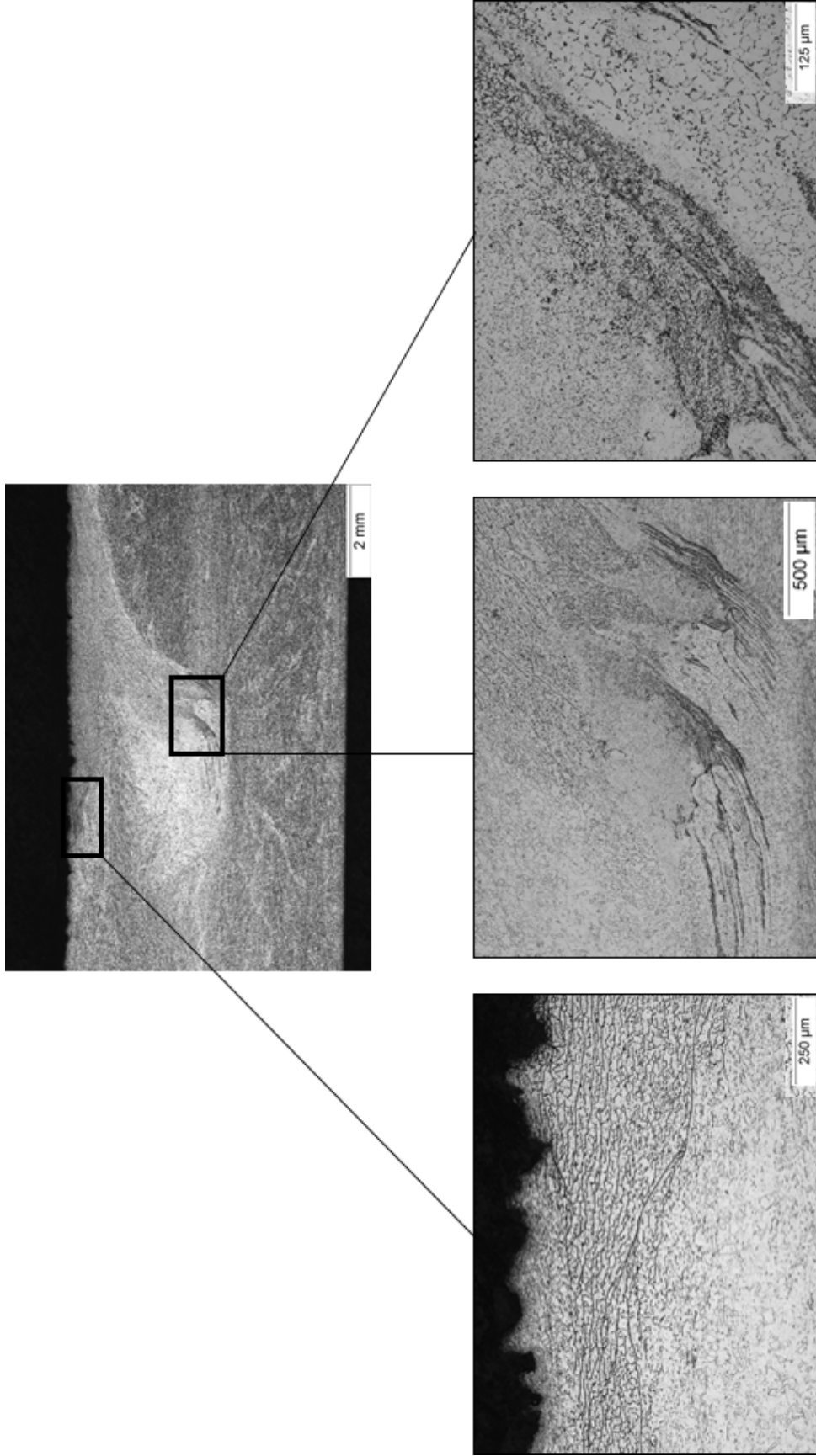
Figure 2-10 **(a) Macro cross-section of processed region at 500 RPM and 2 IPM and higher magnification micrographs showing (b) dark microconstituents decorating grain boundaries along the top surface (c) flow patter towards bottom of stir zone (d) higher magnification of (c) showing both dark banding and dark microcsonstituents decorating grain boundaries.**
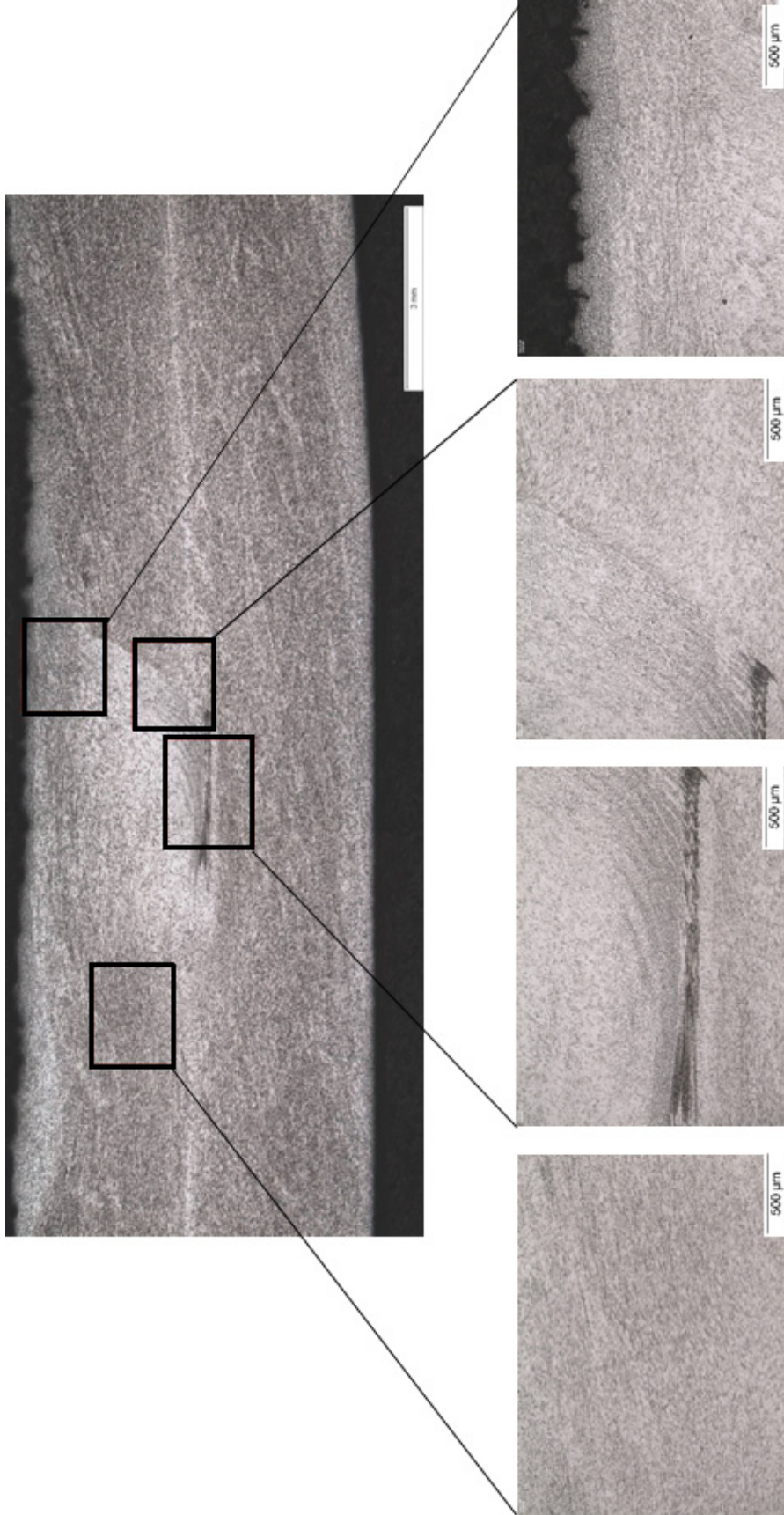
Figure 2-11 (a) Macro cross-section of processed region at 500 RPM and 4 IPM and higher magnification micrographs showing (b) diffuse retreating side interface between stir zone and surrounding material (c) flow pattern towards bottom of stir zone region (d) sharp interface between advancing side stir zone to the surrounding metal.
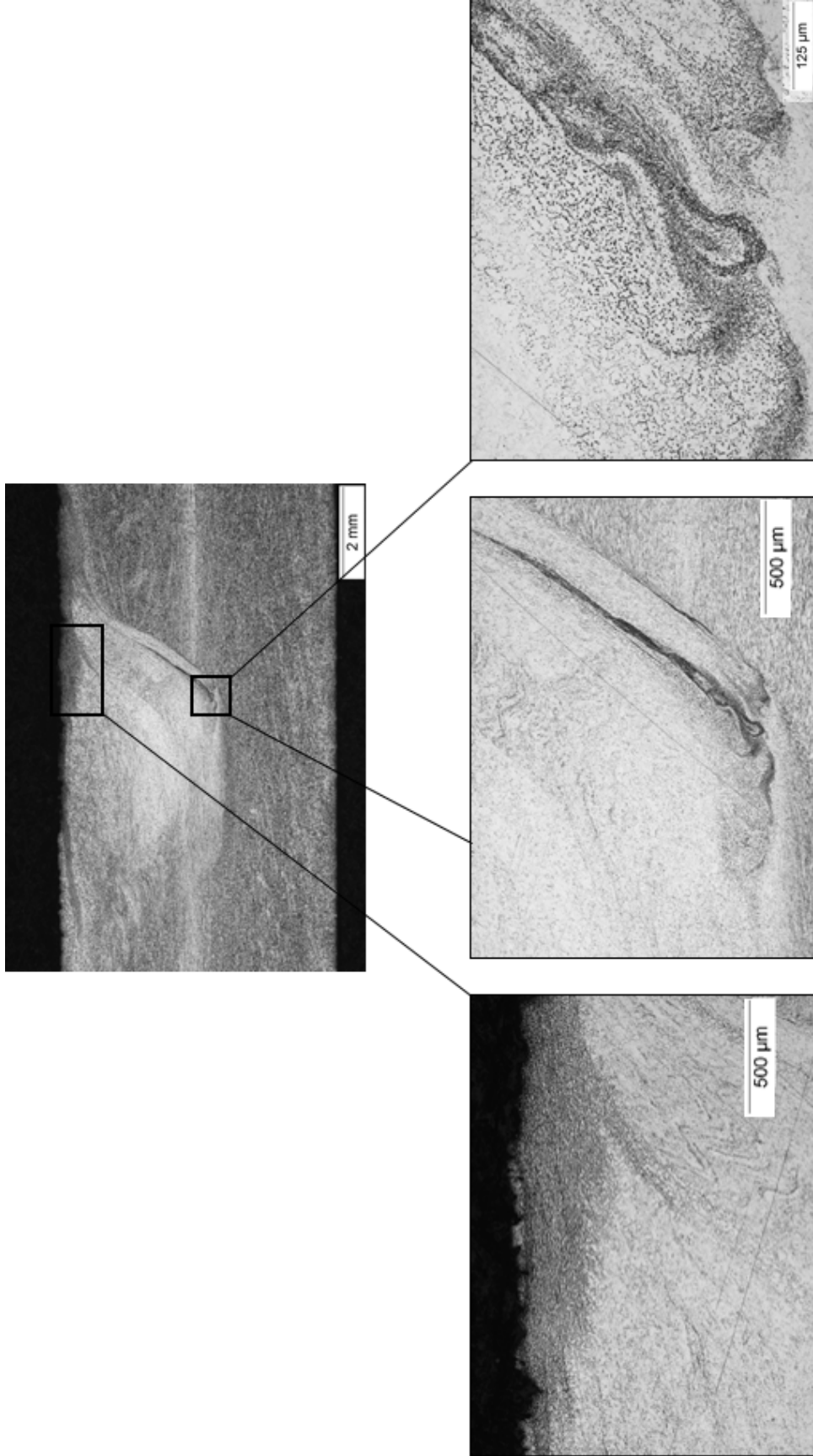
Figure 2-12 (a) Macro cross-section of processed region at 500 RPM and 6 IPM and higher magnification micrographs showing (b) heavy band of dark microconstituents decorating grain bondaries along top surface (c) sharp interface between the stir zone and surrounding metal as well as flow pattern towards bottom of stir zone that extend upward on the advancing side and (d) higher magnification of (c) showing dark banding and dark microconstituents decorating grain boundaries.
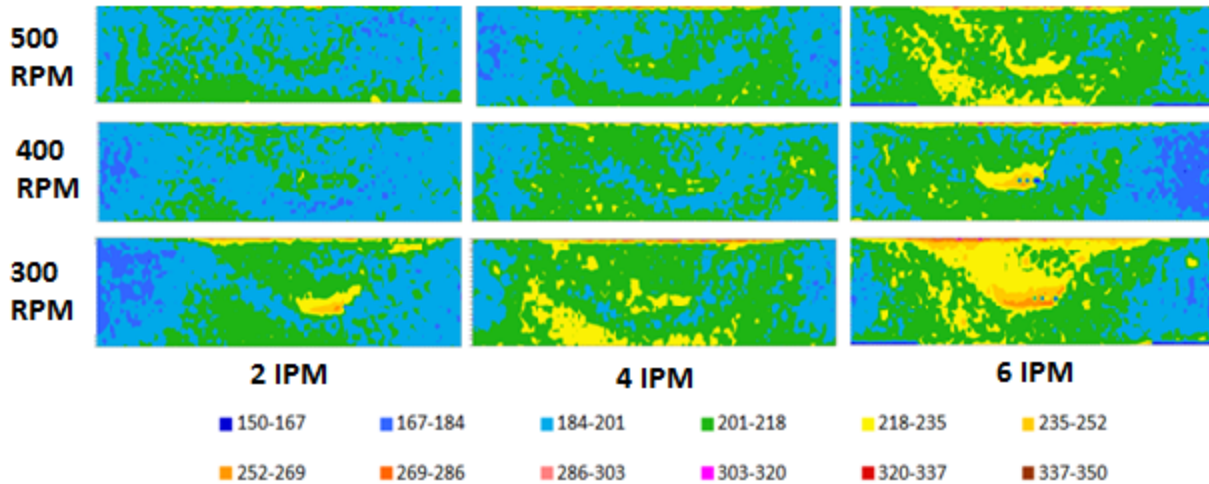
Figure 2-13 Microhardness distribution maps for the nine processing conditions.

In an attempt to make statistical inferences on the hardness data, cumulative distribution function (CDF) and probability density function (PDF) plots were developed. Both analyses were performed on the entire hardness data set which includes the stir zone, thermo-mechanically-affected zone (TMAZ), heat-affected zone (HAZ) and base metal. The CDF is shown in Figure 2-14.

The first, second and third quartiles, corresponding to the 25th, 50th and 75th percentiles were extracted from the CFD plot. These values are listed in Table 2-3. The 50th percentile is plotted in Figure 2-15 (a) as a function of rotational speed and in Figure 2-15 (b) as a function of travel speed. The plots show a polynomial fit ($R^2 = 0.2472$) with respect to both rotational speed and travel speed ($R^2 = 0.4341$). Although the R^2 values are not high, the quantitative trends observed in Figure 2-13 are reflected qualitatively in these plots, i.e., the highest hardness are observed at the highest travel speeds. The intermediate values of travel and rotational speeds are not in line with the remainder of the data set. Figure 2-16 (a) and (b) show the interquartile

range (IQR) plotted as a function of (a) rotational speed and (b) travel speed. The IQR, i.e., the measure of spread of the distribution, increases at higher rotational speed and travel speeds.
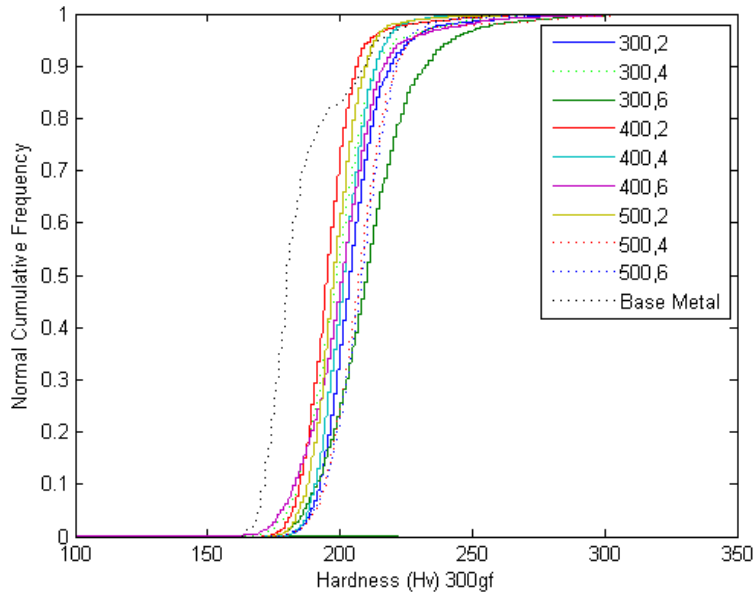
Figure 2-14 Cumulative distribution function (or frequency) for all nine processing conditions and base metal.

Table 2-3 Table Listing the 25th, 50th, 75th and IQR Values for each Distribution Curve

RPM	IPM	25 Percentile	50 Percentile	75 Percentile	IQR
300	2	197.7	203.3	210.3	12.6
300	4	191.2	198.8	206.6	15.4
300	6	199.9	210.2	220.2	20.3
400	2	189.3	195.5	200.9	11.6
400	4	195.5	201	207.8	12.3
400	6	192.3	201	209	16.7
500	2	192.3	197.7	203.3	11
500	4	199.9	206.7	213.8	13.9
500	6	201	207.9	215.1	14.1
Base Metal		175	180	190	15

31
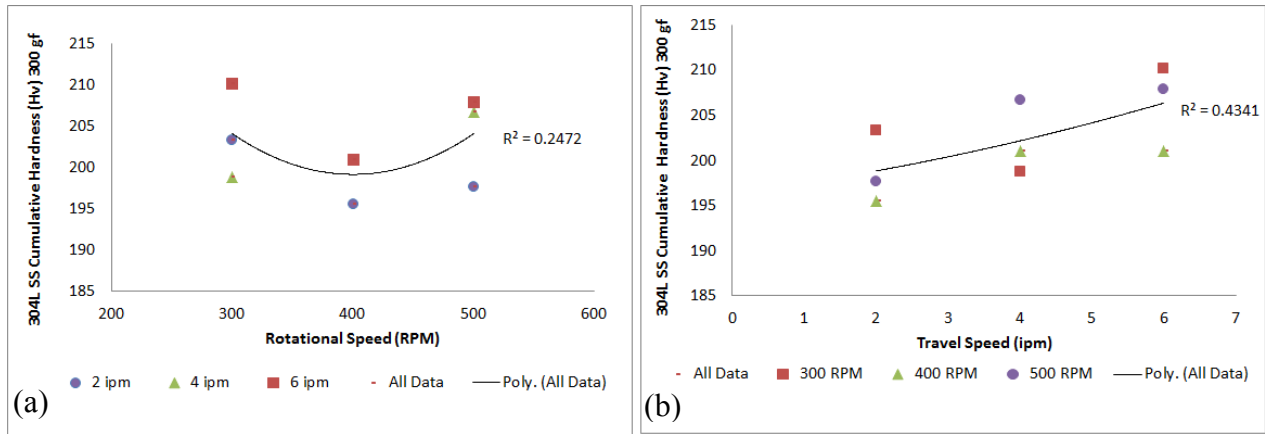
Figure 2-15 Percentile cumulative hardness as function of (a) rotational and (b) travel speed.
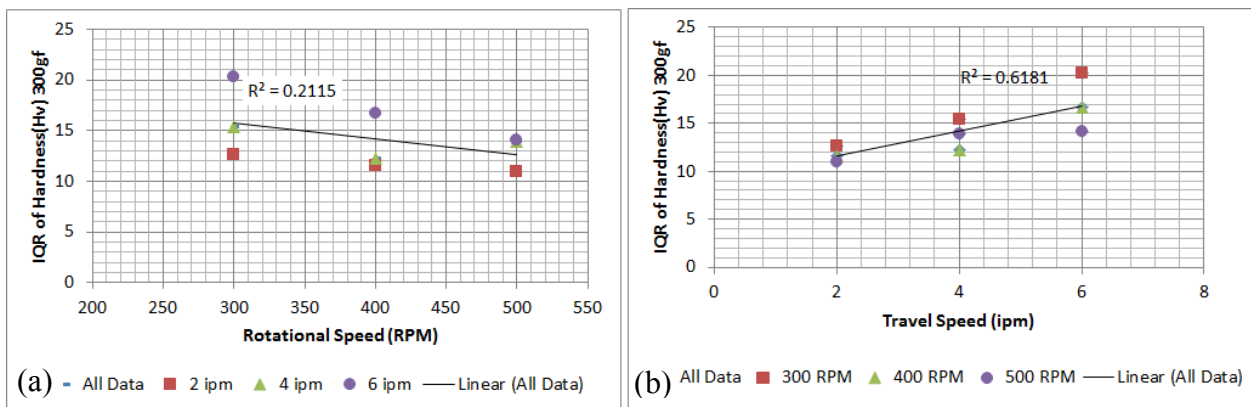
Figure 2-16 Interquartile range (IQR) plotted as a function of (a) rotational speed and (b) travel speed.

A final regression analysis was performed to describe the mean cross-sectional hardness as a function of normalized rotational speed and normalized travel speed. The summary results, shown in Appendix A-20 indicate a poor correlation ($R^2 = 0.3337$). These results suggest that other unknown variables which fall outside the scope of this program affect hardness.

2.5.4 Regression Analysis

As discussed in Section 2.4.5, regression models were developed for spindle torque, peak temperature, cooling rate, percent peak hardness and grain size as a function of rotational and travel speed. However, since rotational speed and travel speed are not independent of spindle power and specific weld energy, linear regression analysis was not used to model their relationships to process parameters. Instead, the models for these output process variables were generated using the model for spindle torque as a function of rotational and travel speed and constitutive relationships for spindle power and specific weld energy. The following paragraphs describe their model development.

Spindle torque, expressed in Equation (2-3), can be modeled as a function of rotational and travel speed and spindle power can be related to spindle torque as expressed in Equation (2-4).

$$\tau_s = A_\tau \left[\frac{\omega}{\omega_{max}} \right]^{\alpha_\tau} \left[\frac{v}{v_{max}} \right]^{\beta_\tau} = A_\tau \, \hat{\omega}^{\alpha_\tau} \hat{v}^{\beta_\tau} \tag{2-3}$$

where τ_s is spindle torque, A_τ, α_τ, and β_τ are the regression coefficients for spindle torque.

$$P = \omega \tau_s \tag{2-4}$$

where ω is the rotational speed and τ_s is spindle torque as expressed in Equation (2-3).

Substituting Equation (2-3) into Equation (2-4), the relationship for power can be modeled as a function of process parameters as expressed in Equation (2-5).

$$P = \omega \left[A_\tau \left(\frac{\omega}{\omega_{max}} \right)^{\alpha_\tau} \left(\frac{v}{v_{max}} \right)^{\beta_\tau} \right] = A_\tau \, \omega_{max} \left(\frac{\omega}{\omega_{max}} \right)^{\alpha_\tau+1} \left(\frac{v}{v_{max}} \right)^{\beta_\tau} = A_\tau \, \omega_{max} \hat{\omega}^{\alpha_\tau+1} \hat{v}^{\beta_\tau} \tag{2-5}$$

Similarly, by dividing Equation (2-5) by the velocity of the heat source, specific weld energy can be expressed in terms of processing parameters as shown in Equation (2-6).

$$E_{specific} = \frac{\omega \tau_s}{v} = \frac{P}{v} = A_\tau \left(\frac{\omega_{max}}{v_{max}} \right) \left(\frac{\omega}{\omega_{max}} \right)^{\alpha_\tau+1} \left(\frac{v}{v_{max}} \right)^{\beta_\tau-1} = A_\tau \left(\frac{\omega_{max}}{v_{max}} \right) \hat{\omega}^{\alpha_\tau+1} \hat{v}^{\beta_\tau-1} \tag{2-6}$$

The coefficient values for A_τ, α_τ and β_τ were obtained and substituted into their respective equations in the next section.

2.5.4.1 Spindle Torque

Spindle torque was calculated using the measured output spindle power and associated rotational speed and solving for τ_s in Equation (2-4). The value for spindle power is calculated by taking the difference between the measured spindle power and the spindle power associated with spindle's free rotation in air. Linear regression analysis relating spindle torque to rotational and travel speed is summarized in Appendix A-2. The coefficients obtained from this analysis are A_τ= 4.118, α_τ = -0.423, and β_τ = 0.263. Thus, the relationship for spindle torque as a function of travel speed and rotational speed by linear regression becomes

$$\tau_s = 4.118 v^{0.263} \omega^{-0.423} \tag{2-7}$$

The R^2 value is 0.9823. A plot showing predicted vs. average measured spindle torque is shown in Figure 2-17. The model for spindle torque shows a high measure of goodness-of-fit. The model for spindle torque in Equation (2-7) agrees with the mechanistic model for robotic friction stir welded Al-F357 investment castings developed by Kalya et al. [19]. For Al-F357, the spindle torque model developed by [19] is shown in Equation(2-8).

$$\tau_s = 399.87 \ v^{0.165} \omega^{-0.848} \tag{2-8}$$

The coefficients in Equation (2-8) for aluminum are different than those obtained in Equation (2-7) for 304L SS. The differences in the coefficient may be attributable to differences in thermophysical properties and thickness variations since the amount of heat generated, the material's ability to conduct heat, and the distance over which that heat must travel will govern

the amount of force necessary to rotate material around the tool. In both models, spindle torque is affected more by changes in rotational speed than changes in travel speed, although to a lesser degree in 304L SS.
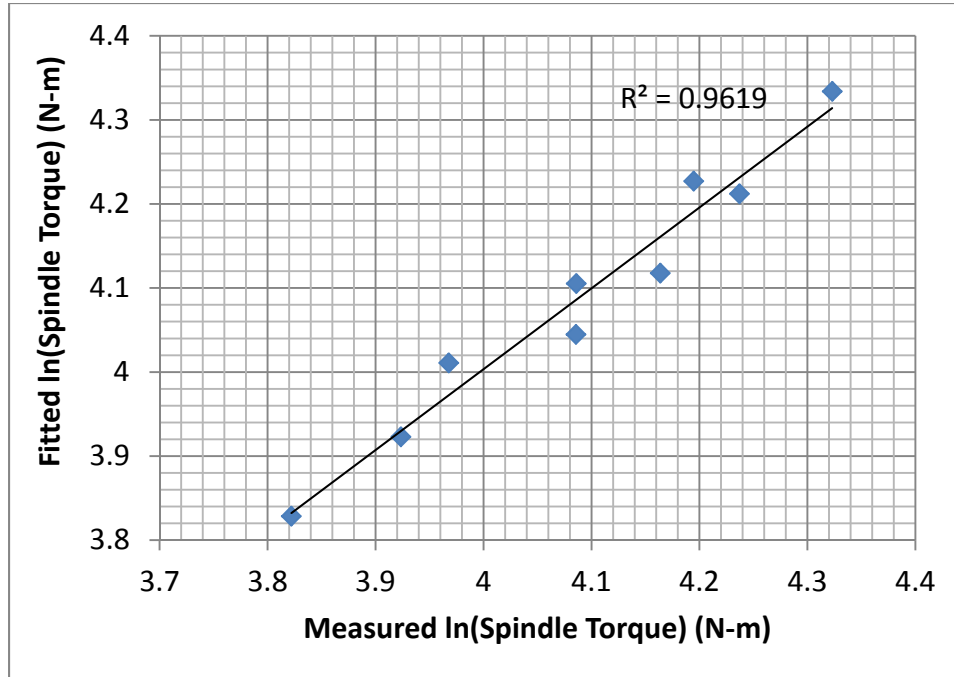
Figure 2-17 Fitted model versus measured spindle torque.

Figure 2-18 shows that spindle torque decreases as rotational speed increases and that at a given rotational speed, spindle torque decreases as travel speed decreases. The highest spindle torque values are observed at the highest travel speeds and lowest rotational speeds. Figure 2-18 shows spindle torque increasing with increasing travel speed.
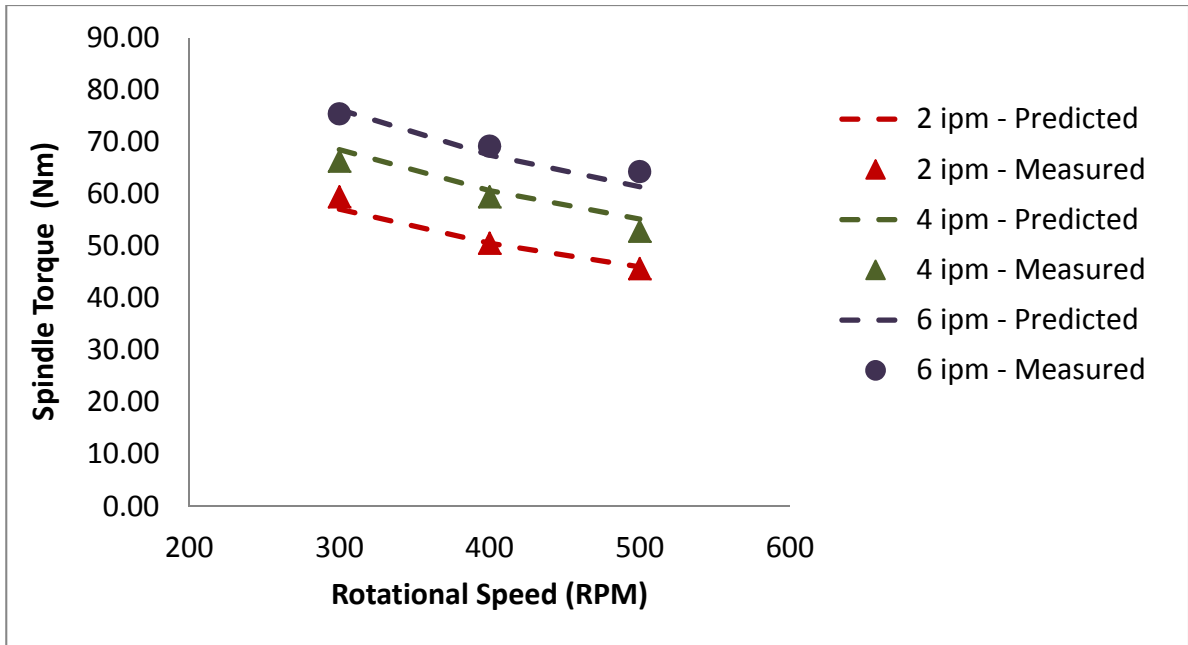
Figure 2-18 Spindle torque as a function of rotational speed.
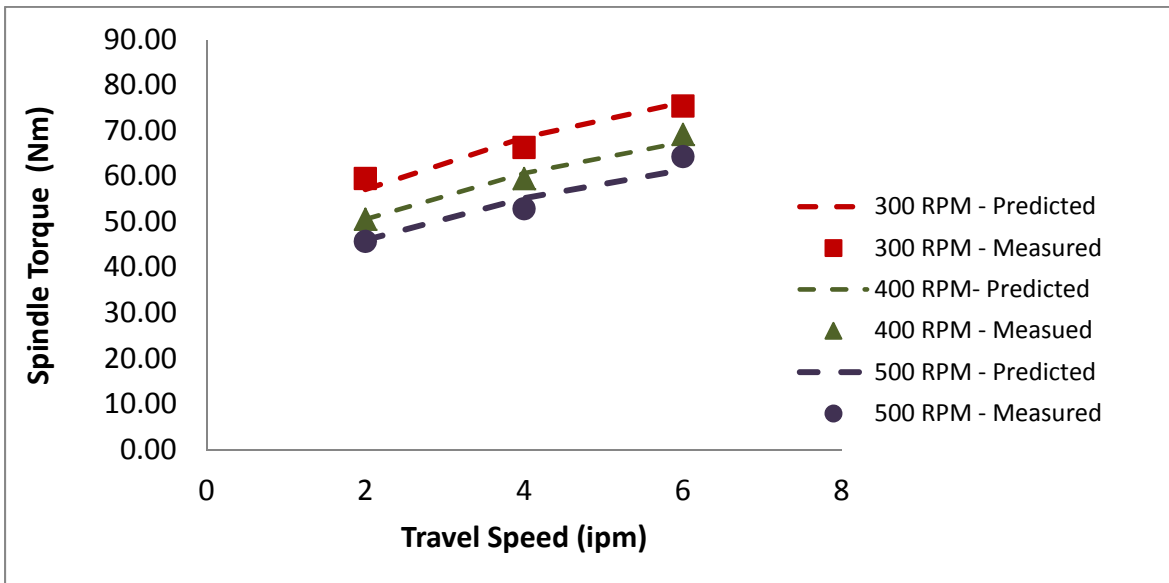
Figure 2-19 Spindle torque as a function of travel speed.

36

2.5.4.2 Spindle Power

Substituting the relationship developed for spindle torque, Equation (2-7), into Equation (2-5), power can be described in terms of rotational and travel speed as shown in Equation (2-9).

$$P = 4.117\omega^{-0.423+1}v^{0.263} = 4.117\omega^{0.577}v^{0.263} \tag{2-9}$$

Figure 2-20 shows that the predicted spindle power over the range of operating conditions has a good linear fit against the measured data ($R^2 = 0.9705$).
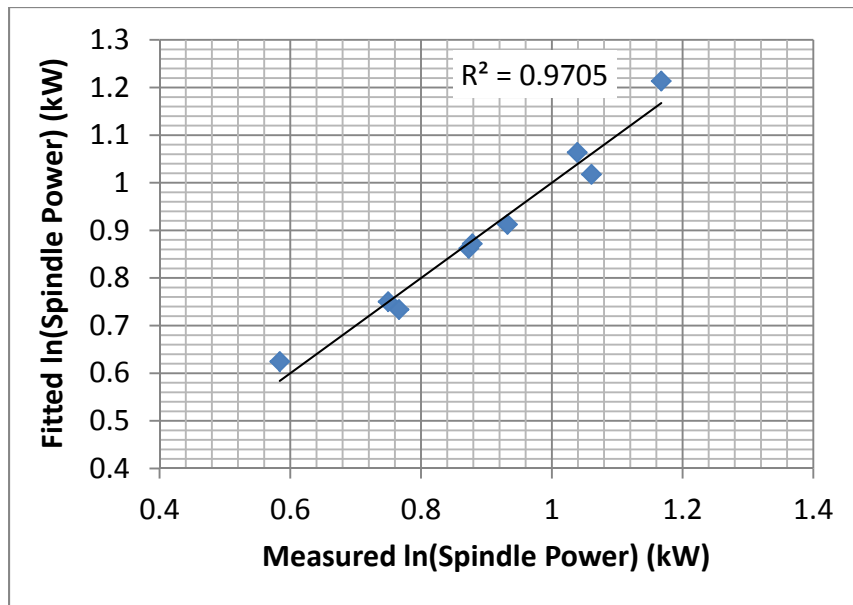
Figure 2-20 Fitted model against measured spindle power with travel and rotational speed as independent variables.

Figure 2-21 and Figure 2-22 show the relationship of spindle power with travel speed and rotational speed, respectively.   These figures show that spindle power increases with an increase in rotational or travel speed. The model fitted model in Equation (2-9) suggests that spindle power is more sensitive to changes in rotational speed, however, the data plotted in Figure 21

and Figure 22 do not show a great difference in sensitivity.   Figure 21 and Figure 22 show that a change in rotational speeds (i.e., between 300 RPM to 400 RPM) has the same effect on spindle power as a change in travel speed (i.e., between 2 IPM to 4 IPM).
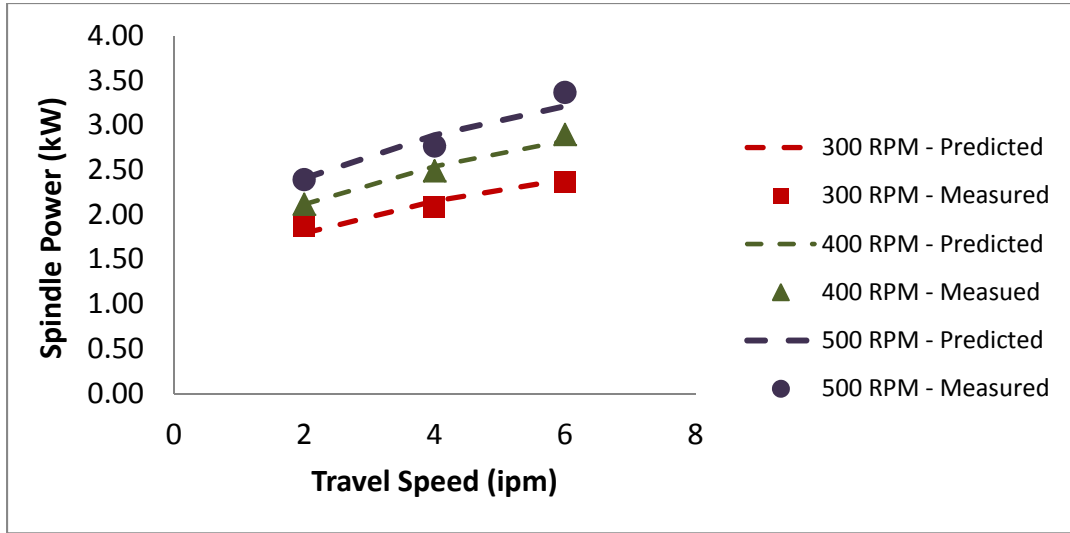
Figure 2-21 Spindle power as a function of travel speed.
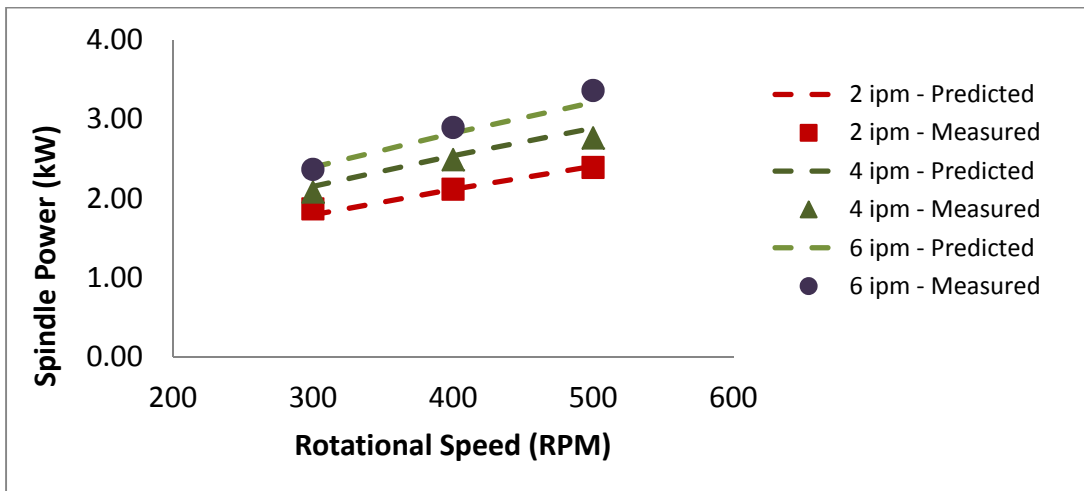
Figure 2-22 Spindle power as a function of rotational speed.

2.5.4.3 Specific Weld Energy

Specific weld energy can be expressed by Equation (2-10)

$$E_{specific} = 4.117\omega^{-0.426+1}v^{0.263-1} = 4.117\omega^{0.577}v^{-0.737} \qquad (2\text{-}10)$$

Equation (2-10) describes the relative measure of energy transferred per unit length of weld as a function of rotational and travel speed.   Summary of regression analysis of specific energy as a function of rotational and travel speed is shown in Appendix A-4. The coefficients are the same as those derived in Equation (2-9) and results show high R^2 value of 0.9931. Figure 2-23 shows the goodness of fit between the predicted and measured data for specific weld energy.
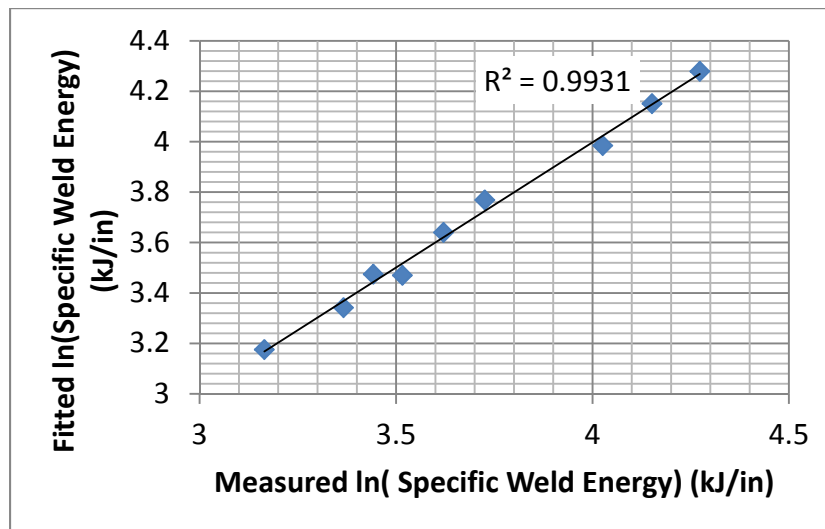
Figure 2-23 Fitted model for specific weld energy.

Figure 2-24 shows that the specific weld energy has a greater sensitivity to changes in travel speed as compared to changes in rotational speed as shown in Figure 2-25.   Figure 2-24 shows decreasing specific weld energy with increasing travel speed and highest weld energies

correspond to the highest rotational and lowest travel speed. At a given travel speed, specific

energy increases with increase in rotational speed. On the other hand, Figure 2-25 shows

increasing specific weld energy with increasing rotational speed. The lowest weld energies

correspond to the highest travel speeds.
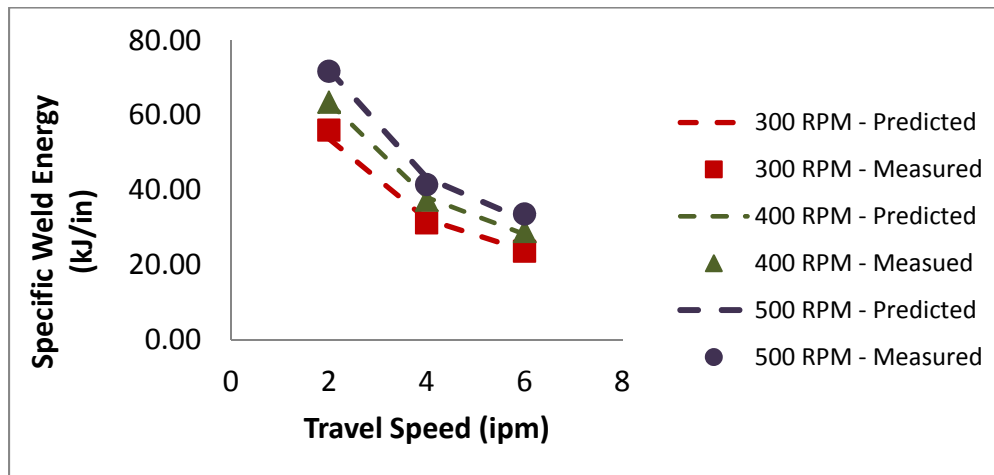
Figure 2-24 Specific weld energy as a function of travel speed.
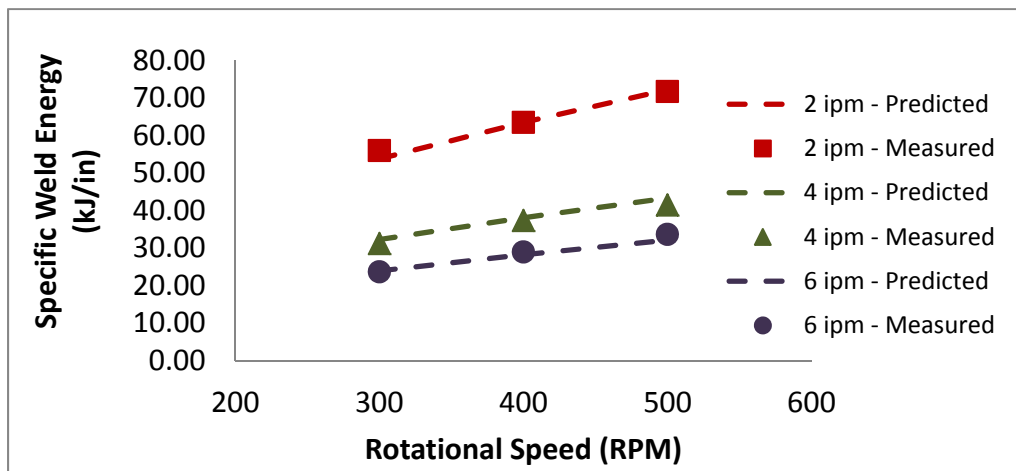
Figure 2-25 Specific weld energy as a function of rotational speed.

40

2.5.4.4 Cooling Rate

Appendix A-5 shows the summary output for the linear regression analysis for the relationship between cooling rate and travel and rotational speed. The regression analysis results show that rotational speed is not a statistically significant predictor of cooling rate in the presence of travel speed. A second regression analysis was performed using only travel speed as the independent value. The results are shown in Appendix A-6. The intercept and coefficient values for this second model are $A_{CR} = 9.139$ and $\beta_{CR} = 0.839$, therefore, $CR_{\Delta T(8\text{-}5)}$, can be expressed as in Equation (2-11) below:

$$CR_{\Delta T_{8-5}} = 9.319 v^{0.839}. \tag{2-11}$$

A plot showing fitted vs. average measured cooling rate values is shown in Figure 2-26.
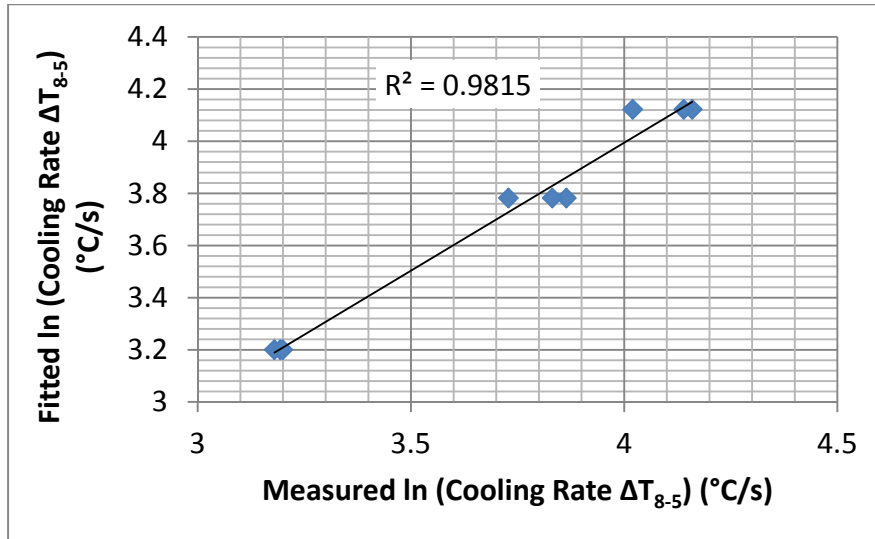
Figure 2-26 Fitted versus measured cooling rate.

The effect of travel speed and rotational speed on cooling rate can be seen in Figure 2-27 and Figure 2-28 respectively. Figure 2-27 shows an increase in cooling rate as travel speed

increases but very little to no change in cooling rate for changes in rotational speed at a given

travel speed. Figure 2-28 shows the sensitivity of cooling rate to changes in travel speed and

insensitivity to changes in rotational speed.
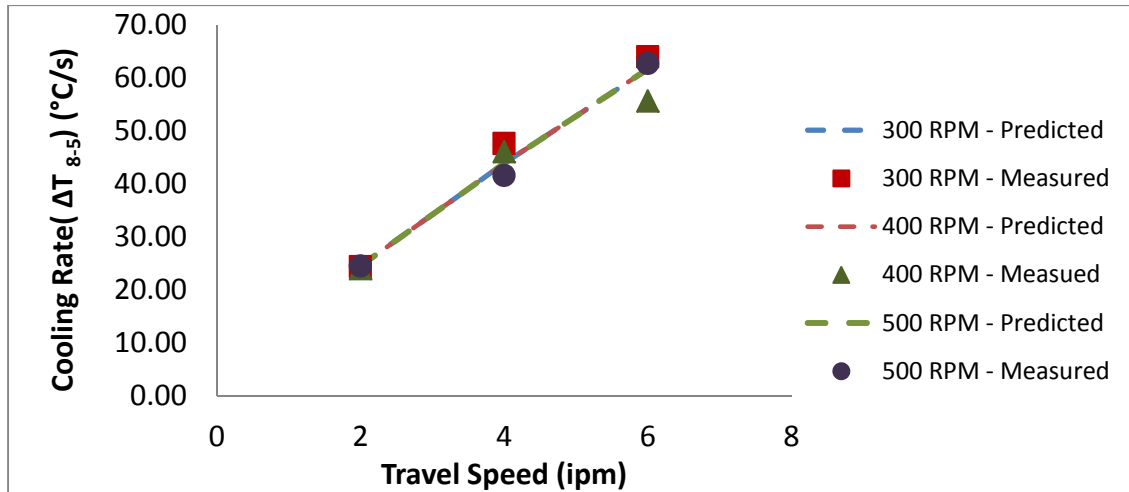
Figure 2-27 Cooling rate as a function of travel speed.
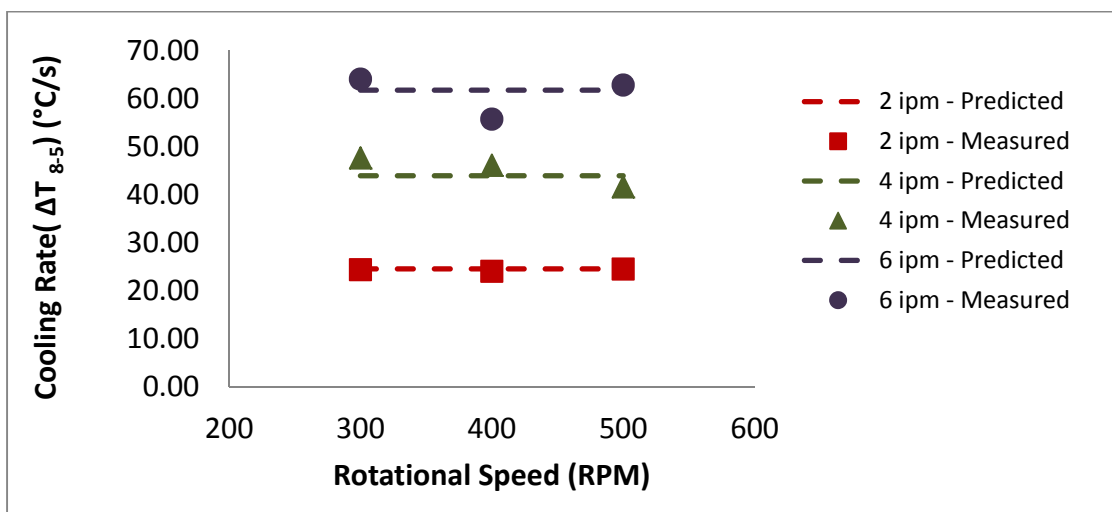
Figure 2-28 Cooling rate as a function of rotational speed.

2.5.4.5 Temperature

Appendix A-7 shows the summary output for regression analysis of peak HAZ temperature as a function of travel and rotational speed. These results show that rotational speed is not a statistically significant predictor of peak HAZ temperature in the presence of travel speed (see Appendix A-7). However, a second regression analysis using travel speed alone as an independent variable resulted in a lower adjusted R^2 value (0.7608 vs. 0.8014) (see Appendix A-8). Since the adjusted R^2 increases only if the new term improves the model more than would be expected by chance, the rotational speed term should be included in the model. The intercept and coefficient values for this model are A_{Tp}= 6.866, α_{Tp} = 0.086 and β_{Tp} = -0.1149, thus the model for peak HAZ temperature can be expressed as

$$T_p = 6.845\omega^{0.086}v^{-0.1149}. \tag{2-12}$$

A plot showing predicted versus measured peak HAZ temperature is shown in Figure 2-29. The R^2 value in this figure is 0.7609. .Figure 2-30 shows peak HAZ temperature as a function of travel speed. Figure 2-30 shows increasing HAZ peak temperature as travel decreasing. Little to no change in peak HAZ temperature is observed with changes in rotational speed, in particular at the lowest travel speed (see Figure 2-31). These trends validate the fitted model described in the previous paragraphs that show little correlation between rotational speed and peak HAZ temperature. The R^2 value of 0.7609 suggests other explanatory variables, not investigated here, account for changes in peak HAZ temperature. The observed trends for HAZ peak temperatures have not validated with peak nugget temperatures thus extrapolating the fitted model to describe the relationship between peak nugget temperatures and processing parameters should be not be done with caution. Rotational speed may have a more significant contribution on nugget peak temperature than in the HAZ in this low thermal conductivity material.
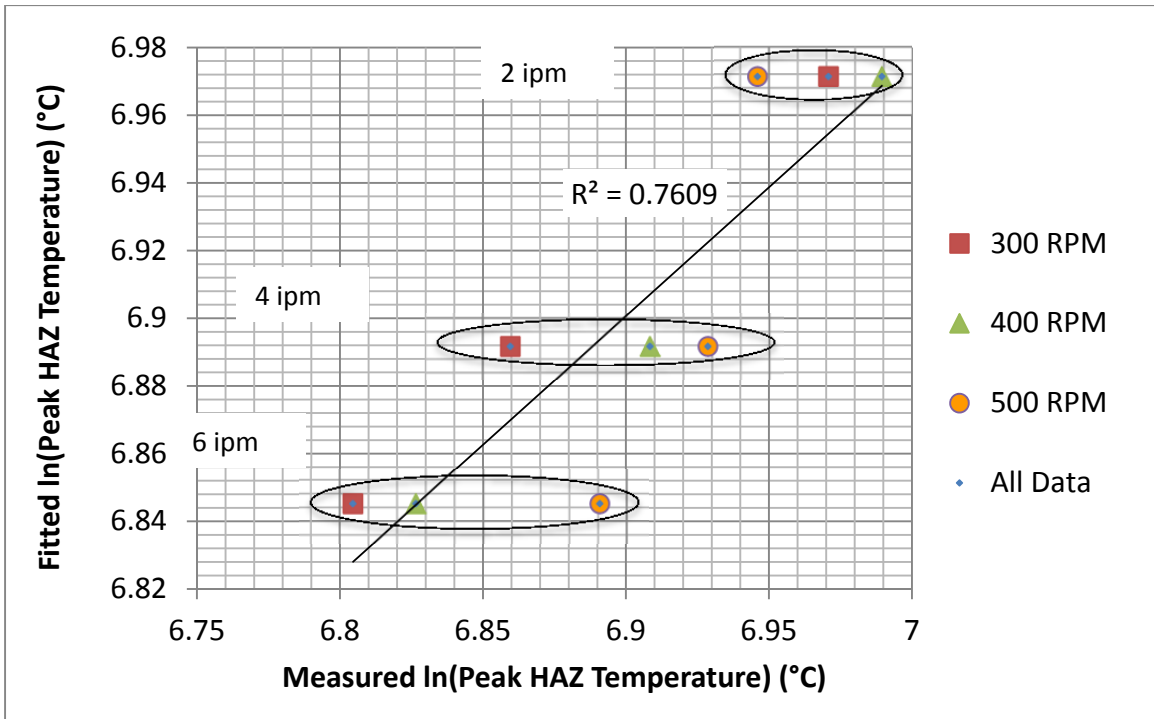
Figure 2-29 Predicted ln(peak temperature) to measured ln(peak temperature)
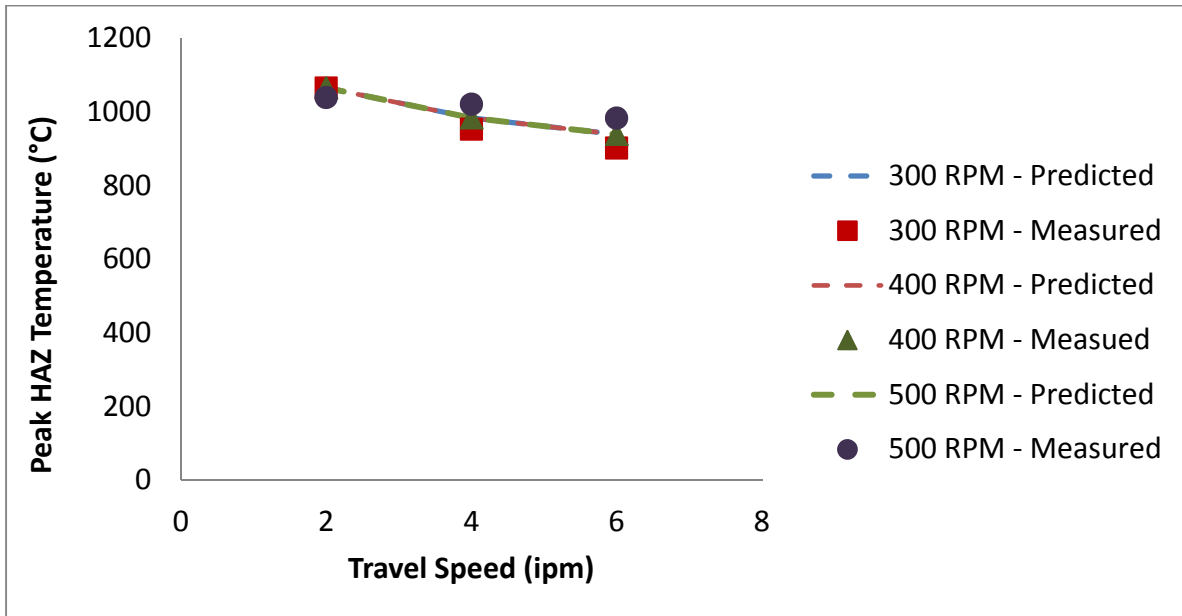
Figure 2-30 Peak temperature as a function of travel speed.
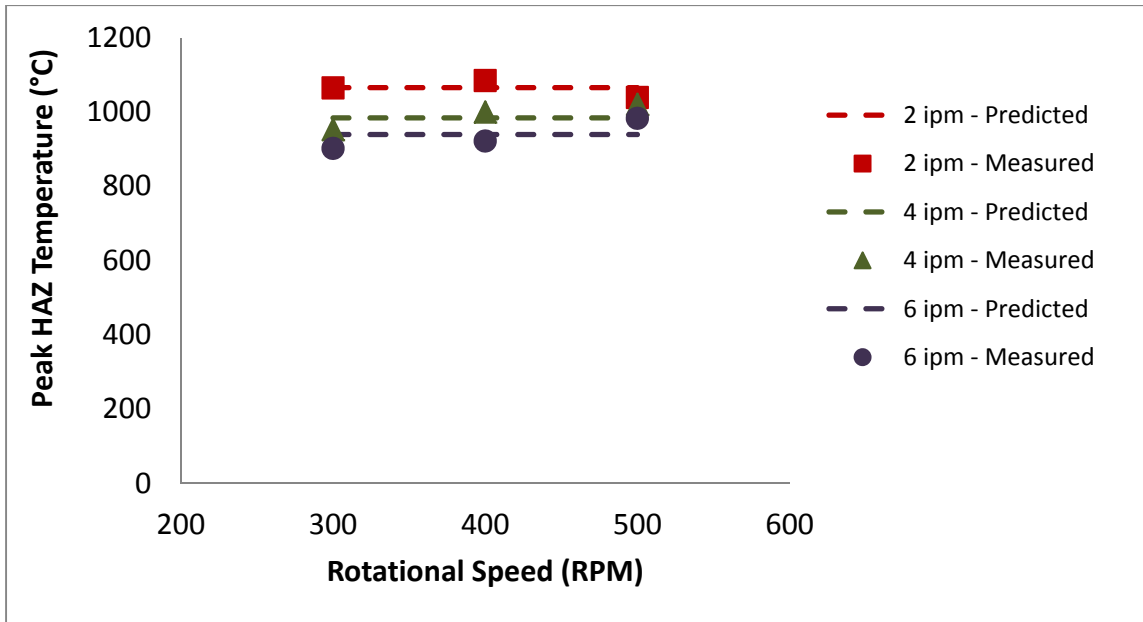
Figure 2-31 Peak temperature as a function of spindle speed.

2.5.4.6 Hardness

Appendix A-9 shows the summary output for this linear regression analysis for average stir zone hardness as a function of travel speed and rotational speed. Linear regression results indicate that travel speed in the presence of rotational speed is not a good predictor of the average stir zone hardness. A second regression analysis was performed using travel speed as the only independent variable. The output summary of that analysis is shown in Appendix A-10. Results from the second regression analysis indicate that a model with only travel speed is not a good predictor of average stir zone hardness. The p-value is just outside the 95% confidence level and the adjusted R^2 value is less than the adjusted R^2 value for the regression model that includes both travel speed and rotational speed. The adjusted R^2 value increases only if the new term improves the model. Therefore, the model including a non-significant variable of rotational speed is a better predictor of average stir zone hardness. The coefficients for this model are $A_H=$

45

5.364, α_H =-0.0874 and β_H = 0.0571. A plot showing predicted versus measured average stir zone hardness is shown in Figure 2-32. The plot shows poor correlation of the model in describing the relationship between process parameters and average stir zone hardness (R^2 value of 0.6229).

An additional regression analysis was performed using the 50 percentile hardness, 75 percentile hardness and IQR data determined from the CDF. The summary output results do not show good model correlation between 50 percentile and 75 percentile hardness to travel speed and rotational speed. The analysis did show that travel speed and rotational speed are strong indicators in the amount of spread (i.e., interquartile range (IQR)). The summary output results are included in Appendix A-11 and the predicted versus measured IQR of hardness data for this data set is shown in Figure 2-33.
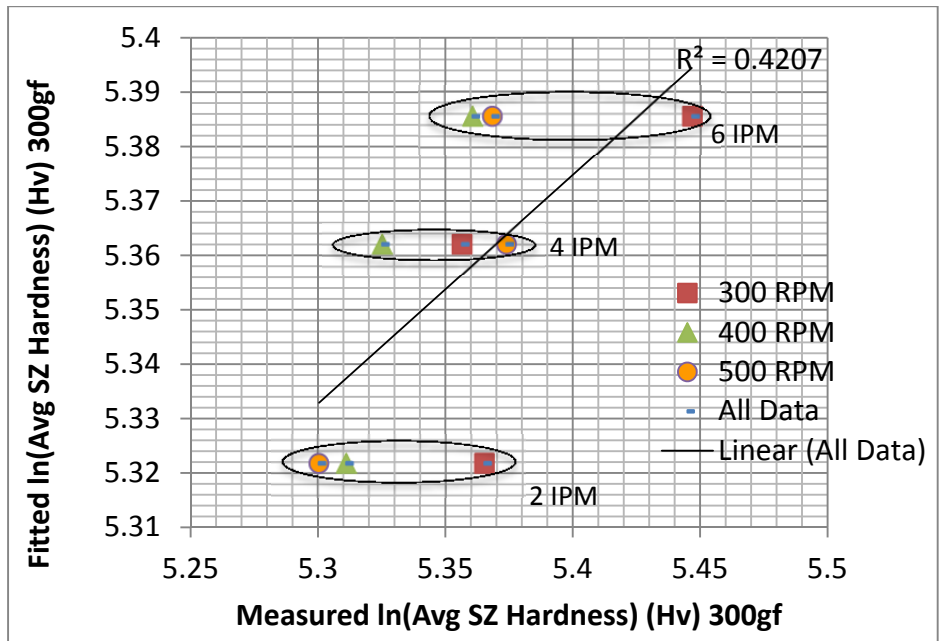
Figure 2-32 Fitted ln(average stir zone hardness) versus measured ln (average stir zone hardness).
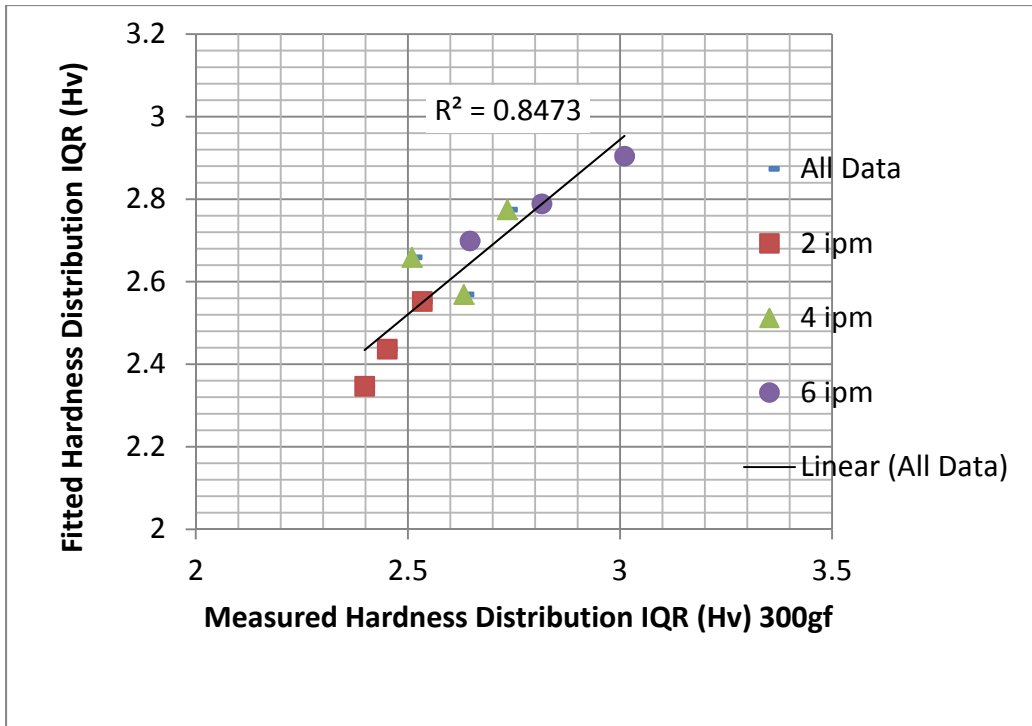
Figure 2-33 Fitted versus measured hardness distribution IQR.

2.5.4.7 Grain Size

Appendix A-12 shows regression analysis of grain size as a function of travel and rotational speed. These results show that neither rotational speed nor travel speed is a statistically significant predictor of grain size within a 95% confidence level. A second regression analysis with travel speed as the independent variable (see Appendix A-13) reveals that travel speed is a statistically significant predictor (R^2 = 0.6448), albeit not perfect. The adjusted R^2 value did not improve when the rotational speed term was included in the model further validating that rotational speed is not a good predictor of grain size. The relatively low value of R^2 is indicative that other unknown variables outside the scope of this program affect

grain size. The intercept and coefficient values for this model are A_{GS}= 1.658 and β_{GS} = -0.1394, thus the model for grain size can be expressed as

$$Grain\ size = 1.658v^{-0.1394} \qquad (2\text{-}13)$$

A plot of predicted versus measured grain size is shown in Figure 2-34.

Peak temperature, cooling rate, average stir zone hardness and grain size were each plotted against spindle torque, spindle power and specific weld energy in Figure 2-35 and Figure 2-36. Grain size and hardness were also plotted as a function of cooling rate in Figure 2-37 (a) and (b), respectively. A linear fit of all data show some correlation but can be improved upon.
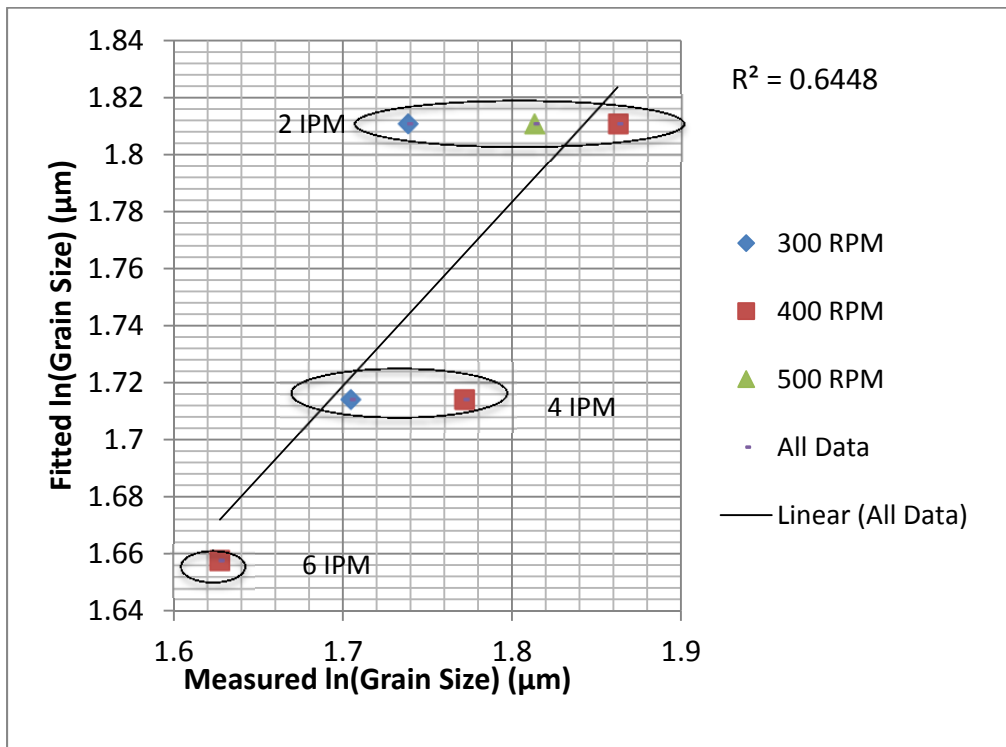
Figure 2-34 Fitted model versus measured ln(grain size) (μm).
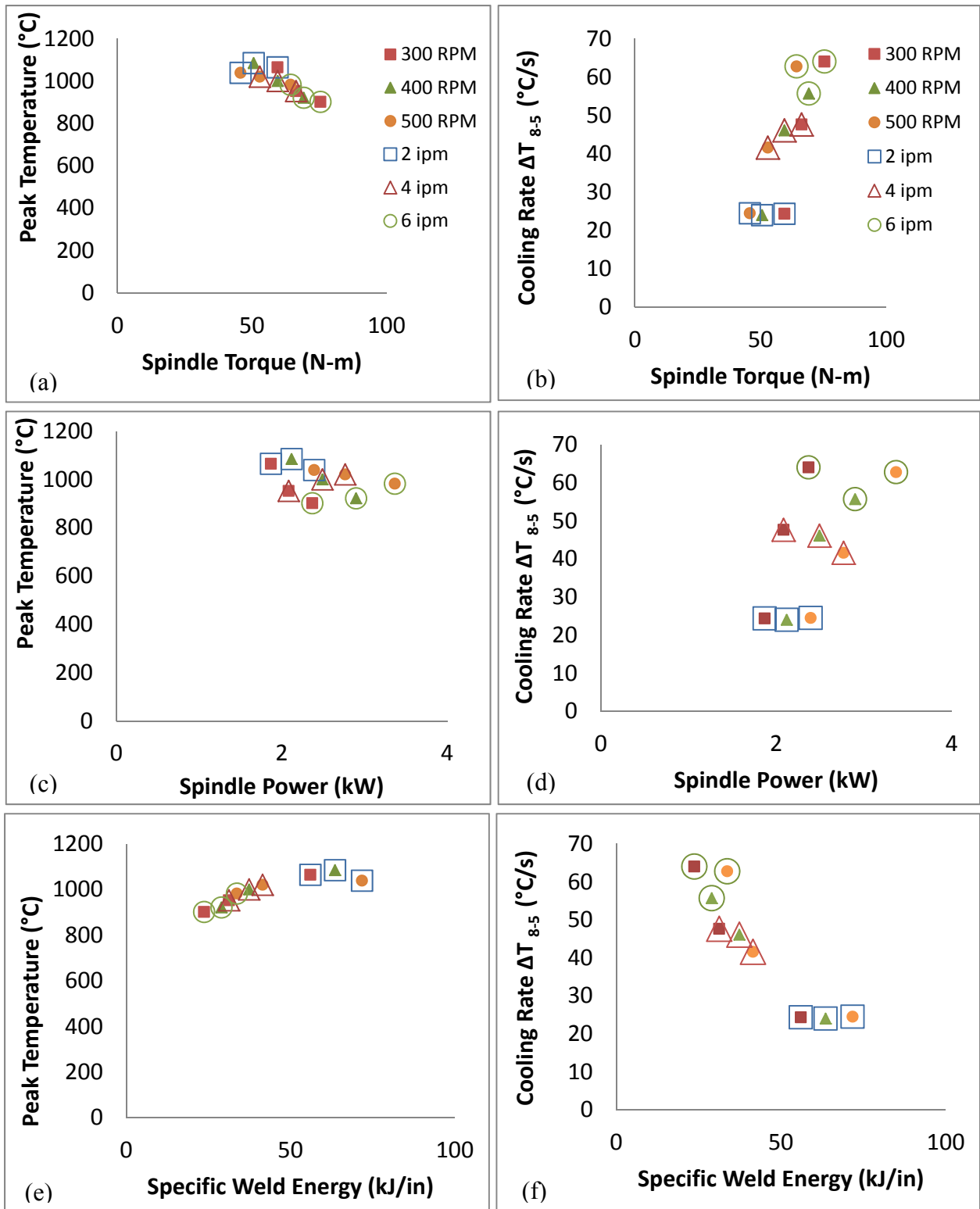
Figure 2-35 Plots showing peak temperature (left side) and cooling rate (right side) as a function of spindle torque, spindle power and specific weld energy. .The key code in plots (a) and (b) correspond to all the subplots.
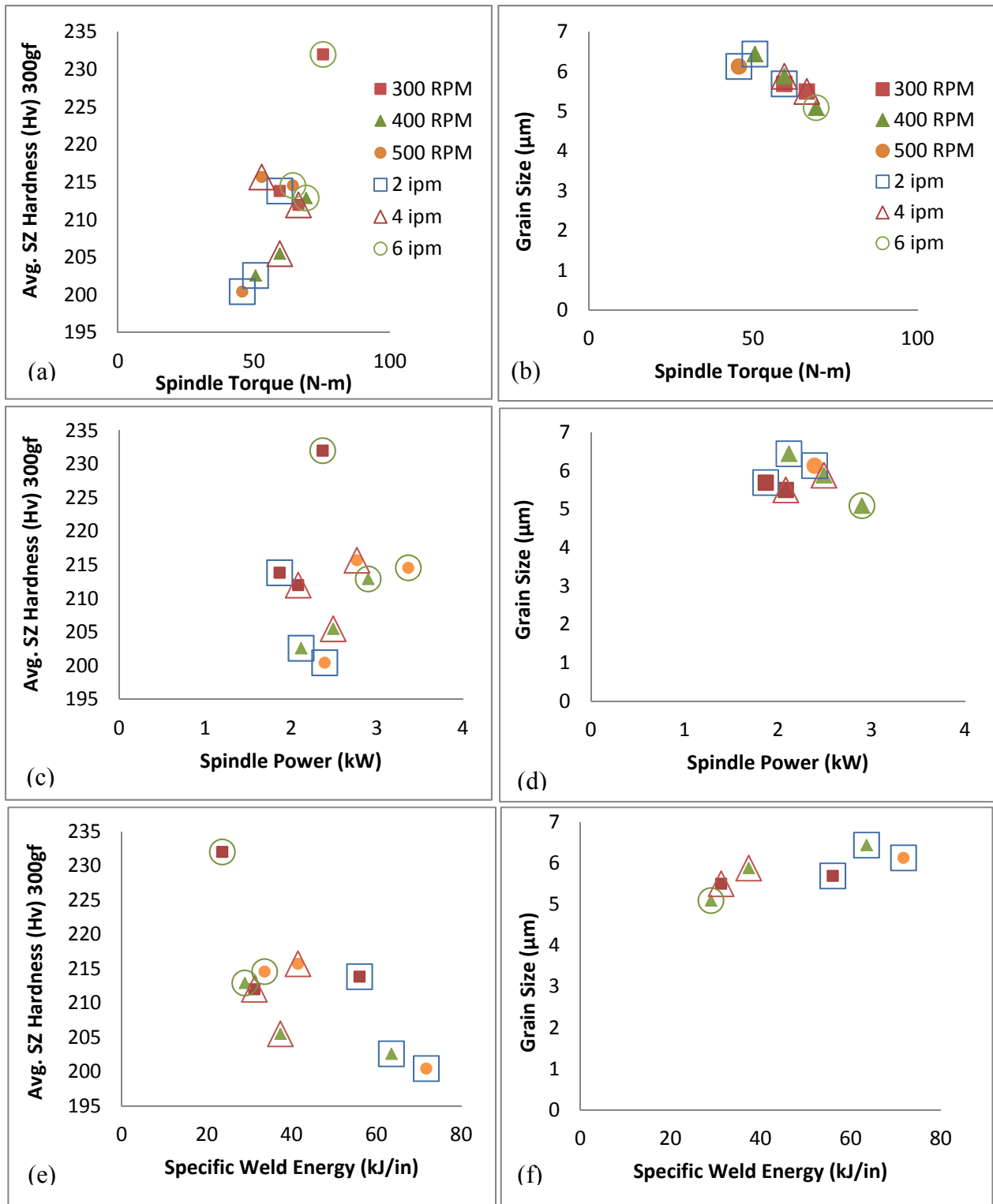
Figure 2-36 Plots showing average stir zone hardness (left side) and grain size ((right side) as a function of spindle torque, spindle power and specific weld energy. The key code in plots (a) and (b) correspond to all the subplots.
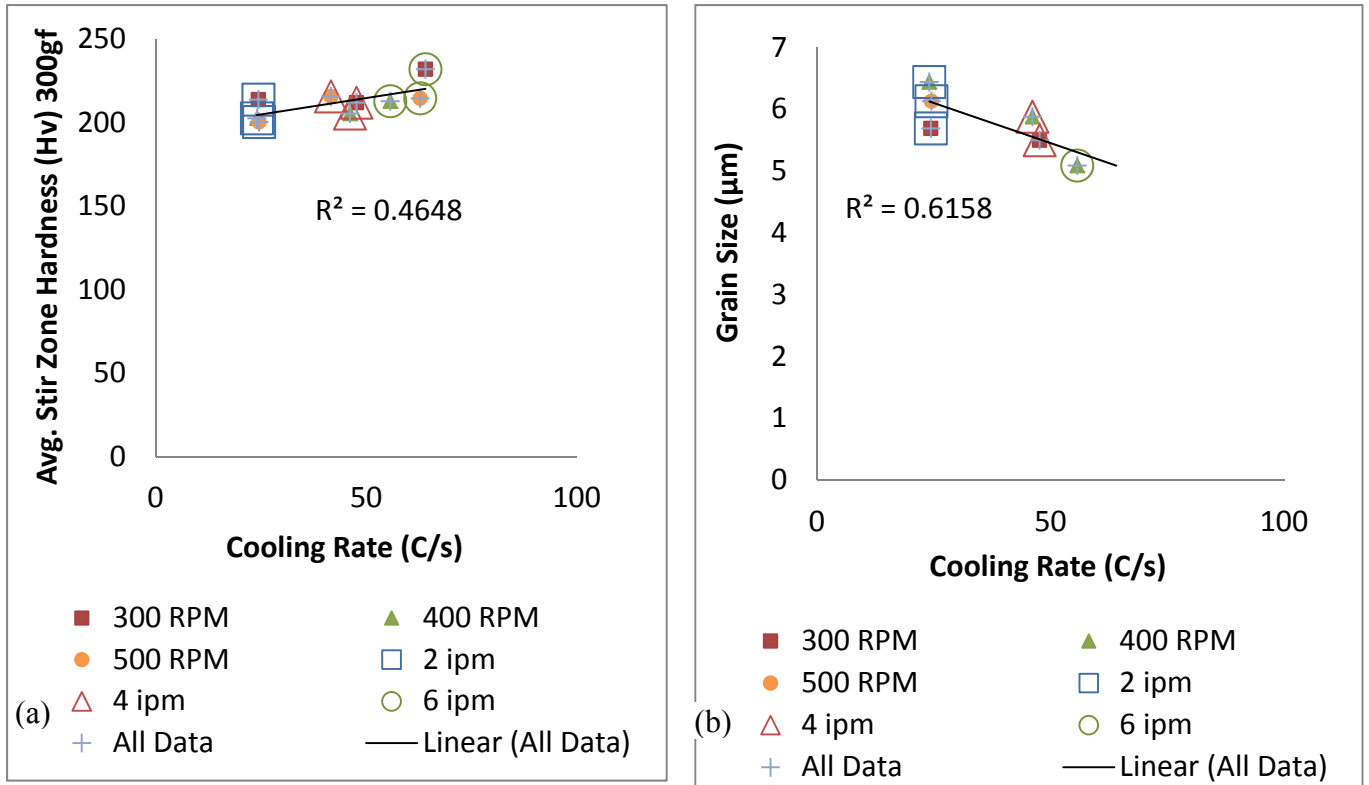
Figure 2-37 (a) Average all stir zone hardness and (b) grain size as a function of cooling rate (ºC/s)

Regression analyses were performed to describe these relationships as described in section 2.4.5.

The output results for peak temperature as a function of weld energy and spindle torque are shown in Appendix A-14 and A-15, respectively. The goodness-of-fit plots between the predicted and measured values for peak temperature as function of specific weld energy (shown in Figure 2-38) and as a function of spindle torque (shown in Figure 2-39) show strong correlations.
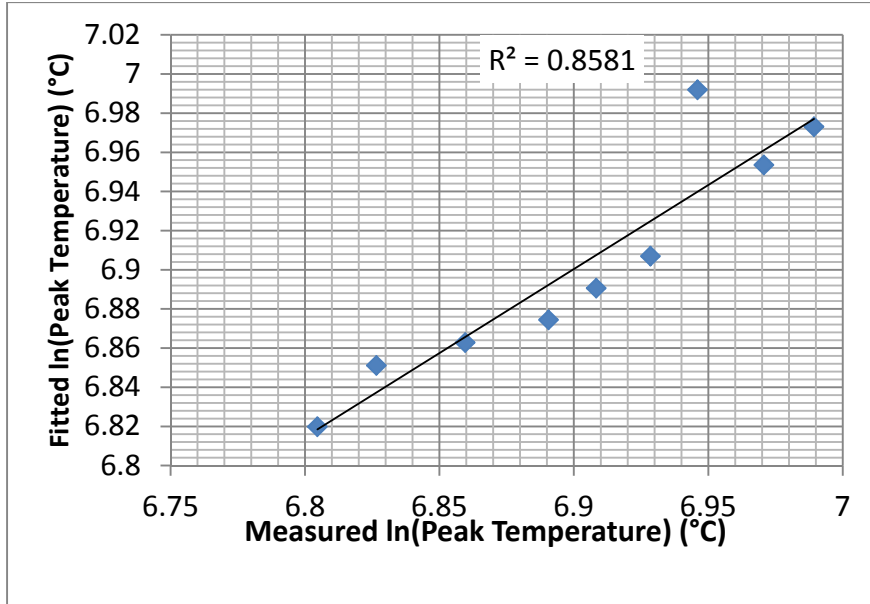
Figure 2-38 Fitted versus measured peak temperature with specific weld energy as an independent variable.
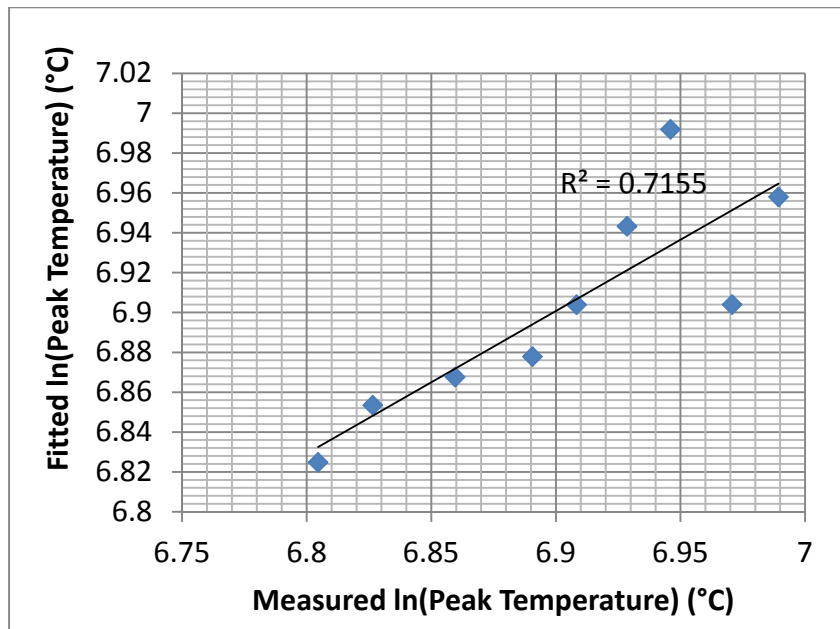
Figure 2-39 Fitted versus measured peak temperature with spindle torque as an independent variable.

Similar analyses were performed to determine if the relationships between cooling rate and specific weld energy and spindle torque. The output summary results are contained in Appendices A-16 and A-17, respectfully. The goodness-of-fit plots between the predicted and measured values for cooling rate as function of specific weld energy (shown in Figure 2-40) and as a function of spindle torque (shown in Figure 2-41) show strong correlations.

The output summary results for linear regression analysis between grain size and specific weld energy, spindle torque and cooling rate are contained in Appendices A-18, A-19 and A-20, respectfully. The goodness-of-fit plots between the fitted model and measured values for grain size as function of specific weld energy (shown in Figure 2-42), as a function of spindle torque (shown in Figure 2-43) and as a function of cooling rate (shown in Figure 2-43), The figures show some correlation but can be improved upon. The best predictor of the three evaluated is spindle torque.
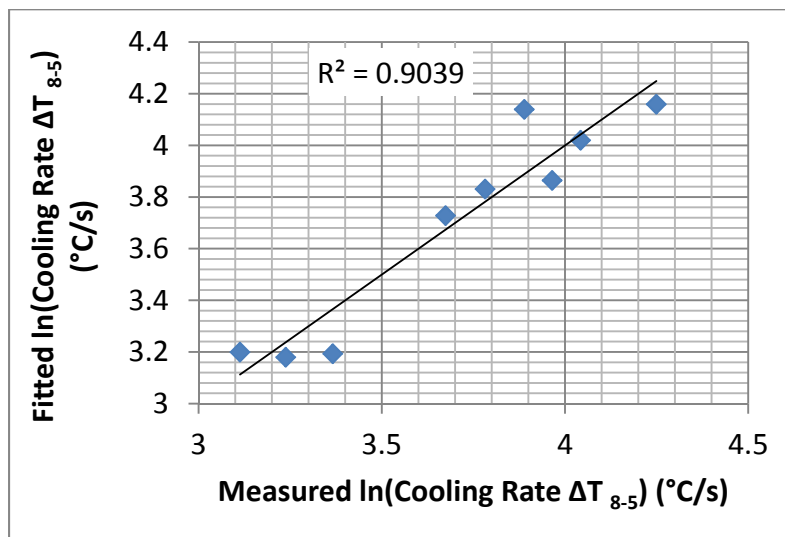
Figure 2-40 Fitted versus measured cooling rate with specific weld energy as independent variable.
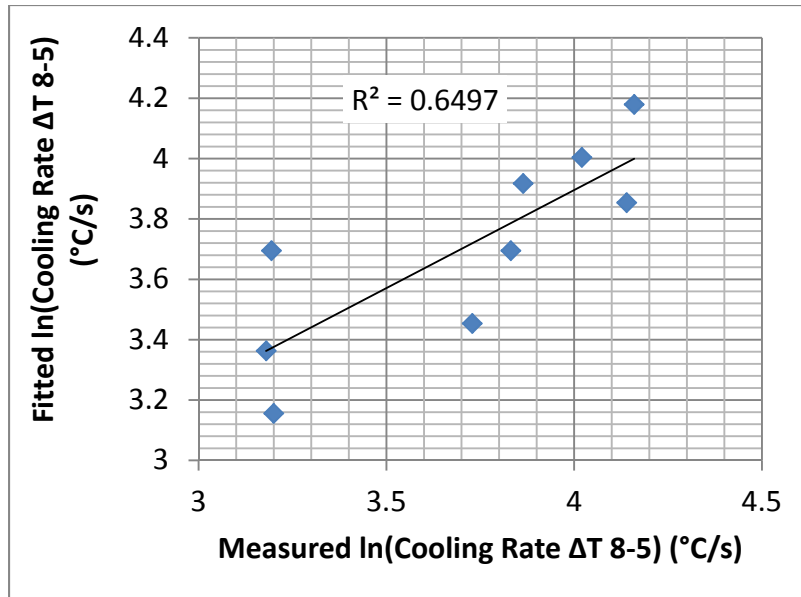
Figure 2-41 Fitted versus measured cooling rate with spindle torque as independent variable.
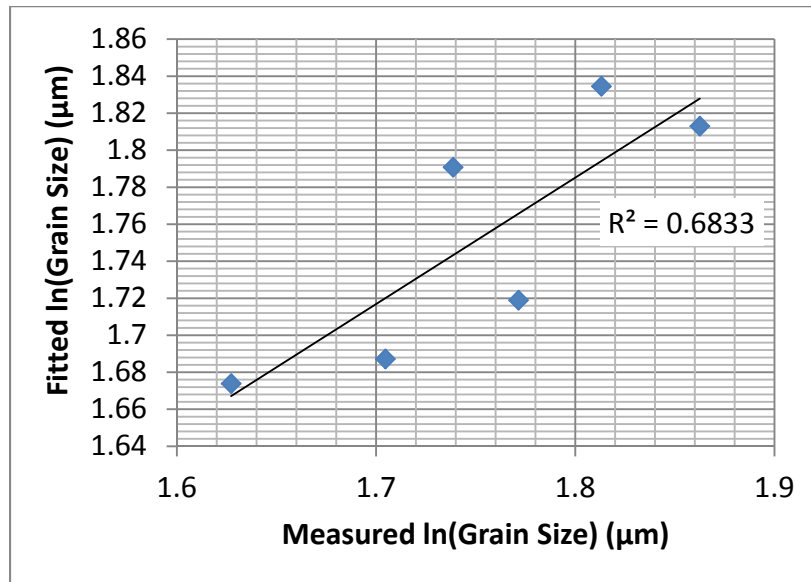
Figure 2-42 Fitted versus measured grain size with specific weld energy as independent variable.
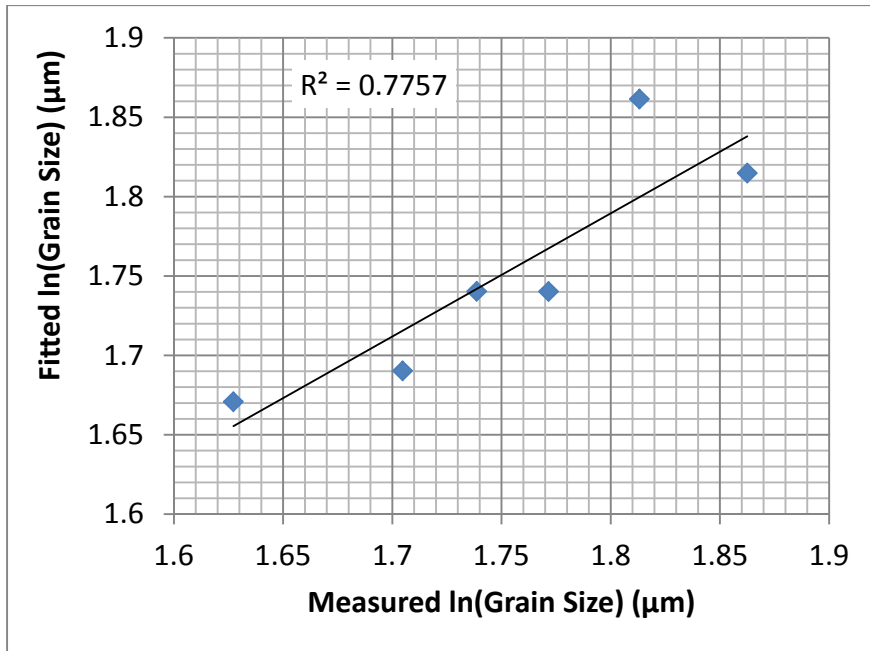
Figure 2-43 Fitted versus measured grain size with spindle torque as an independent variable.
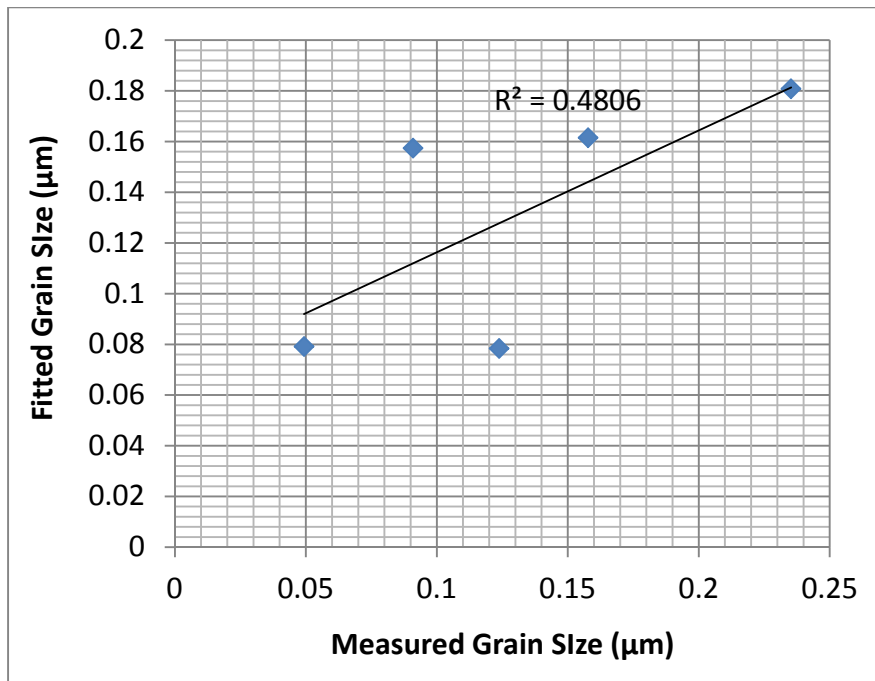
Figure 2-44 Fitted model for grain size using cooling rate as the predictor.

2.6   Discussion

Process output variables, peak temperature, cooling rate, hardness, grain size, spindle torque, spindle power, and specific weld energy were obtained from the set of experimental runs performed at varying travel and rotational speeds. All response variables were plotted as a function of travel speed and rotational speed. The following paragraphs explain how changes in travel speed and rotational speed affect the output response variables.

As travel speed increases, the tool moves forward a greater distance per revolution which increases the distance through which heat must travel and since the traversing speed in higher there is less time for heat to travel through the additional distance.   These combined effects lead to a reduced amount of heat generated and lower local peak temperatures. This reduction in heat generated can account for the decrease in specific weld energy and peak temperature, shown in Figure 2-35 (e). Cooling rate is inversely proportional to the product of temperature and heat input, thus at lower specific weld energy and peak temperature, higher cooling rates are expected as shown in Figure 2-35 (f). In addition, since the material surrounding the tool is "colder" with reduced localized heat generation then the material's flow stress increases. Higher forces are required to overcome the higher flow stresses. Since torque is defined as the measure of how much force must be exerted on an object to cause it to rotate, an increased force requirement translates to greater torque requirements. From Equation (2-4), we know that higher torque values at a given rotational speed translate to higher power requirements. Lower temperatures and higher spindle power are observed at higher travel speeds.

Heat generation and heat transfer per unit volume per unit time can account for trends observed for changes affecting spindle torque. Heat is generated as the tool rotates within the workpiece. As the rotational speed increases, all other factors remaining constant, the amount of

heat generated increases. This additional heat generated can be equated to an increase in energy input per unit length, i.e., specific weld energy, which can contribute to a thermal softening effect.   In the presence of thermal softening, the material's flow stress decreases, thus reducing the force required to move material around the periphery of the tool. Figure 2-35 (e) and (f) and Figure 2-36 (e) and (f) show higher values of specific weld energy with increases in rotational speed for a given travel speed.   As previously stated, torque is a measure of force required to rotate an object, thus a reduced force requirement translates to reduced torque requirements. Figure 2-35 (a) and (b) and Figure 2-36 (a) and (b) show that the lower torque values are observed at the highest rotational speeds.

In order to address the lack of correlation between hardness and process parameters and one must consider the effect of work hardening and dynamic recovery during deformation. During deformation, strengthening of a metal occurs by the production of dislocations which can be quantified by the increase in dislocation density during deformation. This means that strengthening in metals occurs through dislocation's resistance to slip. Strengthening equates to hardness and is proportional to the square root of dislocation density.

During plastic deformation, most of the plastic work is converted to heat, also known as adiabatic heating. For low thermal diffusivity material, such as 304L SS, heat builds up causing localized heating and a thermal softening effect on the material. Lee et al. indicated that if this thermal softening effect surpasses that of the work hardening effect then instabilities in metal flow may occur [23]. The micrographs show inconsistent flow patterns at all processing parameters and the hardness correlation to processing parameters is not consistent. The next chapter evaluates the effect peak temperature and strain rate on microstructure and hardness. The results of that evaluation will help in our understanding.

57

2.7   Conclusions

This study characterized microstructural and hardness distribution of friction stir processed 304L SS. The measured output responses for the series of processed cross-sections were used in regression analysis to investigate relationships between the independent process variables, namely travel speed and rotational speed, to the dependent output process variables. Table 2-4 and Table 2-5 lists the values for coefficients determined from linear regression analysis.

Table 2-4 Summary of Regression Coefficients and Statistics R^2 and Adjusted R^2 Values When Using Rotational Speed and Travel Speed as Predictors

	A	α	β	R^2	Adj R^2
Spindle Torque (Nm)	4.118	-0.423	0.263	0.9619	0.9491
Spindle Power (kW)	4.118	0.577	0.263	0.9705	0.9606
Specific Weld Energy (kJ/in)	4.118	0.577	-0.737	0.9931	0.9908
Cooling Rate (ºC/s)	4.097	-0.131	0.839	0.9846	0.9908
Cooling Rate (ºC/s)	9.139	--	0.839	0.9815	0.9788
Peak Temp (ºC)	6.87	0.086	-0.115	0.8511	0.8014
Peak Temp (ºC)	6.845	--	-0.115	0.7608	0.7267
All Stir Zone Hardness (Hv)	5.364	-0.087	0.058	0.6229	0.4972
All Stir Zone Hardness (Hv)	5.386	--	0.058	0.4207	0.3379
IQR Hardness (Hv)	2.699	-0.4022	0.321	0.8473	0.7965
Grain Size (µm)	1.697	0.1247	-0.134	0.7319	0.5533
Grain Size (µm)	1.657	--	-0.1397	0.6448	0.5560

Note:
A is the intercept, α is the coefficient for rotational speed, and β is the coefficient for travel speed.

Table 2-5 Summary of Regression Coefficients and Statistics R^2 and Adjusted R^2 Values When Using Specific Weld Energy, Spindle Torque, and Cooling Rate as Predictors

	A	γ	δ	ζ	R^2	Adj R^2
Peak Temp (ºC)	6.99	0.155			0.8581	0.8378
Peak Temp (ºC)	6.824		0.345		0.7155	0.6749
Cooling Rate (ºC/s)	3.112	-1.024			0.9038	0.8901
Cooling Rate (ºC/s)	4.178		2.04		0.6497	0.5997
Grain Size (µm)	1.835	0.1773			0.6833	0.6041
Grain Size (µm)	1.67		-0.4594		0.7757	0.7196
Grain Size (µm)	-0.198			-0.1239	0.4806	0.3075

The following conclusions can be drawn from this chapter:

(1) Spindle torque is more strongly influenced by rotational speed than travel speed although to a lesser extent in 304L SS than in aluminum alloys. Results for 304L SS are in general agreement with literature in that spindle torque decreases with increasing rotational speed and increases with increasing travel speeds with other things being equal.

(2) Spindle power is a function of both travel and rotational speeds and increases with an increase in either parameter, in agreement with models developed for aluminum alloys.

(3) Specific weld energy has a greater sensitivity to changes in travel speed than to changes in rotational speed. Specific weld energy decreases with an increase in travel speed and specific weld energy is minimally affected by changes in rotational speed, although for 304L SS, specific weld energy slightly decreased as rotational speed decreased for a

given travel speed and the effect was slightly greater at the lowest travel speed used in this study.

(4) Cooling rates in 304L SS is affected by changes in travel speed. Changes in rotational speed had little to no effect on changes in cooling rate. Higher cooling rates were noted at higher travel speeds.

(5) The peak HAZ temperature decreases as travel speed increases. Little to no change is observed with changes in rotational speeds. The insensitivity of temperature to changes in rotational speed is surprising since a large number of authors report increased in temperature with increasing rotational speed. However, it is reasonable to speculate that at distances away from the stir zone region, particularly for low thermal diffusivity materials, the effects of changing processing parameters may not be as significant.

(6) A good model to quantify observed hardness to processing parameters is difficult to obtain from this data set. The independent variable with the highest correlation factor to hardness is IQR of hardness data distribution. Additional studies are needed to evaluate the isolated effect of strain rate and temperature on hardness in this alloy to gain a better understanding of its effects.

(7) For this data set, grain size was modeled as a function of rotational speed with a low R^2 value indicating low confidence for that model. The proposed model shows that grain size is inversely proportional to travel speed in accord with models developed for aluminum alloys.

3 CHARACTERIZATION OF 304L SS COMPRESSION TESTS PERFORMED UNDER KNOWN THERMOMECHANICAL HISTORIES

3.1 Abstract

Developments in modeling (both physical and numerical) are being used to develop a greater understanding of the influence of various metallurgical factors (e.g., grain size, dislocation density, and texture) on the properties (e.g., hardness) of friction stir welded materials. The overall scope of this work is geared towards evaluating Isaiah, an existing 3-dimensional FSW finite element code developed at Cornell University, through metallographic evaluation and hardness measurements from a series of actual friction stir welds and physically-simulated conditions. Hot axial compression tests were performed on the Gleeble 1500™. The 6.25 mm diameter 304L stainless steel cylindrical specimens underwent a similar heating and cooling thermal profile as that measured from an actual FSW in the same material. Metallography, hardness, texture and flow stress from hot compression tests were characterized as a function of strain rate (1 s^{-1}, 10 s^{-1}, 50 s^{-1}, and 100 s^{-1}) and peak temperature (900°C, 1000°C, and 1100°C). This paper presents flow stress, metallography and hardness for specimens isothermally compressed at 10 s^{-1}, 50 s^{-1}, and 100 s^{-1} each at 900°C, 1000°C, and 1100°C. Regression models were generated that describe how peak stress and grain size vary as a function of temperature and strain rate as well as how grain size varies as a function of peak stress. No statistically-significant correlations of hardness to temperature and strain rate were found.

3.2 Introduction

Friction stir welding is a thermal and thermomechanical process that involves extreme plastic deformation resulting from the solid-state stirring of one base metal into another. The extreme plastic deformation within the weld nugget generally occurs at high temperatures (~1100ºC for steels) and at high strain rates. These high temperatures and high strain rates are analogous to other hot deformation processes that have been modeled extensively. In friction stir welding, however, the temperature and strain rates are not homogeneous as with other hot

deformation processes, such as rolling. Friction stir welds exhibit severe thermal and deformation gradients that result in microstructural and hence mechanical property variations across these localized weld regions.

In hot deformation processes, work hardening, dynamic recovery, and dynamic recrystallization occur simultaneously [24]. These flow characteristics are evident in flow stress curves that can be generated experimentally using a thermomechanical simulator, such as the Gleeble system used in this study. This type of information is extremely useful in understanding how a material in solid-state form behaves in the presence of deformation and temperature. Developments in material science and modeling have been very helpful in explaining solid-state flow as a function of numerous deformation variables during hot-working processes.

3.3   Previous Work

As with hot deformation processes, friction stir welding is a complex process. In hot deformation processes, work hardening, dynamic recovery, and dynamic recrystallization occur simultaneously [24]. These are the mechanisms by which a material tends to soften in hot-working. In metals with low stacking fault energy, such 304L austenitic stainless steel, dynamic recovery and dynamic recrystallization (DRV) are softening mechanisms. DRV occurs by the formation of well-developed sub-grain structures by polygonization of dislocations through cross slip and climb that is similar to the mechanism that occurs in creep deformation. When the critical driving force from large local differences in dislocation density is reached then new grains nucleate along the grain boundaries that lead to dynamically recrystallized (DRX) grains

[25]. DRX is a softening mechanism that occurs when the dislocation density reaches a critical value to rearrange or nucleate new high angle grain boundaries.

As such, researchers have used controlled thermomechanical tests to gain a better understanding DRV and DRX in 304 and other stainless steels. The following paragraphs describe such efforts [26-30].

In work performed by Medina and Hernandez [26-29] torsional tests in a thermomechanical simulator were performed to model various aspects of hot metal working deformation for micro-alloyed steels. Using empirical and constitutive relationships such as the Zener-Hollomon, Sellars and Tegart, Von Mises and Avrami's equations, the authors were successful in predicting stress-strain curves, peak stress, peak strain, flow stress curves, static recrystallization, and dynamic recrystallization as a function of temperature and strain rate for various chemical compositions of micro-alloyed steels.

Other authors used stress-strain curves generated through continuous hot torsion tests to understand work hardenability, static recrystallization and restoration, and dynamic softening in 304 SS. Barraclough and Sellars [28] performed hot torsion tests on type 304 SS. The authors confirmed that static recrystallization curves conform to Avrami's equations, but a smaller exponent should be used for coarser grain materials due to a greater amount of non-uniform deformation in these materials. The authors discuss and conclude several good points. First, specimen geometry is important on the effect on the heterogeneity of deformation. They state that long and thin specimens provide good heterogeneity in tension, while small length/diameter ratio specimens would render less heterogeneity in axisymmetric compression testing, and small height/cross-sectional area ratio specimens give good results under plane strain compression testing, as confirmed in [30]. Second, the authors state that the major restoration of hardness on

annealing after hot deformation is associated with static recrystallization. Finally, the authors point out that recrystallization time and recrystallized grain size decrease as (1) the initial grain size decreases, (2) strain increases, (3) strain rate increases, and (4) deformation temperature decreases.

Ryan et al. [25, 31, 32], evaluated the work hardening, strengthening and ductility in hot working of 304 stainless steel using hot-torsional tests. The authors experimentally validated the hyberbolic sine function of Sellars and Tagert equation and the Arrhenius equation with 304 experimental data at temperatures 900 – 1200°C and strain rates of 0.1 to 5 s^{-1}.

Arbegast [33] used output from thermomechanical tests to develop flow stress curves as a function of temperature and strain rate for various aluminum alloys to develop constitutive relationships for use in a first order approximation of the friction stir welding process using the architecture of hot metal working models. Using this developed FSW process model, Arbegast calculated the extrusion pressure (i.e., the force opposite the direction of travel that is exerted on the pin during friction stir welding). By comparing the extrusion pressures for each of the Al alloys investigated, the author was able to verify experimental trends observed and gain insight into the optimum processing conditions (pin tool geometry, extrusion zone width, processing parameters, and flow stress of the material) for joining various types of aluminum alloys.

3.4 Experimental Details

3.4.1 Materials

The cylindrical test specimens used in this study were machined from nominal 0.25 in (6.4 mm) thick 304L SS with a chemical composition listed in Table 3-1. The corresponding

specification requirement and friction stir weld chemistry are also listed for reference. The

longitudinal axis of the 0.25 in (6.4 mm) diameter specimens was aligned parallel to the plate

rolling direction and had a diameter-to-length ratio ranging from 1.0 to 1.3.

**Table 3-1 Bulk Chemical Analysis of 304L Stainless Steel
Base Metal and Weld Metal**

Element	ASTM A 240/A 240M	FS Weld Metal	Base Metal
	wt%	wt%	wt%
Carbon	0.030 max	0.014	0.019
Manganese	2.00 max	1.72	1.70
Silicon	0.75 max	0.27	0.28
Sulfur	0.030 max	0.001	0.001
Phosphorus	0.045 max	0.025	0.016
Nickel	8.0-12.0	8.58	8.16
Molybdenum	--	0.43	0.44
Chromium	18.0-20.0	18.13	18.76
Cobalt	--	0.29	0.29
Nitrogen	0.10 max	0.088	0.087
Boron	--	0.0015	0.0048

3.4.2   Thermal and Thermomechanical Simulations

The Gleeble 1500 system was programmed to perform a series of thermal and thermo-

mechanical simulations that systematically varied peak temperature and strain rate. The

simulation test matrix is detailed in Table 3-2. The peak temperatures were selected based on

thermocouple data and on hot deformation studies of 304 and 304L stainless steel performed by

others [22, 25, 31, 32, 34, 35]. All cylindrical test specimens underwent a similar heating and

cooling thermal profile as that measured from an actual FSW in the same material. The details

of the actual FSW temperature measurements are reported elsewhere [22]. A thermocouple was

attached along the longitudinal mid-span of the specimen to measure the actual specimen temperature during the simulation test.

Table 3-2 Gleeble Thermal and Thermomechanical Simulation Test Matrix

Peak Temperature (°C)	Strain Rate	Time to Full Compression (s)	Heating Rate (°C /s)	Cooling Rate (°C /s)
900	0	--	RT to 85 °C = 10 85 to 260 °C= 175 260 to Tp °C = 60	Tp to 500 °C = 23 500 to 340 °C = 9 340 to 220 °C = 4 220 to RT °C = 1
	*1	4.0000		
	10	0.0842		
	*50	0.0798		
	100	0.0397		
1000	0	--		
	1	4.0000		
	*10	0.4020		
	*50	0.0794		
	*100	0.0402		
1100	0	--		
	1	4.0600		
	10	0.4040		
	50	0.0800		
	100	0.0402		

*shape coefficients did not meet the specified requirements for valid compression test conditions.

The longitudinal axis of the cylindrical specimens was positioned parallel to the compression axis and centered between two ISO-T anvils (shown in Figure 3-1 (c)). The ISO-T anvils were designed to ensure uniform heating and deformation during thermo-mechanical testing. A boron nitride coating, a dry, high temperature lubricant, was lightly sprayed on the face of each anvil to minimize the amount of barreling during compression. A jaw-to-jaw L-strain gauge system was positioned across the jaws to provide precise dynamic displacement

measurements. The measured displacement measurements were used in calculating true stress, true strain plots. The experimental set-up within the Gleeble test chamber is pictured in Figure 3-1. Once the test specimen was secured between the anvil/jaw assembly and thermocouple wires were connected, the test chamber was vacuum-sealed and flooded with argon gas.
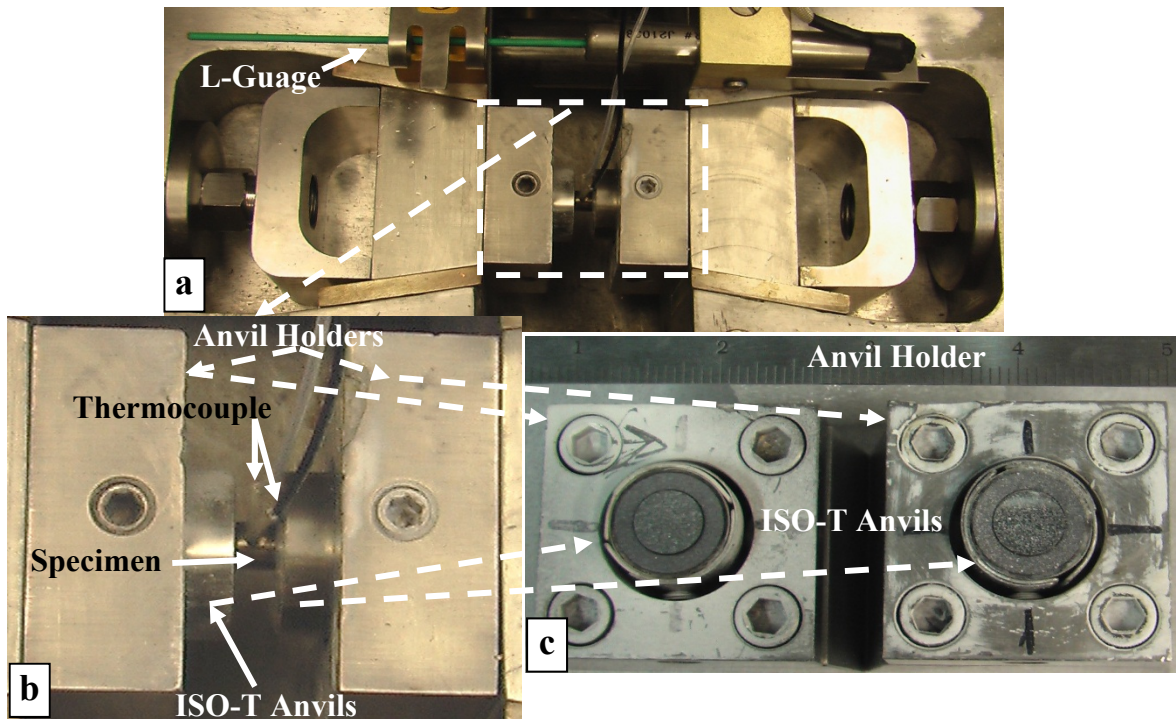
Figure 3-1 Experimental set-up within Gleeble chamber showing (a) set-up within the testing chamber of the Gleeble (b) close-up view of specimen with thermocouple sandwiched between anvils and (c) anvil holder with ISO-T anvils in place. Note the light boron nitride coating on the anvils was used as a lubricant.

As indicated in Table 3-2, one specimen at each peak temperature underwent the heating and cooling cycle. These specimens will be referred to as "thermal-only" for the remainder of the paper. These specimens were heated to peak temperature at the specified heating rate, held

for 1 second then cooled to room temperature at the specified cooling rate. The hot, uniaxial compression test specimens were each heated to peak temperature, held for 1 second, compressed at the specified strain rate to a 3 mm final length, held for 1 second then cooled to room temperature. The test specimens were measured before and after compression testing to calculate shape coefficients (barreling, ovality, and height). Specimens after testing are shown in Appendix B-1. These shape coefficients, listed in were used to determine the validity of the compression test data.

3.4.3 Metallography, Electron Backscatter Diffraction and Orientation Image Microscopy (EBSD-OIM)

All specimens, including untested base metal specimens, were sectioned at the center along the plane parallel to the compression axis (or rolling direction for base metal), mounted and metallographically prepared to a 1 μm finish. Vickers (Hv) microhardness measurements were taken at incremental spacing of 0.30 mm along intersecting diagonal paths using a 300 gf load. The metallographically-prepared specimens were etched with Luca's reagent (150 mL HCl, 50 mL lactic acid, 3 g oxalic acid) to reveal grain size and other microconstituents.

To prepare for orientation image microscopy (OIM) in a scanning electron microscope (SEM), the mounted specimens were then re-ground and polished in a colloidal silica suspension. A 200 x 200 μm area was scanned at the center of each specimen in the SEM using EBSD at a 20 keV accelerating voltage and a step-size of 0.5 μm. Grain size plots, misorientation plots, image quality images, orientation map images, phase map images, pole figures, inverse polar figures, and texture plots were captured using OIM software. Only grain size, image quality and phase map images are presented in this paper.

68

3.4.4   Hardness

Vicker's (Hv) microhardness measurements were taken at incremental spacings of 0.30 mm along intersecting diagonal paths using a 300 gf load.

3.5   Results and Discussion

3.5.1   Thermal and Thermomechanical Simulations

3.5.1.1 Thermal-Only

The measured temperature profile at 900°C is plotted in Figure 3-2 against the programmed temperature profile. The measured temperature profile is within 0.1234±0.911°C/s of the programmed temperature profile for the majority of the test, from 1.2 s to 196 s. Thereafter, for the remaining 60 seconds, the measured temperature profile deviates 25.9±16.5°C/s from the programmed path upon cooling from 88°C. For the critical portions of the temperature profile, the Gleeble system was capable of simulating thermal profiles that are representative of actual friction stir welding conditions. Similar profiles were observed for compression tests conducted at 1000°C and 1100°C deformation temperatures.

Uniaxial compression tests performed at 900°C, 50 s^{-1}, and 1000°C, 10 s^{-1} and 100 s^{-1}, were deemed invalid based on the calculated shape coefficients. These shape coefficients are listed in Appendix B-2. Data associated with test specimens deemed invalid are not included.

The flow curves for 304L SS are shown in Figure 3-3. These curves are characteristic of deformation curves for typical fcc and low stacking fault energy metals. During deformation, particularly during the hardening stage (referred to as either strain or work hardening), energy is stored within the metal in the form of dislocations [25, 31, 32, 34, 35]. This portion of the curve

is represented in Figure 3-3 by the exponential increase of stress after yielding. In this portion of the curve, work hardening and recovery occur simultaneously, called dynamic recovery (DRV). The onset of dynamic recrystallization, DRX, occurs at peak strain where flow stress begins a gradual decent from the peak stress [25, 31, 32, 36].
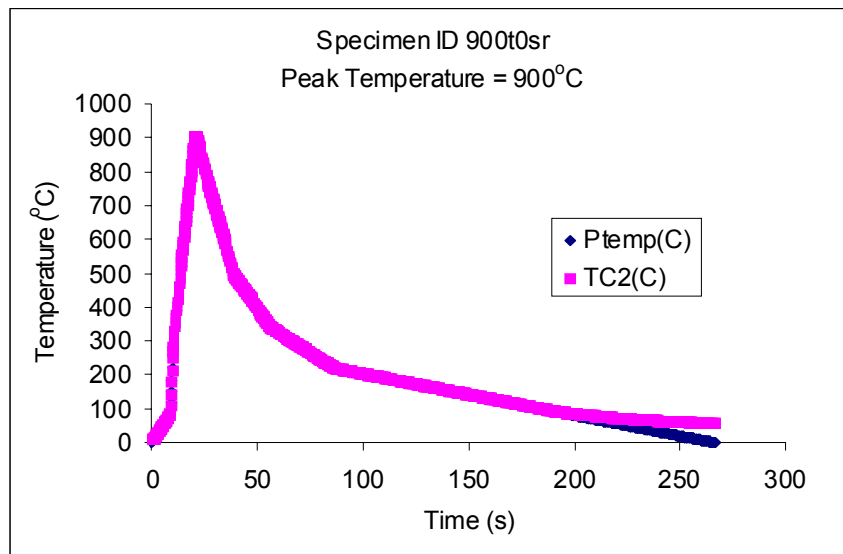
Figure 3-2 Plot of the programmed and measured thermal profile for the thermal-only specimen at peak temperature 900˚C. Similar results were observed at 1000˚C and 1100˚C.

3.5.1.2 Thermomechanical Simulations

The maximum flow stresses ranged from 309 -310 MPa at 900˚C, 222 - 229 MPa at 1000˚C, and 122 - 210 MPa at 1100˚C. At 900˚C, the flow curves at 10 s^{-1} and 100 s^{-1} both exhibit similar flow characteristics; both experiencing a relatively small amount of softening but

not sufficient for complete recrystallization. While at 1000˚C, 50 s^{-1}, and 1100˚C, 10 s^{-1}, 50 s^{-1}, and 100 s^{-1}, a greater extent of softening is evident.

The flow curves were further analyzed by plotting the strain hardening rate ($\delta\sigma/\delta\varepsilon$) as a function of flow stress, σ (shown in Figure 3-4). Characteristic segments of the work hardening curves, as reported by others [25, 31, 32, 36] are observed. The linear segment of these curves where the work hardening rate decreases with increasing flow stress is due to dynamic recovery [37]. Dynamic recrystallization becomes active at a critical stress (σ_c) value. This critical stress values is observed at point where the last downward inflection point takes place prior to dropping to zero. The flow stress at which the work hardening rate is equal to zero is called the peak stress (σ_p). At this peak stress level, all restorative processes, strain hardening, recovery and recrystallization, are in equilibrium with each other. The corresponding critical stress and peak stress for each curve are indicated in Figure 3-4.

For this set of curves, all but one curve exhibited dynamic recrystallization. The specimen compressed at 900˚C, 10 s^{-1} did not exhibit a downward inflection to zero but rather reached saturation stress that results from DRV alone in the absence of DRX [25, 32]. Additional qualitative observations suggest that the critical and peak stresses are highest at 900˚C and tend to decrease with increasing peak temperature. This trend is in agreement with trends reported by others for 304 and 304L SS [25, 34]. Linear regression analysis was performed to determine if there are any correlations exist between critical stress and peak stress to grain size and hardness.
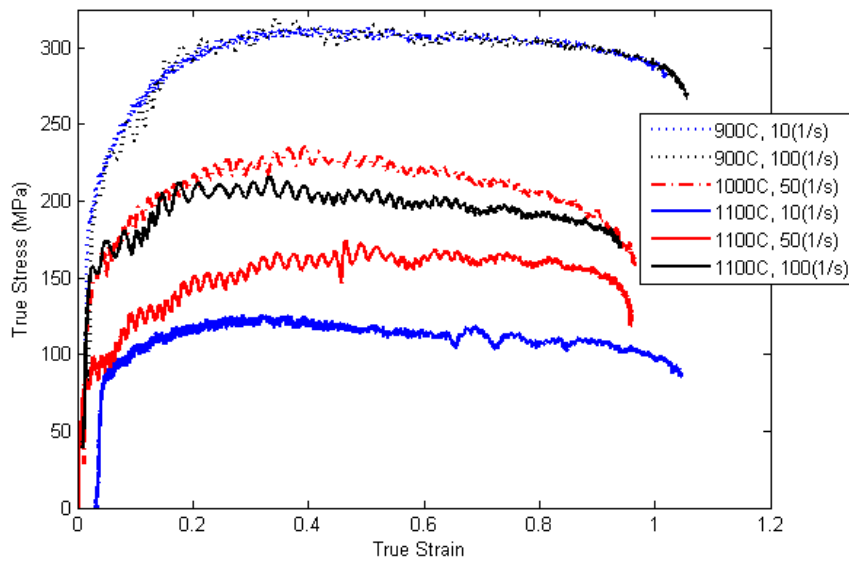
Figure 3-3 Flow stress curves generated from hot compression tests for 304L SS as a function of peak temperature and strain rate.
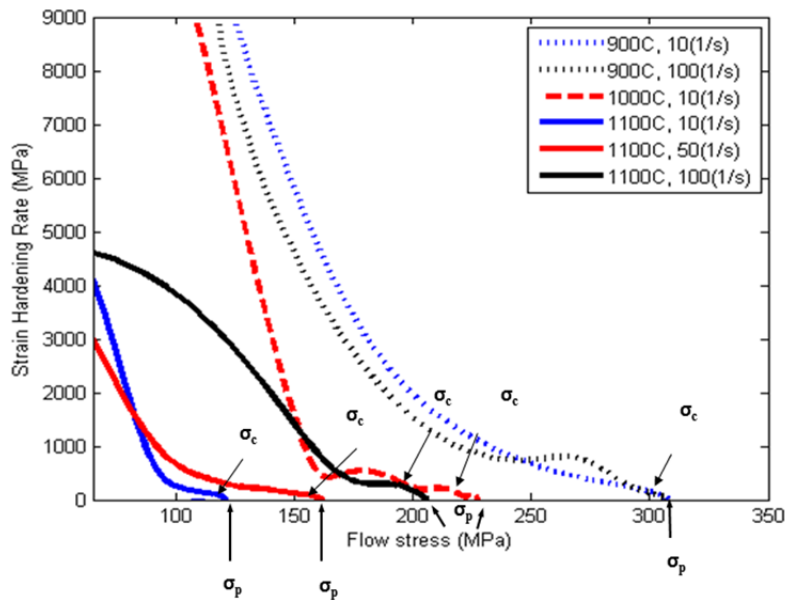
Figure 3-4 Strain hardening rate (δσ/δε) as a function of flow stress for 304L SS obtained at various peak temperatures and strain rates

The first linear regression analysis evaluates peak strain with strain rate and temperature as predictors. Appendix B-3 shows the regression output summary results which indicate a poor model fit (R^2 is 0.04). Strain rate and temperature are not good predictors of peak strain.

Figure 3-5 (a) and (b) show peak strain as a function of strain rate and temperature, respectively. Peak strain decreases with increasing temperature at low and high strain rates (see Figure 3-5 (b)). In both plots, inconsistencies are noted for data obtained at a strain rate of $50s^{-1}$. This may be due to invalid shape coefficient values for those tests (see Appendix B-2).

Similar plots to those generated for peak strain were generated for peak stress. Figure 3-6 (a) shows an increase in peak stress as strain rate increases, however, to a much less extent at 900°C indicating that peak stress is not sensitive to changes in strain rate at lower temperature regimes. Peak stress decreases with increase in deformation temperature (see Figure 3-6 (b)). Regression analysis was performed to quantify the effect of strain rate and temperature on peak stress, regression analysis.

Regression output summaries are contained in Appendices B-4 and B-5. The first analysis performed included both temperature and strain rate as predictors. Of these two variables, the model indicates that temperature is deemed a good predictor of peak stress while stain rate is not statistically significant. This linear regression model has a high R^2 value of 0.9311 even in the presence of an insignificant variable. In light of the insignificant variable, a second regression model was performed only using temperature as a predictor for the model. The output summary in Appendix B-5 indicates that while temperature is a good predictor of peak stress, the adjusted R^2 value decreased (0.8307 vs. 0.8851) from that generated in the previous model which included an insignificant variable. Thus, the first model which includes a

non-significant variable of strain rate provides a better model for describing the relationship for peak stress. The model for peak stress can be expressed as follows:

$$\sigma_p = 926.80 - 0.7170(T_p) + 0.4868(\dot{\varepsilon})$$ (3-1)

where σ_p is peak stress, T_p is peak temperature and $\dot{\varepsilon}$ is strain rate. The trends generated by this model agree with general trends described by [32] for 304 SS which show that σ_p increases as the deformation temperature decreases and strain rate increases.
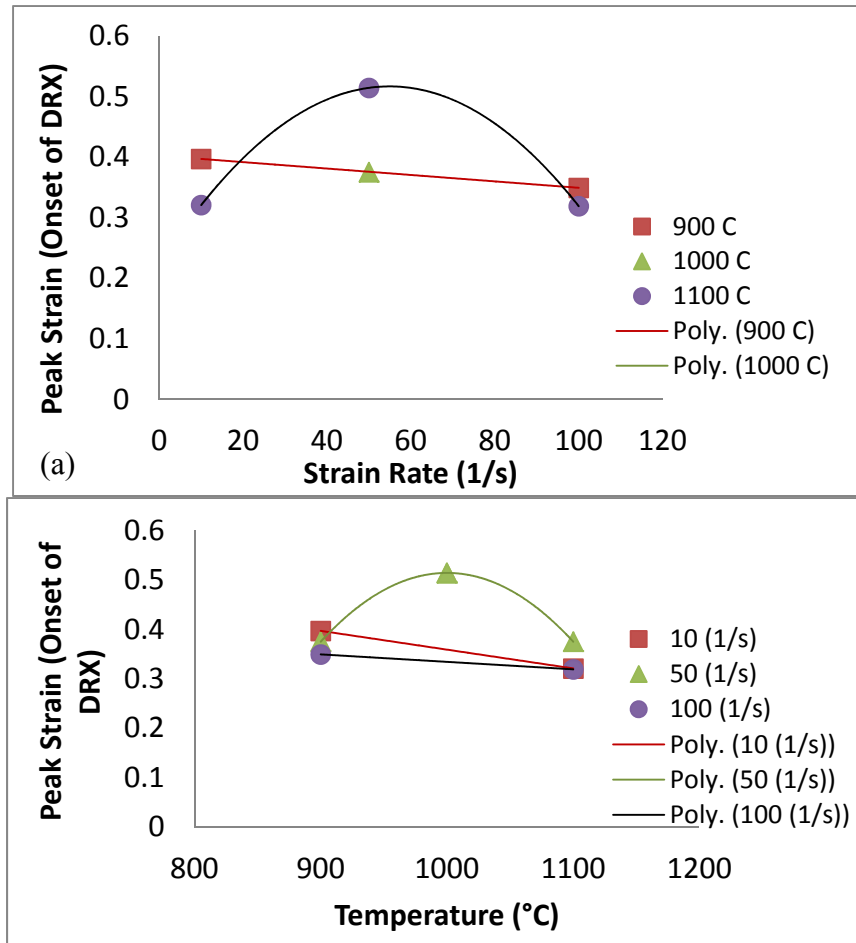
Figure 3-5 Peak stress as a function of (a) strain rate and (b) temperature.
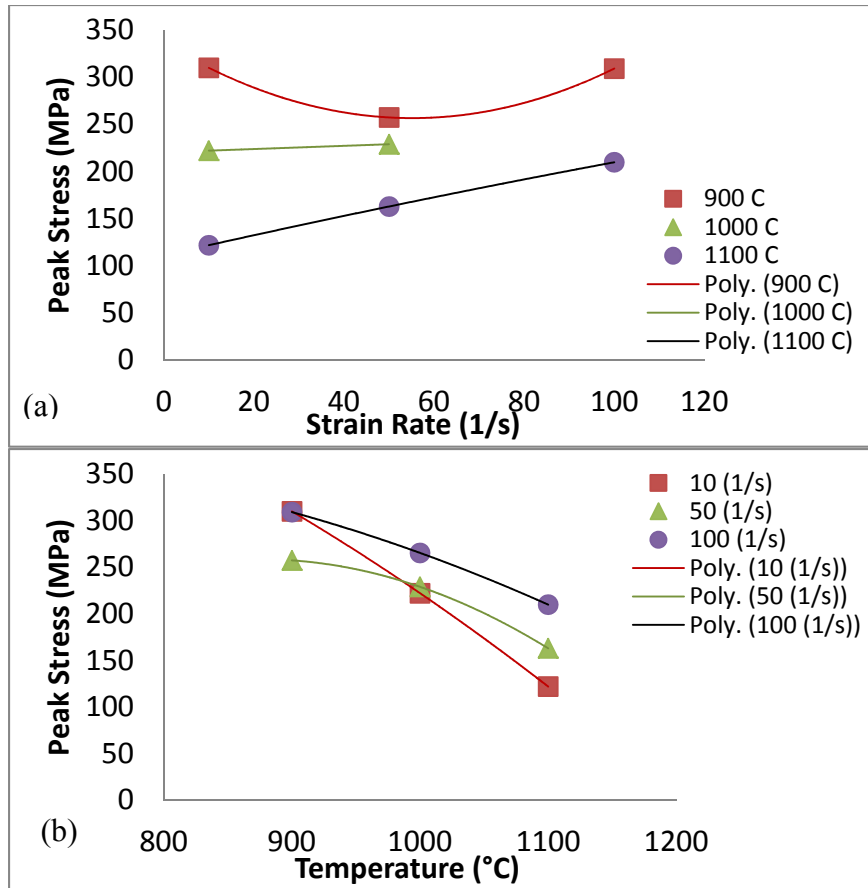
Figure 3-6 Peak stress as a function of (a) strain rate and (b) deformation temperature.

3.5.2 Metallography, Electron Backscatter Diffraction and Orientation Image Microscopy (EBSD-OIM)

3.5.2.1 Base Metal

A micrograph of the base metal is shown in Figure 3-7 (a). Base metal metallographic evaluation exhibited large grains, annealing twins, ferrite stringers aligned along the rolling direction, lath-like structure and dark, blocky microconstituents. Figure 3-8 shows a magnified view of the lath-like and blocky microconstituents observed in the base metal. Representative microconstituent regions were subjected to Vicker's hardness indentation to evaluate relative hardness differences between the different microconstituents observed. The highest hardness is

observed in the needle-like feature, the blocky microconstituents had a mid-range hardness value of 175 Hv, while the austenite "clean" baseline metal had the lowest hardness of 159 Hv.

Several researchers have identified microconstituents that tend to form in 304 stainless steels. Padhila et al. [38], mentions that two types of martensite may form in austenitic stainless steels, ά-(bcc ferromagnetic) and ε-(hcp, paramagnetic) martensite. The presence of ά-martensite, a magnetic, body-centered cubic (bcc) microconstituent, has been observed in lean grade austenitic SS by several researchers [34, 38-40]. These authors have attributed the formation of these microconstituents to the stress-state produced by the cold-rolling process (deformation), stacking fault energy of the material, temperature (relative to the chemical composition dependent martensite start temperature, M_s) and the metastable austenite phase of this alloy (primarily due to the low carbon content and other alloying additions) [41]. Padhila et al. indicates that the formation of martensite in this alloy is not generally expected upon cooling since the M_s temperature is low (below 0°C). However, precipitation to the grain boundaries depletes the surroundings grains of carbon and chromium which increase the M_s temperature to temperatures well above room temperature enabling ά-martensite formation at room temperature or above.

Barbucci et al. [39] confirmed the presence of ά-martensite in 304 SS using transmission electron microscopy (TEM) methods, X-ray diffraction (XRD) and magnetic measurements using a Faraday balance. TEM diffraction patterns revealed a face centered cubic (fcc) ϓ-austenite structure for an annealed specimen (no second phase present) and an fcc and bcc diffraction pattern for a cold-rolled specimen with second phase present. XRD analysis of both these specimens validated the presence of fcc and/or bcc structures within the corresponding specimens.
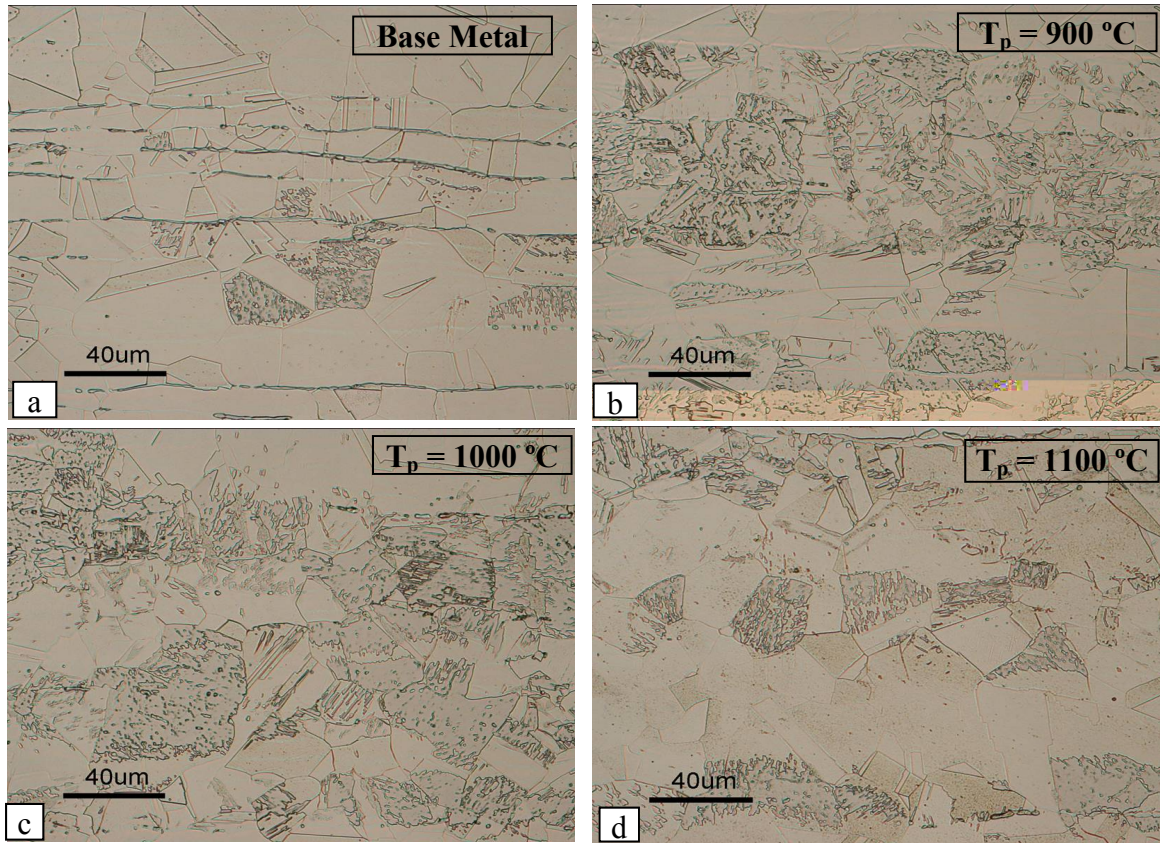
Figure 3-7 Micrographs showing microstructure (a) of the unaffected base metal and of thermally-cycled specimens at peak temperatures of (b) 900°C, (c)1000°C, and (d)1100°C.
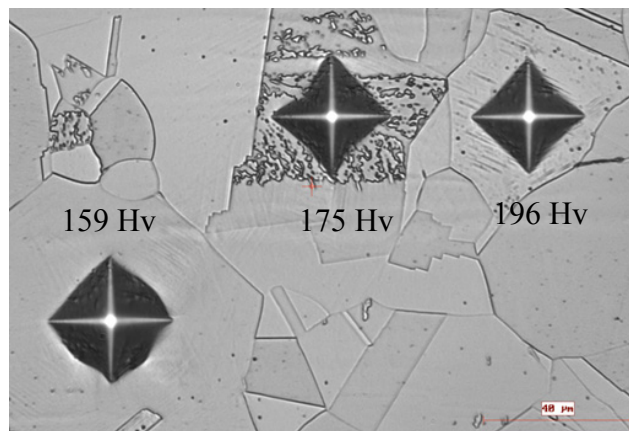
Figure 3-8 Micrograph showing hardness values of three microstructurally-distinct regions in 304L base metal used in this study.

Figure 3-9 shows the resulting XRD pattern for the base metal specimen used in this study.   The XRD pattern shows both fcc and bcc peaks which are identical to XRD results by [39]. The magnetic characteristic of the ά-martensite was detected using a handheld magnet in this specimen as well. These results confirm the presence of ά-martensite in the starting base metal from cold working during fabrication processes.

3.5.2.2 Thermal-Only

The microstructures observed for the thermal-only specimens heated to 900ºC, 1000ºC and 1100ºC are shown in Figure 3-7 (b), (c) and (d), respectively. Observations of resulting microstructures at $T_p = 900ºC$ and $T_p = 1000ºC$ show an increase in both the grain size and the amount of second phase relative to the base metal and a slight increase at 1000ºC than at 900ºC. The increase in grain size and the amount of second phase present for specimens at $T_p = 900ºC$ and $T_p = 1000ºC$ must be primarily a function of temperature since alloy composition and heating and cooling rates were constant. The grain size at $T_p = 1100ºC$ is approximately equal to that of the base metal and smaller than those observed at $T_p = 900ºC$ and $T_p = 1000ºC$. The amount of second phase present observed in the $T_p = 1100ºC$ specimen is greater than the amount observed in the base metal but less than the amounts observed at the other two lower peak temperatures.

To understand this phenomenon related to the presence and extent of second phase formed, two base metal specimens were annealed and evaluated. The annealing temperature and time at temperature were selected based on the ASM Handbook [41] recommendation for an effective heat treatment of this alloy. The recommended holding time is 3 to 5 minutes per 2.5

mm of thickness recommended annealing temperature ranged from 1010ºC - 1120ºC. The ASM handbook mentioned that cooling from annealing temperatures must be rapid to prevent precipitation. However to test the sensitivity of cooling rates to precipitation and ά-martensite formation, intermediate and slow cooling rates were selected
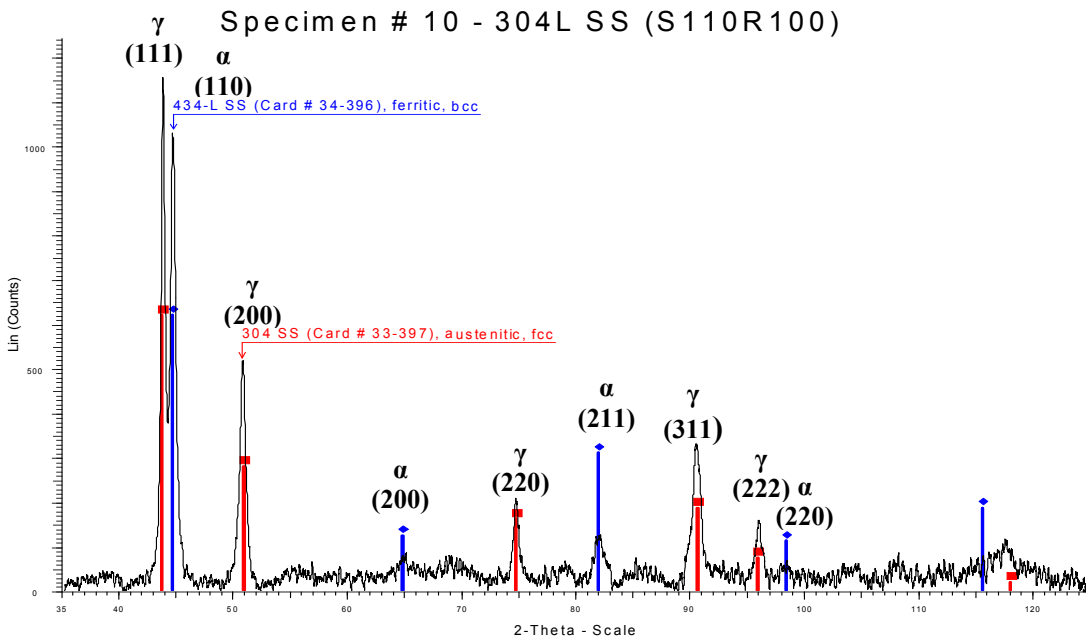
Figure 3-9 X-ray diffraction (XRD) pattern of the 304L SS base metal. Austenite (γ) and ferrite (α) peaks are marked and identified with their respective crystallographic indices.

Two 0.246 in (6.25 mm) diameter, 0.25 in (6.4) mm long specimens were heat treated. One specimen was furnace heated to 1100ºC for 15 minutes then air cooled while the other specimen was furnace heated to 1100ºC for 15 minutes then allowed to furnace cool. The resulting microstructures are shown in Figure 3-10 (b) and (c) respectively along with the base metal microstructure. Qualitatively speaking, the grain size and amount of second phase in the

79

intermediate-cooled and the slow-cooled specimens increased substantially compared to the base metal. The furnace-cooled specimen appears to have a slightly greater area of second phase formation than the intermediate-cooled specimen. Although hardness measurements are not representative of the average hardness, the individual hardness measurements in Figure 3-10, show a similar trend with respect to hardness. The second-phase has a higher hardness relative to the austenite grain as would be expected for a martensitic phase.

Experimental studies by Padilha et al. and others[38, 42] show that ά-martensite reverts back to austenite during annealing above the AISI 304 SS ά-martensite (~200ºC) and ά (~400ºC) stabilization temperatures. In some studies [42] ά-martensite reverted to austenite in as little as 2 minutes at 600ºC. In addition, Padhila discusses an interesting theory for the increase of ά-martensite content during annealing of cold-worked 304 SS between of 300 – 400ºC. He offers two plausible explanations. The first is due to a recovery mechanism that relieves stresses caused by point defects, dislocation and stacking fault defects. This recovery mechanism also provides stress relief around martensite laths and allows them to grow. The second explanation for increased ά-martensite formation is related to precipitation. Precipitation increases the M_s temperature thereby increasing the formation of ά-martensite upon cooling. He states that this latter theory is less acceptable since carbides do not form at temperatures below 400ºC.

The time at temperature above 400ºC for the thermal-only specimens cycled to $T_p =$ 900ºC, $T_p = 1000$ºC and $T_p = 1100$ºC was 36 sec, 41 sec, and 47 sec, respectively. This time at temperature is not sufficient to fully anneal and revert all ά-martensite to austenite and for the specimens heated to 1100ºC. However, some stress relief occurs that allows pre-existing ά-martensite to grow and increase the amount of ά-martensite. According to Padilha, partial-

solutionizing to high temperatures would have increased the M_s temperature thus increasing the

formation of ά-martensite upon cooling.
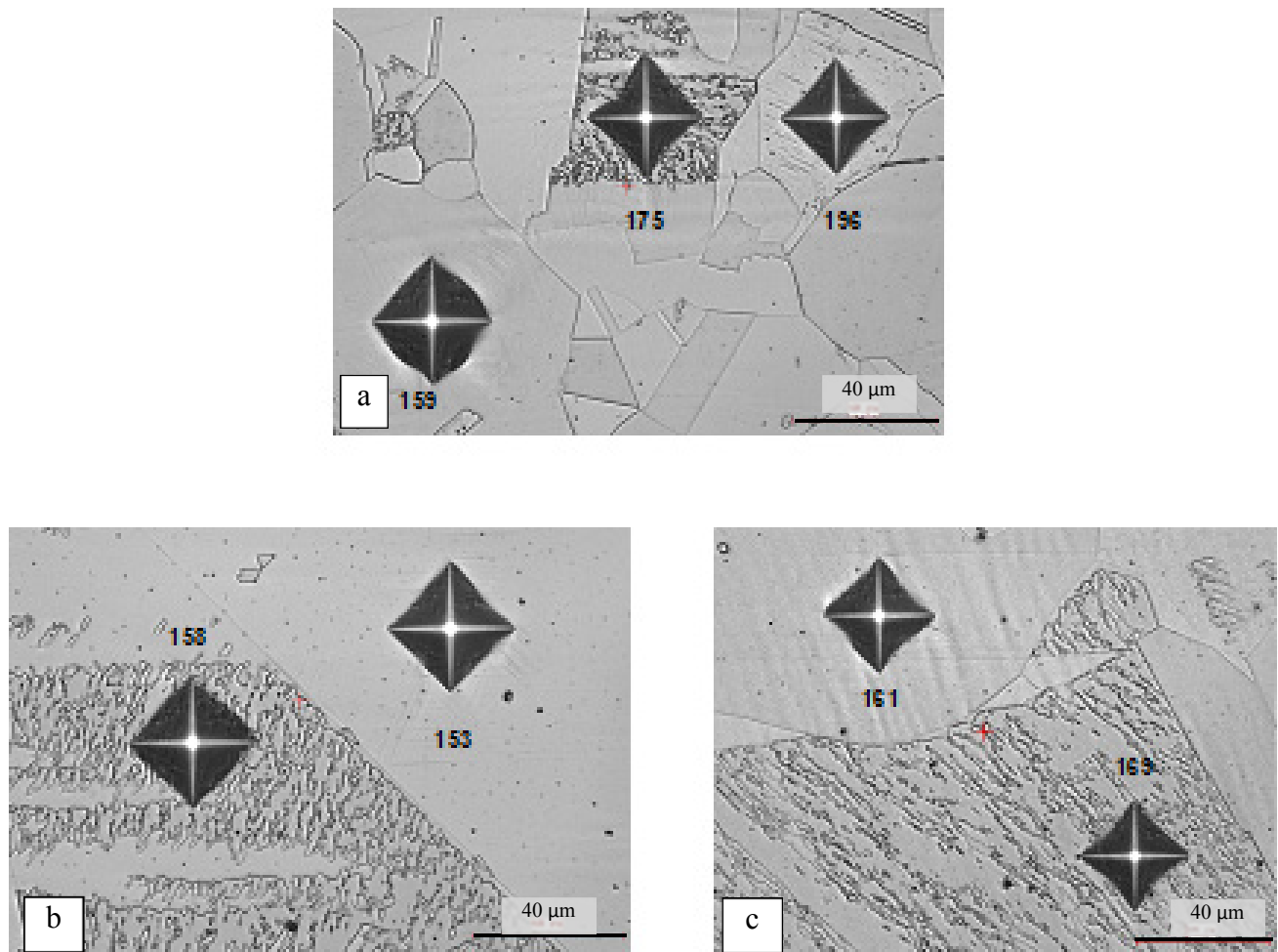
Figure 3-10   (a) Base metal (top center), (b) solution annealed at 1100°C for 15 minutes then air cooled (bottom left) and (c) furnace heated to 1100°C; held at peak temperature for 15 minutes then furnace cooled

3.5.2.3 Thermo-Mechanical Simulations

The microstructures observed at 900˚C and 1100˚C are consistent with the flow stress behavior in Figure 3-3. The microstructures of specimens compressed at deformation temperature of 900˚C, shown in Figure 3-11 (a) and (d) reveal highly deformed grains that are elongated in the flow direction.

Figure 3-11 (a) shows no evidence of recrystallization while Figure 3-11 (d) does show evidence of formation of small recrystallized grains at grain boundaries. The recrystallized grains are indicated by arrows in Figure 3-11 (d). Several authors [36, 43] characterize the evolution of microstructure with increasing strain during dynamic recovery as starting with a homogenous distribution of dislocations, resulting from dislocation multiplication, that rearrange themselves into elongated cells that eventually become elongated subgrains within the deformed grains as misorientation increases. This corresponds well to flow curve behavior exhibited in Figure 3-3 at 900˚C.

At 1100˚C, the micrographs, shown in Figure 3-11 (b), (d), (f), exhibit recrystallized, equiaxed grains that correlate well with their respective flow curves in Figure 3-3. Several authors [25, 31, 38, 44] state that the main softening process in non-stabilized, low stacking fault steels, such as 304L stainless steel is recrystallization and recovery plays a minor role. This revelation is particularly true at deformation temperatures greater than 900˚C.

This study shows that dynamic recovery is the active softening mechanisms at 900°C and low strain rates while dynamic recrystallization becomes the overriding softening mechanism at higher temperatures and strain rates.
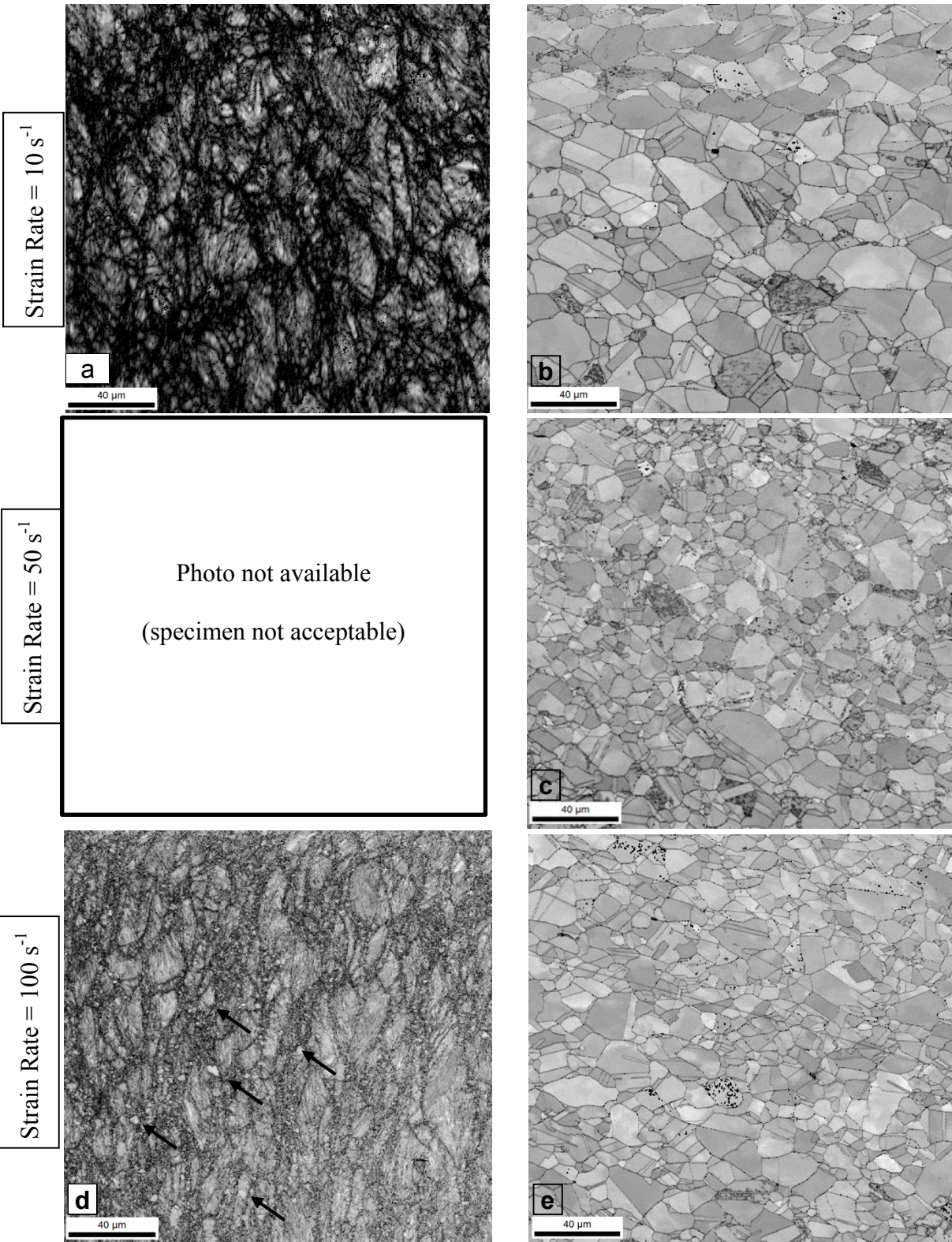
Figure 3-11 SEM Micrographs of specimens after hot uniaxial compression at (a) 900°C, 10s⁻¹, (b) 1100°C, 10s⁻¹, (c) 1100°C, 50s⁻¹, (d) 900°C, 100s⁻¹ and (e) 1100°C, 100s⁻¹.

Strain Rate = 10 s⁻¹

Strain Rate = 50 s⁻¹

Photo not available

(specimen not acceptable)

Strain Rate = 100 s⁻¹

83

3.5.2.4 Grain Size

Using OIM software, grain sizes were obtained from the scanned area for each of the test specimens and listed in Table 3-3. These data were plotted as a function of strain rate and temperature in Figure 3-12. Trends are observed at the low and higher deformation temperatures.

Table 3-3 Grain Size of Scanned Areas as Determined by OIM

Temperature (°C)	Strain Rate (1/s)	Grain Size (μm)
900	10	2.1±2.7
900	100	1.56±2.1
1000	50	6.7±7.5
1100	10	5.03±5
1100	50	3.26±2.9
1100	100	4.32±3.6

The data obtained from specimens conducted at $50s^{-1}$ appear to be outliers in this data set. The plots show a slight decrease in grain size as strain rate increases in Figure 3-12 (a) results are shown in Appendix B-8. The results indicate that while temperature and strain rate are significant predictors of hardness, the low R^2 value of 0.64 indicates that other unknown variables which fall outside the scope of this program affect hardness.

Regression analysis was performed to determine if strain rate or peak temperature were good predictors of grain size. Regression output summaries for analyses performed on data set without data for test conducted at $50s^{-1}$ are in Appendix B-6 and Appendix B-7. Appendix B-6
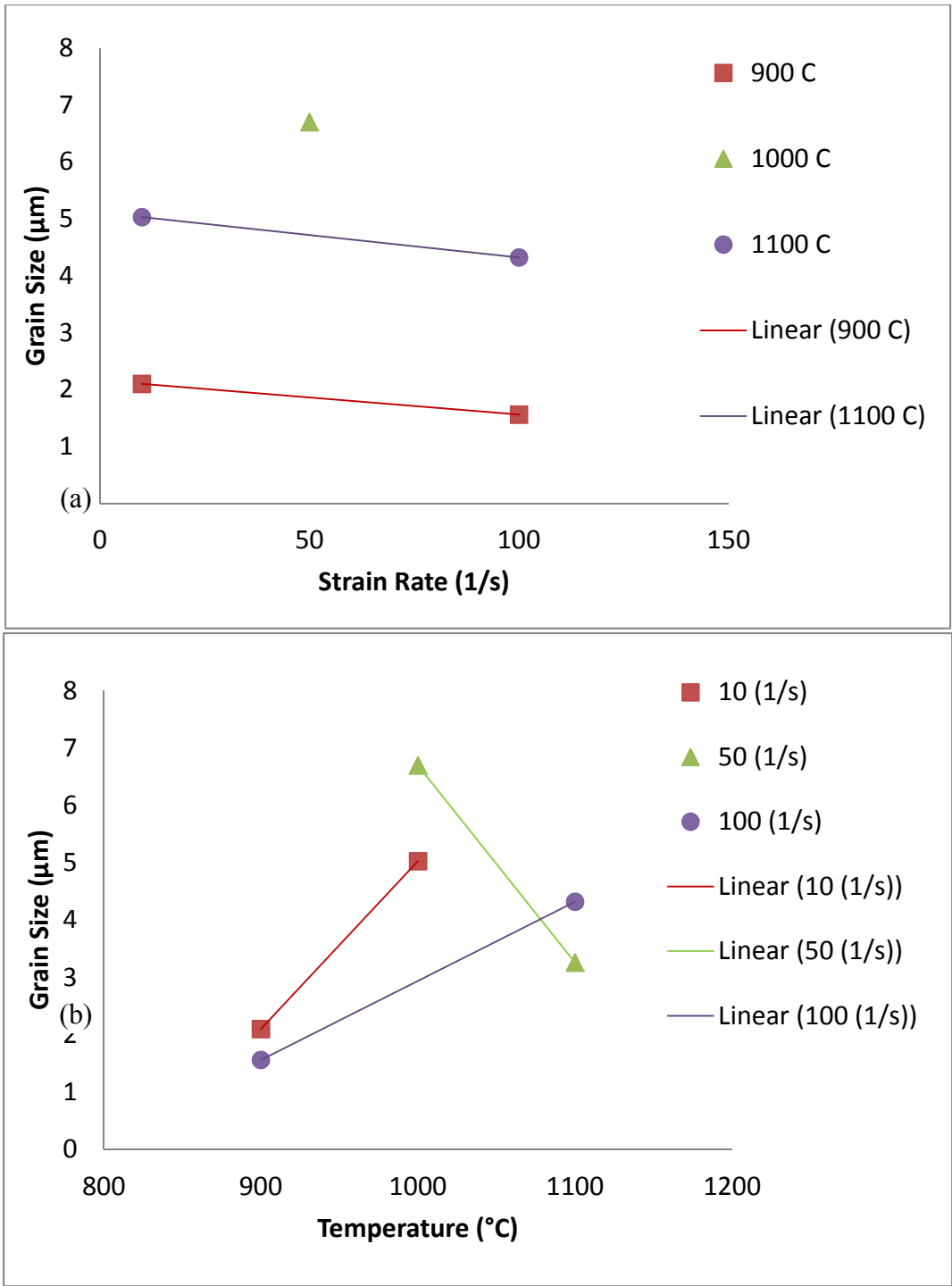
Figure 3-12 Plot showing gain size as a function of (a) strain rate and (b) temperature.

contains the regression summary as a function of temperature and strain rate. The regression

model has a high R^2 value of 0.9991 and indicates temperature is significant and that strain rate

is not a significant predictor of grain size. The regression analysis was run again with

temperature only (see Appendix B-7). The results from this model indicate that while this model

had a good R^2 value (R^2 value = 0.9531) its adjusted R^2 value (0.9297 vs. 0.9974) was less than

the previous model which included strain rate. Thus, the model for grain size should include

both terms to better predict grain size. The model for grain size can be expressed as:

$$Grain\ Size = -10.59 + 0.0142(T) - 0.0069(\dot{\varepsilon}) \tag{3-2}$$

The trend expressed by Equation (3-2) is in agreement with experimental work conducted

by other authors [24, 25] that have evaluated recrystallized grain size above the steady-state

temperature. Their results indicate grain size is strongly dependent upon stress which is a

function of both temperature and strain rate. Kim et al. [24] noted that the DRX grain size in 304

SS decreased with decreasing temperature and increasing strain rate.

3.5.3   Hardness

The average hardness data of compression specimens is shown in Table 3-4.

Backward stepwise regression analysis was performed to determine if strain rate, temperature,

their squares and/or their cross-products were good predictors of average hardness. Figure 3-13

plots measured versus predicted average hardness as a function of strain rate and temperature.

The regression results show some correlation of hardness to strain rate and temperature but the

fit is not perfect suggesting that there are other unknown variables outside the scope of this effort

that affect hardness.

**Table 3-4 Table of Average Hardness for Hot
Iso-thermally Compressed Specimens**

	900 °C	1000 °C	1100 °C
0 s^{-1}	195.7	182.2	164.9
1 s^{-1}	244.2	176.7	179.2
10 s^{-1}	195.1	215.7	186.9
50 s^{-1}	258.25	176.12	188.6
100 s^{-1}	259.7	226.8	190.5
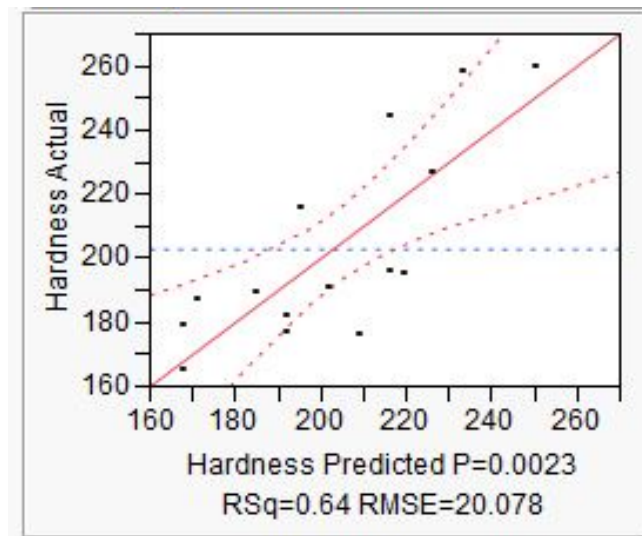
**Figure 3-13 Measured versus predicted average hardness as a function of strain rate and
temperature.**

3.6   Conclusions

Physical simulations were performed on 0.25 in (6.40 mm) diameter 304L SS cylindrical

specimens using a Gleeble 1500 thermomechanical simulator.   These physical simulations were

programmed on the Gleeble system to follow both thermal thermomechanical profiles at strain

rates of 10s^{-1}, 50s^{-1}, and 100s-$^{-1}$ each at peak temperature of 900˚C, 1000˚C, and 1100˚C. The

flow stress curves and their related metallography were evaluated as a function of strain rate and temperature. The following observations were made:

(1)   The Gleeble system can be used to adequately simulate thermal profiles that are representative of actual friction stir thermal cycles within 0.1234±0.911°C/s of the programmed temperature profile for the majority of the test.

(2)   The primary softening mechanism for specimens deformed at 900°C was dynamic recovery while dynamic recrystallization was the overriding softening mechanism at higher deformation temperatures.

(3)   A regression model was developed to predict peak stress as a function of temperature and strain rate. The model shows that σ_p increases as the deformation temperature decreases and strain rate increases.

(4)   A regression model was developed for grain size that shows its relationship to temperature and strain rate. The model indicates that grain size decreased with decreasing temperature and increasing strain rate. Similarly, since peak stress is a function of temperature and strain rate, a regression model was also developed that shows grain size dependence on peak stress.

(5)   Temperature and strain rate are correlated with hardness, however, there are other unknown variables that should be included to increase model fit. Further studies are recommended to understand the relationship between the presence and distribution of this second phase to grain size, flow behavior, strain rate sensitivity, strain hardening and softening mechanisms. In addition, future studies should also account for effects of adiabatic heating in their evaluation, particularly at high deformation rates. Simulations and Comparisons against experimental data.

4 SIMULATIONS AND COMPARISONS AGAINST EXPERIMENTAL DATA

4.1 Abstract

Isaiah, an existing 3-dimensional finite element code developed by Cornell University is evaluated by comparing model predictions against experimental and physically-simulated data to determine how well the code output relates to real friction stir (FS) data over a range of nine processing conditions. Physical simulations replicating select thermo-mechanical streamline histories were conducted to provide a physical representation of resultant metallurgy and hardness. Isaiah predicts qualitative trends over a limited range of parameters and is not recommended for use as a predictive tool but rather a complimentary tool, particularly if weld data can be used to calibrate the model. Once properly calibrated, the Isaiah code is a powerful tool to gain insight into the process for the range over which it was calibrated.

4.2 Introduction

Friction stir welding/processing is a thermal and thermomechanical process that involves severe plastic deformation within the stir zone. Strain, strain rate and temperatures are tightly coupled during this process. Often times the real source of uncertainty is the lack of understanding of boundary conditions at the tool to workpiece interface. These complexities have driven the development of a large number of FS models that simulate various aspects of the process. Examples of the disparities in FS models and results are presented in the next section.

Most models developed have been validated primarily for aluminum alloys with relatively small amounts of experimental data. Fewer models have been validated for steels or stainless steels, particularly since FSW of steels and stainless steels have proven more challenging than aluminum alloys.

Some research efforts have also investigated the use of the Gleeble system to physically-simulate predicted thermomechanical histories to replicate microstructure and hardness values of the stir zone (SZ), thermal mechanically affected zone (TMAZ) and heat affected zone (HAZ). Hot torsional and compression tests conducted under predicted FS thermomechanical histories have been successful in reproducing microstructures and hardness values that are comparable to experimental welds. However, physical simulations have never been used to evaluate the validity of constitutive equations.

This chapter presents model simulation results over nine processing conditions as well as physical simulation results of select streamlines. Model simulation results are evaluated to provide a qualitative and quantitative assessment of how accurate predicted trends are relative to experimental data. Physical simulation results are evaluated to provide a physical metallographic representation of specific thermomechanical histories to assess predicted state variable evolution against physically simulated hardness. Gleeble flow stress results are compared against those of predicted streamline flow stress to evaluate how well internal constitutive models describe plastic flow stress behavior.

4.3   Previous Work

Seidel and Reynolds [45] presented a 2-D Eulerian material flow model using Fluent, a commercial computational fluid dynamics (CFD) package. The authors assumed laminar fluid flow past a featureless rotating cylinder with pure plastic deformation and no strain hardening. The Zener-Hollomon equation was used to model the flow stress behavior of the material. This model was able to replicate experimental tracer material flow experiments in an aluminum alloy

which demonstrated that material was swept from the advancing side around the retreating side and back to the starting position on the advancing side then trailed behind the tool under optimum operating conditions.

Colegrove and Shercliff [46-48] used Fluent to model heat transfer and material flow in two and three dimensions to describe effects of various tool shapes. In the 2-D modeling effort, the authors used two modeling approaches to describe the boundary conditions at the tool-to-workpiece interface. One approach used the Johnson-Cook model to describe the materials' flow stress using a "stick" boundary conditions (i.e., the shear stress was below a limiting shear stress value) and an experimentally-derived flow stress values using a "slip" boundary condition (i.e., shear stress exceeded the limiting shear stress value and was truncated to a limiting value). The main difference noted between the two constitutive models was the amount of scatter observed on particle traces. The Johnson-Cook model exhibited a greater amount of scatter relative to the slip boundary condition, albeit, the pressure and force predictions were similar. Their 3-D modeling efforts built upon the slip boundary condition where the material was allowed to slip against the tool and the limiting shear stress was adjusted to reflect experimentally measured weld power values.

Askari et al. [49] presented a 3-dimensional Eulerian hydro-code model that used a finite-difference approach. The model uses an elastic-plastic material model that incorporates work hardening, strain-rate dependence, and thermal softening. The Johnson-Cook plasticity theory is used to model heat transfer, material flow, and streamlines of state variables around profiled tools.

Schmidt et al. [50] presented an analytical model for heat generation based on sliding, sticking and partial sliding/sticking contact boundary conditions at the probe-to-workpiece

91

interface using Coulomb's law to distinguish between the various contact conditions. The contact boundary condition was experimentally verified by examining the relationship between plunge force and torque. The authors concluded the lack of proportionality between plunge force and heat generation is indicative of a sticking boundary condition at probe-to-workpiece interface.

WELDSIM is a 3-D finite analysis code developed by Zhu and Chao [51] for fusion welding simulations and applied to model FSW of 304L SS. The model uses an iterative inverse analysis method to numerically solve the boundary value problem for heat transfer. The temperature fields obtained from the output of the inverse analysis is used as input for the un-coupled 3-D elastic-plastic thermomechanical analysis that assumes plastic deformation of the material follows Von Mises yield criterion and the associated flow law. Comparisons between predicted and available experimental temperature and residual stress data show good agreement. The authors showed that 50% of mechanical work is converted into heat and that the maximum predicted temperature ranged between 900-1000°C located at the tool shoulder and along the centerline.

Hickory is a 2-D finite element coupled viscoplastic model developed at Cornell University and can be used in either an Eulerian or Lagrangian framework. This longstanding model was originally developed for hot temperature deformation processes such as rolling operations since the late 1970's and modified to model the FS process [52]. Owen and Sorensen [22] undertook a systematic and extensive evaluation of Hickory's performance for modeling FSW. They first performed a series of 16 model simulations to compare the model's predicted trends with other FSW trends found in the literature. The authors also performed nine model simulations and corresponding experimental runs to evaluate predicted weld deformation widths,

92

thermal histories, velocity streamlines, and hardness (represented by the state variable) using 304L stainless steel. Comparisons between the predicted and experimental results suggest that Hickory was fairly accurate in predicting temperature, velocity, hardness trends, and weld deformation width at the weld centerline for a limited parameter range after an optimization routine was implemented and under-relaxation of the state variable was imposed. Recommendations to improve the code include (1) implementation of temperature-dependent thermal conductivity values be used in lieu of a constant thermal conductivity term (2) accounting for heat loss to the backing plate, and (3) investigation of new friction laws that can accurately describe the interface boundary conditions over a larger parameter range.

Dewhurst and Dawson [53] extended Hickory to a 3-dimensional model called Isaiah in 1985 that was modified to model FSW processes. Isaiah is a finite element code that models viscoplastic deformation in either Eulerian or Lagrangian reference frame. The code assumes isotropic strain hardening. The model originally used a modified Hart's model but now uses a modified Kocks and Mecking [54] model to predict a measure of strength induced by the deformation and thermomechanical history in the process. This measure of strength is called hardness and it corresponds to the measure of dislocation density in the material. In this model, the deformation and heat transfer are used in determining the flow streamlines which can be extracted along with the thermo-mechanical history to input into a texture evolution model to look at texture.

Cho et al. [54, 55] evaluated simulated material flow patterns, strength and temperature distributions over a limited number of translational and rotation combinations using modified Hart's material model in Isaiah. Their parametric study evaluated the effect of threads on the probe, probe thread angle, the presence or absence of friction at the shoulder or probe interfaces,

and heat losses with and without backing plate. The results of their study indicate that the presence of friction on the shoulder generates a greater volume of higher temperature and hardening regimes, particularly at the surface where the shoulder is in contact with the workpiece as compared to those run with a frictionless shoulder. The axial traction components induced by the presence of threads on the probe provide vertical mixing and homogenization of the temperature and hardening distribution in the through-thickness direction. This axial traction component had a greater impact on strength rather than temperature distribution. The author speculates its impact may be greater at higher translational speeds because convection becomes the more prominent heat transfer mechanism than conduction. The author found good agreement between predicted strength and experimental hardness profile trends. Cho et al. [55] concluded that while model trends are in agreement with experimental data, the use of this program is best served as a qualitative tool for gaining insight into the process rather than for obtaining quantitative relationships.

Nandan et al. mathematically modeled 3D plastic flow and heat transfer of FSW for 6061 AA [56] , 304L stainless steel [57] and 1018 mild steel [58]. In all three papers, the authors solved equations of conservation of mass, momentum and energy in three dimensions. The model evaluated heat generation rates that were determined by considering deformation work, non-Newtonian viscosity as a function of local strain rate, temperature and the nature of the material dependent and temperature dependent thermal conductivity, specific heat and yield stress. For aluminum and 304L stainless steel, 80% of the heat generated at the shoulder and 20% from the vertical pin surface. Based on previous work by Zhu et al. [51] that showed 50% of mechanical work is converted into heat during FSW of stainless steel, the authors approximated the power input by doubling their predicted heat generation rates. Thus, the

authors predicted that power input requirements increased as rotational speeds increased at a given travel speed as well as increased as travel speeds increased at a given rotational speed. The model showed that both aluminum and 304L SS exhibited an axisymmetric temperature field while 1018 steel did not. The temperature field asymmetry predicted for aluminum and 304L SS was attributed to the motion of the tool whereby the heat supply to the cold region head of the tool is quicker than that of the preheated material behind the tool. In steel, the lack of asymmetry was attributed to the angular variation of heat generation and material flow. The asymmetry in the aluminum alloy increased at higher travel speeds. In all cases, heat generation increased further away from the axis near the shoulder where the relative velocity between the shoulder and the workpiece increased. The value of viscosity over which no significant material flow occurs is $4 - 5 \times 10^6$ Pa-s for AA6061 and 304L SS and 9.9×10^6 for 1018 steel.

Arbegast [33] used output from thermomechanical tests to develop flow stress curves as a function of temperature and strain rate for various aluminum alloys to develop constitutive relationships for use in a first-order approximation of the friction stir welding process using the architecture of hot metal working models. Using this developed FSW process model, Arbegast calculated the extrusion pressure (i.e., the force opposite the direction on travel that is exerted on the pin during friction stir welding). By comparing the extrusion pressures for each of the Al alloys investigated, the author was able to verify experimental trends observed and gain insight into the optimum processing conditions (pin tool geometry, extrusion zone width, processing parameters, and flow stress of the material) for joining various types of aluminum alloys.

Forrest et al. [59] used Hickory model to generate thermomechanical history streamlines which were used to conduct hot uniaxial compression tests in HSLA-65 using Gleeble 1500 system. The authors indicated that the 1.5 mm/mm strain capability of the system for the given

specimen length was insufficient to simulate predicted strains of 25 mm/mm of stir zone region. The authors also found that a 3-D model provided thermomechanical histories the more accurately replicated experimental HAZ microstructure and hardness. Posada et al. [60] performed a series of physical simulations over a range of strain rates and peak temperatures and was successful in replicating experimental HSLA-65 microstructure and hardness of the inner and outer HAZ regions.

Norton [61] used hot torsional tests in Gleeble 3800 system to simulate SZ microstructure in Armco Iron and HSLA-65 steels. Limitations with the applied cooling control techniques rendered some degree of mismatch between measured and physically-simulated grain size and transformation products in both steels.

Sinfield et al. [62] was successful in developing a control cooling during deformation testing and was successful in obtaining good agreement between hot torsional microstructure and hardness for the coarse grain stir zone, the TMAZ and the inner and outer HAZ regions. Sinfield indicated that numerical modeling is required to accurately predict the effective strain rate and strains because of the large temperature and deformation gradients along the gage length. With the use of DEFORM, a commercial software program that models large deformation material flow and thermal behavior for metal forming, heat treatment, machining and mechanical joining processes, the authors predicted an effective strain value of 1.7 mm/mm, strain rate of 35.22 s^{-1} and temperature of 1331°C at the coarse grain SZ region.

4.4   Method

4.4.1   Description of 3-D Finite Element Model

Isaiah is a finite element code developed at Cornell University that models heat transfer and viscoplastic flow in three dimensions using an Eulerian reference frame. This model assumes isotropic material properties, including isotropic strain hardening. The governing equations for the forming process are described elsewhere [54, 55]. These same references also describe the constitutive equations that describe material behavior associated with internal energy and plastic flow using a modified Hart's model. The viscoplastic response is described by a flow law, flow stress and a state variable evolution model as described in Equation (4-1) to Equation (4-10).

The state variable represents the quantitative measure of hardness and is proportional to the square root of the dislocation density [43, 54, 55]. Its rate dependence and saturation limit are separately determined via a Fischer factor. In this work, The Kocks and Mecking material model is used to describe the deformation history and flow properties of the material. The constitutive model uses the temperature dependent shear modulus, G, for scaling and twelve material constants. The material constants parameters were evaluated from experimentally derived data for 304L SS described elsewhere [55].

4.4.1.1 Flow Law

$$\acute{\sigma} = \frac{2\bar{\sigma}}{3\bar{D}}\acute{D} \tag{4-1}$$

where $\acute{\sigma}$ is the deviatoric Cauchy stress, $\bar{\sigma}$ is the flow stress, $\acute{D}$ is the deviatoric displacement.

4.4.1.2 Flow Stress

   Flow stress, Equation (4-2), has two main contributions, one from strength and a kinetic

term. The kinetic term has temperature and strain rate dependence. The rate sensitivity

exponent is at a fixed state and must be very small to keep the flow bands tight around the tool.

The strength component (Equation (4-3)) is scaled by the shear modulus which provides a bound

on stress over the range of temperatures. The state variable is the component accounts for strain

hardening and thermal softening (Equation (4-7)).

$$\bar{\sigma} = \tau(s,\theta)f(\theta)\left(\frac{\bar{D}}{D_0}\right)^m \tag{4-2}$$

where $\bar{D}$ is the effective deformation rate, D_0 is the constant, m is the temperature dependent

constant

$$\tau(s,\theta) = sG \tag{4-3}$$

where τ is the hardness, s is the state variable, θ is the temperature, and G is the temperature

dependent shear modulus.

$$f(\theta) = \exp\left(\frac{Q_0}{R}\left(\frac{1}{\theta} - \frac{1}{\theta_0}\right)\right) \tag{4-4}$$

where $f(\theta)$ is the thermal softening, Q_0 is the activation energy, R is the gas constant, and θ_0 is the

reference temperature

$$m(\theta) = m_0 + m_t\theta \tag{4-5}$$

$$G(\theta) = G_0 + G_t\theta \tag{4-6}$$

where $G(\theta)$ is the temperature dependent shear modulus, G_0 is the reference shear modulus

(constant), and G_t is the shear modulus at time t.

4.4.1.3 Evolution of the State Variables for Strength

Evolution of the state variable is determined by employing a modified Voce hardening equation, expressed in Equation (4-7). This equation limits the growth of flow stress from strain hardening by placing limits on state saturation value s_s.

$$\frac{D}{Dt}(s) = \frac{h_s}{G}\left(1 - \frac{s}{s_s}\right)^{n_s} \bar{D} \qquad (4\text{-}7)$$

where h_s is the material constant and n_s is the hardening exponent

$$s_s = \left(a_s + b_s \left(\frac{\tilde{\varphi}}{\widetilde{\varphi_s}}\right)^{\frac{1}{2}}\right)^2 \qquad (4\text{-}8)$$

where a_s and b_s are constants, $\tilde{\varphi}$ is the Fisher factor, and $\widetilde{\varphi_s}$ is the saturated Fisher factor.

$$\tilde{\varphi} = \frac{\theta}{G}\ln\left(\frac{D_s}{\bar{D}}\right) \qquad (4\text{-}9)$$

where D_s is a constant

$$\widetilde{\varphi_s} = \tilde{\varphi}(\theta_r, D_r) \qquad (4\text{-}10)$$

where θ_r is the reference temperature, and D_r is the reference deformation.

Material property values and constants are listed in Tables 4-1 to 4-4. The material thermal physical properties are listed in Table 4-1. The isotropic shear moduli values are listed in Table 4-2 and the Kocks and Mecking material constants for 304L SS are listed in Table 4-3 and Table 4-4.

Table 4-1 Material Parameters for the Thermal Response of Annealed 304 Stainless Steel [63]

$k_0(\frac{W}{mK})$	$\rho(\frac{kg}{m^3})$	$C_{p_0}(\frac{J}{kgK})$
22.6	7940	750

Table 4-2 Isotropic Shear Moduli for 304L Stainless Steel [63]

$G_0(GPa)$	$G_t(\frac{GPa}{K})$
84	-0.0351

Table 4-3 Kocks-Mecking Material Model Flow Stress Parameters for 304L Stainless Steel [63].

θ_o (K)	D_o (1/s)	$\frac{Q_o}{R}(K)$	$\frac{Q_1}{R}$	m_o	m_1(1/K)
1173	1.0	300	--	0.02	$3.0e^{-5}$

Table 4-4 Kocks-Mecking Material Model Basic State Variable Evolution Fit Parameters for 304L Stainless Steel [63].

h_s	n_s	a_s	b_s	D_s (1/s)	θ_r (K)	D_r (1/s)
$5.0e^9$	6	0.1676	-0.0782	$1.0e^7$	1000	1.0

4.4.2 Mesh

The mesh used for simulations in shown in Figure 4-1 and is comprised of 28,944 hexahedral elements and 387,039 nodal points. The greatest concentration of elements surrounds the shoulder and probe where thermal and velocity gradients are expected to be the steepest. The mesh dimensions consist of a 2.14 in (54.6 mm) square width and extended length equivalent to approximately one shoulder radius in length along the travel direction. The depth of the mesh is 0.25 in (6.4 mm).
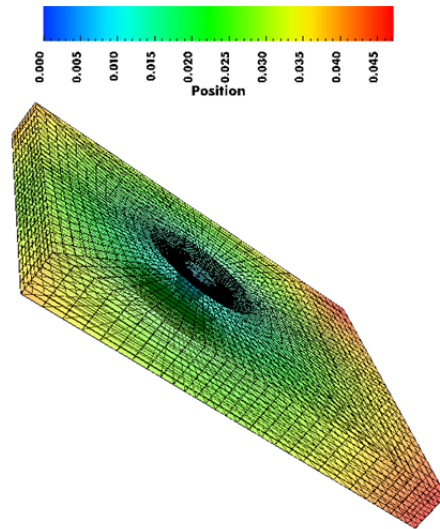
Figure 4-1 Illustration of 3-D mesh.

The computational domain represented the experimental trials to the extent possible. The tapered probe and convex shoulder geometry was modeled after the E44016 tool design, the tool used in experimental trials (modeled without threads), that is partially penetrated into the workpiece. The probe is embedded approximately 0.17 in (4.32 mm) into the domain and the shoulder is also partially engaged, similar to experimental processing trials. Tool tilt is 0 degrees. Rotating boundary conditions are defined at the points connecting the tapered shoulder to the base of the tapered probe and at the probe tip. Since the probe is partially-penetrated, the surface below the probe tip serves as a backing anvil.

The domain is defined by ten surfaces. The material enters the control volume with known properties, temperature and state through surface 1 and flows past a stationary but rotating probe then exits through surface 3. The modeled tool rotation is clockwise rendering an advancing and retreating side as shown in Figure 4-2. The boundary conditions at each surface are listed in Table 4-5.
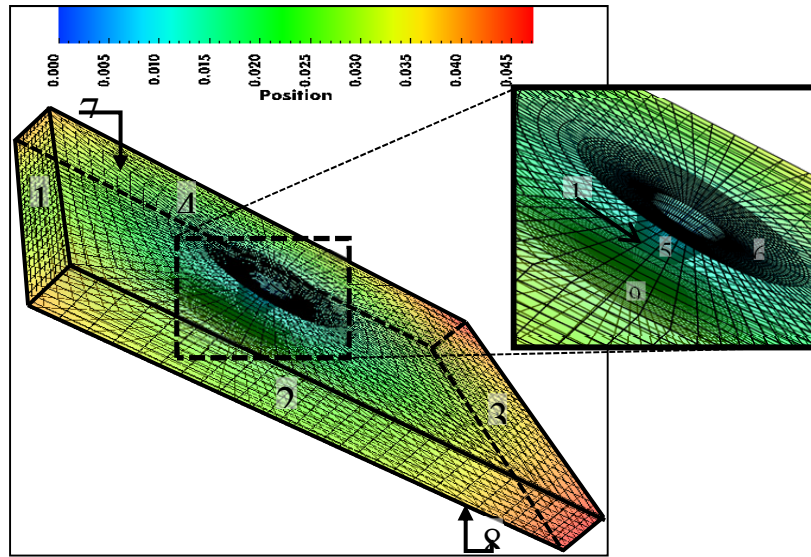
Figure 4-2 Schematic of computational domain showing all 10 surfaces. Material enters through side 1 and exits through side 3.

Table 4-5 List of Specified Boundary Condition at Each Surface

Surface Number	Surface Description	Boundary Condition Specified	Initial Temperature (K)	Convection Coefficient $(\frac{W}{m^2K})$	Other Values
1	Inlet	Initial θ and SV	300	—	SV$_i$ =0.0025 θ = 300 K
2	Lateral	Adiabatic	—	—	—
3	Exit	Adiabatic	—	—	—
4	Lateral	Adiabatic	—	—	—
5	Probe	υ diff friction BC Convection heat transfer	1023	1000	fc=$45e^8$
6	Shoulder	Coulomb friction BC	1023	1000	fc=0.4
7	Top	Natural convection	300	100	—
8	Bottom	Convection	300	1000	—
9	Bottom shoulder	Convection	500	1000	—
10	Probe bottom	Convection	1023	1000	—

where θ = temperature, u = velocity, BC = boundary condition, SV$_i$ = initial state variable and fc = friction coefficient.

4.4.3 Friction Models

Three basic friction laws can be modeled. These include sticking, sliding, and Coulomb friction models. In this study, only sliding and Coulomb friction models are employed. The sliding friction model employs a velocity difference model which uses a constant times the velocity difference between the tool's effective tangential velocity, u_{tool}, and the material's tangential velocity, u, thus the traction vector is proportional to velocity difference as expressed in Equation (4.11).

$$\bar{T}_t = \beta \cos \varphi \, (u_{probe} - u)_t \qquad\qquad (4\text{-}11)$$

where the subscript, t, represents a tangential component, β is a coefficient which can either be scaled or unscaled (i.e., independent of the yield stress of the material) and φ represents the angle of material directionality resulting from probe treads. Threads are not used in these model simulations.

The second is Coulomb's law of friction, Equation 4-12, which is a function of traction. Traction is a unit vector value whose direction is in the direction of the velocity difference. Both friction laws are used as described in the following paragraphs.

$$\bar{T}_t = v \cos \varphi \, T_n sign(u_{probe} - u)_t \qquad\qquad (4\text{-}12)$$

For simulations described in this paper, the velocity difference friction law using an unscaled friction coefficient constant is used to describe the friction condition at the probe interface since its tangential velocity is small relative to the shoulder's. The friction coefficient value was determined after performing a large number of simulations using different friction coefficients over the entire range of processing conditions. Simulations conducted using a friction coefficient value of $45x10^8$ converged to a solution for temperature, velocity and state at all nine processing conditions and trends across processing seemed reasonable. The model did

not converge to a solution for one or all three output response variables and for values that did converge, the magnitude of individual processing conditions were unreasonable and did not correlate with expected trends. The detailed results from those series of simulations will not be discussed herein.

Since the radial difference between the outer and inner shoulder diameters is relatively large compared to those of the probe, the velocity difference friction law is not ideal for modeling the friction condition at the shoulder since its effect would dominate any effect at the probe interface. Instead, the Coulomb friction law is used to describe the friction condition at the shoulder interface since tool velocity can either be a constant or a function of the radius.   The value used for Coulomb friction coefficient is 0.4 [63].

4.4.4   Description of Parametric Study

A series of simulations were conducted over a set of processing conditions that consisted of three rotational speeds (300, 400 and 500 RPM) and three translational speeds, (2 IPM (0.85 mm/s), 4 IPM (1.69 mm/s) and 6 IPM (2.54 mm/s)). Temperature, power and X-force trends were evaluated and compared against experimental data.

4.4.5   Physical Simulation of Select Streamlines

Thermomechanical histories of select streamlines were simulated in a Gleeble 3500 system. Because of Gleeble specimen geometry, the streamline thermomechanical histories were limited to those with a total strain of 1.   One streamline each was selected from simulations at a

low and high RPM, both at 2 IPM.   The streamline selected in both cases is located on the retreating side, approximately0.15 in (3.9 mm) from the tool centerline just below the shoulder.

Uniaxial thermal mechanical simulations were performed using a Gleeble 3500 system under strain (L-Gauge) control. The cylindrical test specimens measured approximately 0.254 in (6.45 mm) and 0.246 in (6.26 mm) in length and 0.245 in (6.22 mm) and 0.246 in (6.25 mm) in diameter; low and high RPM respectively.   The longitudinal axis of the cylindrical specimens was positioned parallel to the compression axis and centered between two ISO-T anvils. A thin graphite sheet was used between the anvil and the specimen which served as a lubricant to prevent barreling as well as provide sufficient compliance to protect anvils.   The ISO-T anvils were designed to provide uniform heating and deformation during thermomechanical testing.   A jaw-to-jaw L-strain gauge system was positioned across the jaws to provide precise dynamic displacement measurements. Once the test specimen was secured between the anvil/jaw assembly and thermocouple wires were connected, the test chamber was vacuum-sealed and flooded with argon gas. Before and after the test, the specimens were measured and shape coefficients for barreling, ovality, circularity and height coefficients (listed in Appendix C-1) were calculated according to NPL recommendations [64] to ensure test validity. After testing, the flow stress was calculated from initial specimen length, instantaneous L-gauge measurements and time output data.

After testing, the compressed Gleeble specimens and one untested base metal specimen were sectioned at the center along the plane parallel to the compression axis (or rolling direction for base metal), mounted in epoxy and metallographically prepared to a 1 μm finish. Vickers (Hv) microhardness measurements were taken at incremental spacings of 0.012 in (0.30 mm) along intersecting vertical, horizontal and diagonal lines using a 300 gf load. The

metallographically prepared specimens were etched with Luca's reagent to reveal grain size and other microconstituents. Grain size was measured using Abrams 3 circle method according to ASTM E112.

4.5   Results

4.5.1   Model Simulations

4.5.1.1 Predicted Temperatures

Three-dimensional isotherm surface distributions are shown in Figure 4-3.   The temperature entering the control volume at 300K has little change until it reaches the outermost edge of the rotating tool. The predicted peak temperature at all nine processing conditions occurred at the probe-to-workpiece interface. Peak temperatures typically reported for this process range from 0.8 to 0.95 of the material's melting temperature (T_m) [65]. The peak temperatures predicted in these simulations range from 1237 K ($0.73T_m$) to 1783 K ($1.05Tm$) (see Figure 4-4). The peak temperatures at the low rotational speed were cold ($0.73 - 0.75T_m$) relative to those typically reported and those at the high rotational speed were too hot ($1.04 - 1.05\ T_m$). The peak temperatures predicted at the intermediate rotational speed were on the upper shelf of expected temperatures for this process (0.95 to $0.96T_m$).

A plot illustrating how predicted peak temperature varies as a function of travel and rotational speed is shown in Figure 4-5. The plot shows that predicted peak temperature is most sensitive to changes in rotational speed and practically insensitive to changes in travel speed. Peak temperature is seen to increase with increasing rotational speed.

4.5.1.2 Advancing and Retreating Side HAZ Temperature Profiles

Thermal histories on the advancing and retreating side were extracted from a set of complimentary streamlines. These streamlines were equi-distance from the probe centerline at mid-thickness of the control volume. This position within the control volume represents also the thermocouple positions placed at 0.157 inch (3.988 mm) on either side of the centerline within experimental processed plates.
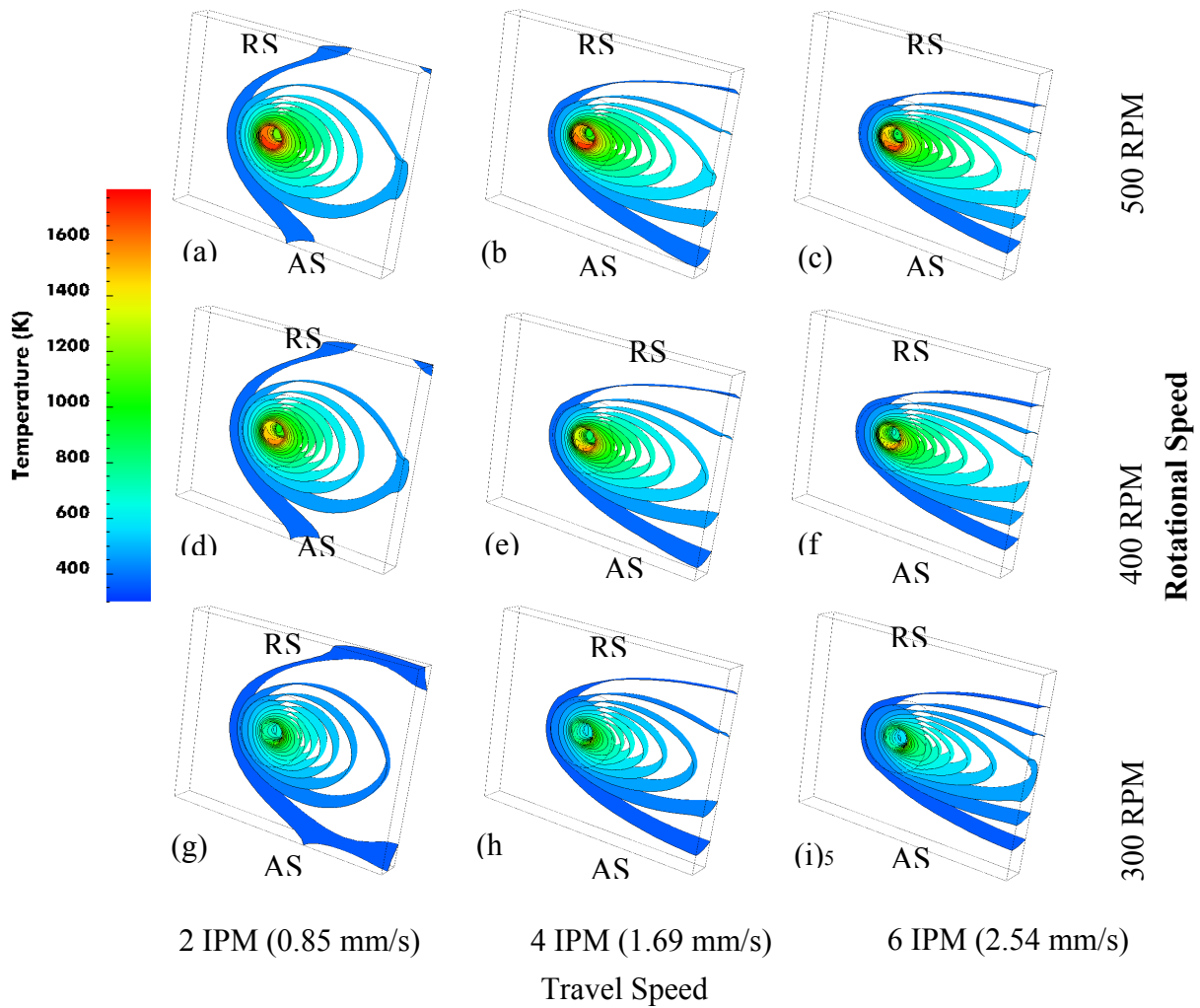
Figure 4-3 Matrix of iso-therm surface distribution for all nine processing conditions. The retreating side is located at the top and bottom is the advancing side.

	2	4	6
500	**1783.02** 1.05Tm	**1781.39** 1.05Tm	**1755.85** 1.04Tm
400	**1627.97** 0.96Tm	**1631.01** 0.96 Tm	**1607.24** 0.95Tm
300	**1237.43** 0.73Tm	**1267.2** 0.75Tm	**1237.6** 0.73Tm

RPM

Travel Speed (IPM)
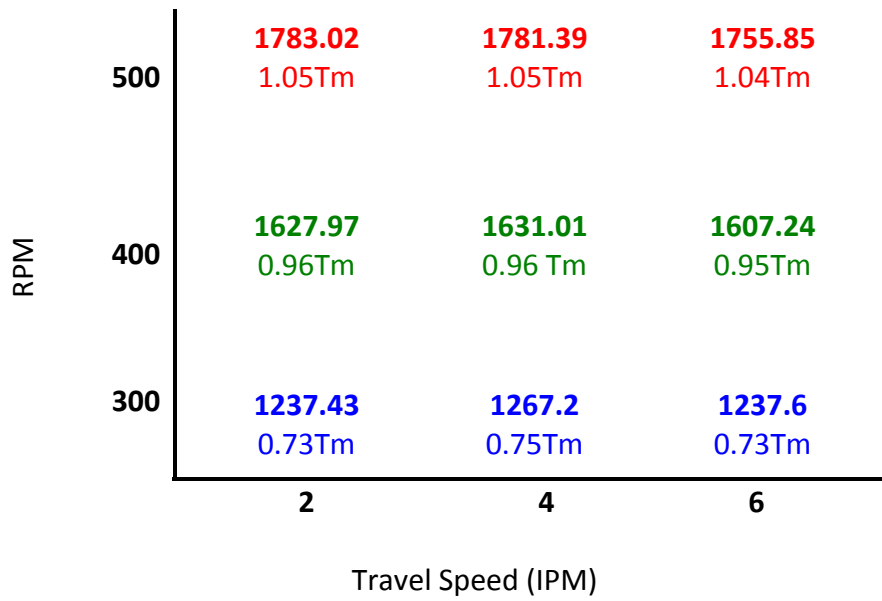
Figure 4-4 Peak and homologous temperature at all nine processing conditions.
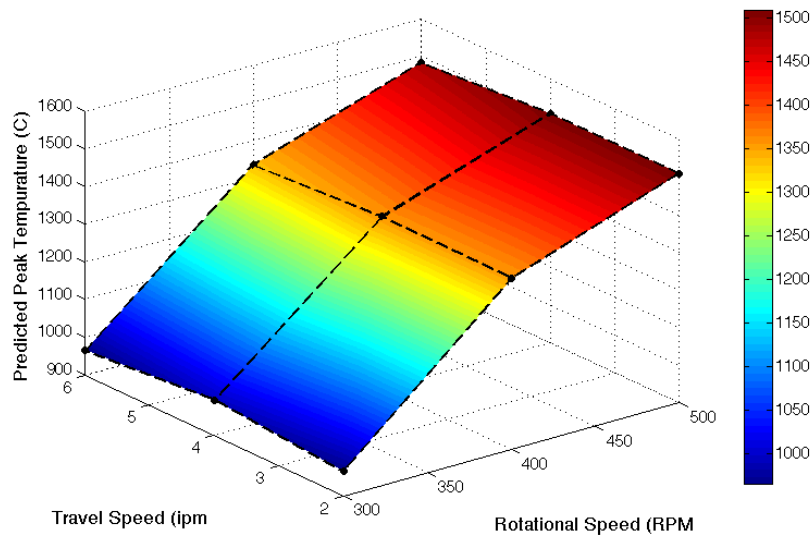
Figure 4-5 Plot of peak temperature as a function or travel and rotational speed as a function of travel and rotational speed.

The predicted advancing and retreating side HAZ temperature profiles are shown in

Figure 4-6. Observations of the plots indicate the heating and cooling rates are identical and that

the advancing side peak HAZ temperature equal to or higher than the retreating side peak
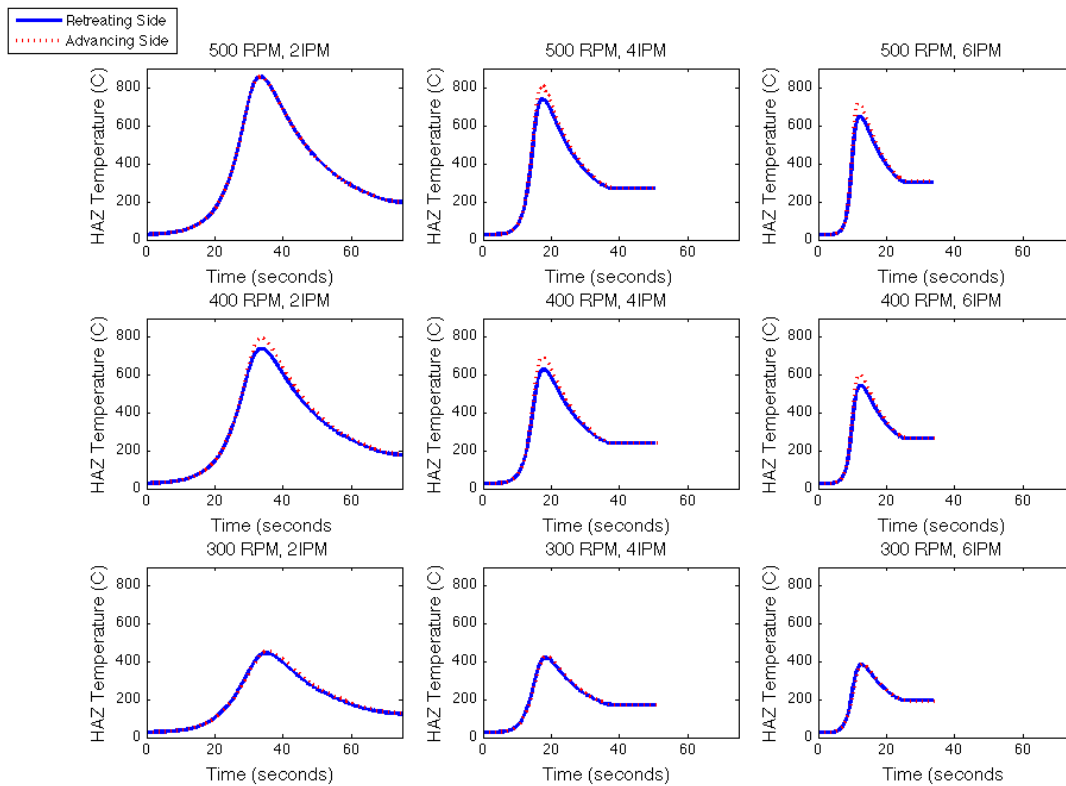
temperature.

Figure 4-6 Matrix of plots showing advancing and retreating side temperature profiles in HAZ region approximately 0.157 inch (3.988 mm) from the centerline.

The difference between the advancing and retreating side peak HAZ temperatures as a

function of travel and rotational speed is plotted in Figure 4-7. At the low rotational speed, the

difference between the advancing and retreating sides is minimal to nonexistent. With the

exception of behavior at 500 RPM, 2 IPM, where no difference exists, the difference in peak

HAZ temperature increases with increasing rotational speed. For the intermediate and high

rotational speeds, the peak HAZ temperature increases with increasing travel speed. The

advancing side HAZ peak temperature is higher than the retreating side by 0 to 10°C at the low,

40 to 60°C at the intermediate, and 0 to 80°C at the high rotational speeds.
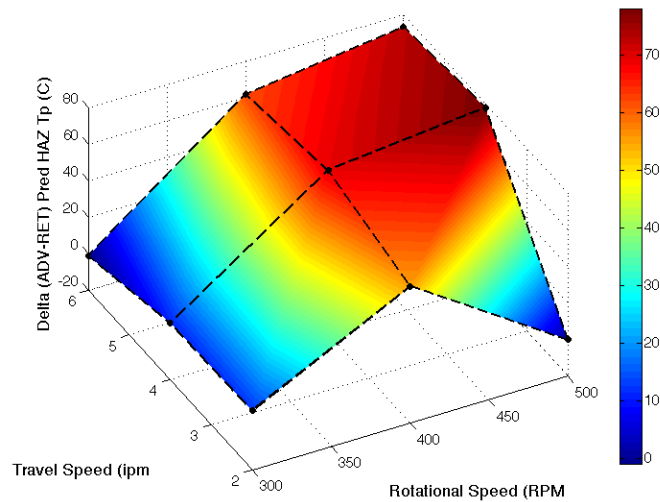
**Figure 4-7 Plot showing the difference between advancing and retreating side peak
temperatures as a function of travel and rotational speed.**

A qualitative comparison between the predicted advancing side and measured HAZ

temperature profiles can be assessed from Figure 4-8. Observations of Figure 4-8 suggests that

the model does an adequate job of predicting the measured data's trend of decreasing peak

temperature with increasing travel speed at the intermediate and high rotational speed but not at

110

the low rotational speed. The predicted data show greater sensitivity to changes in rotational

speed at a given travel speed while the measured data show little to no sensitivity.
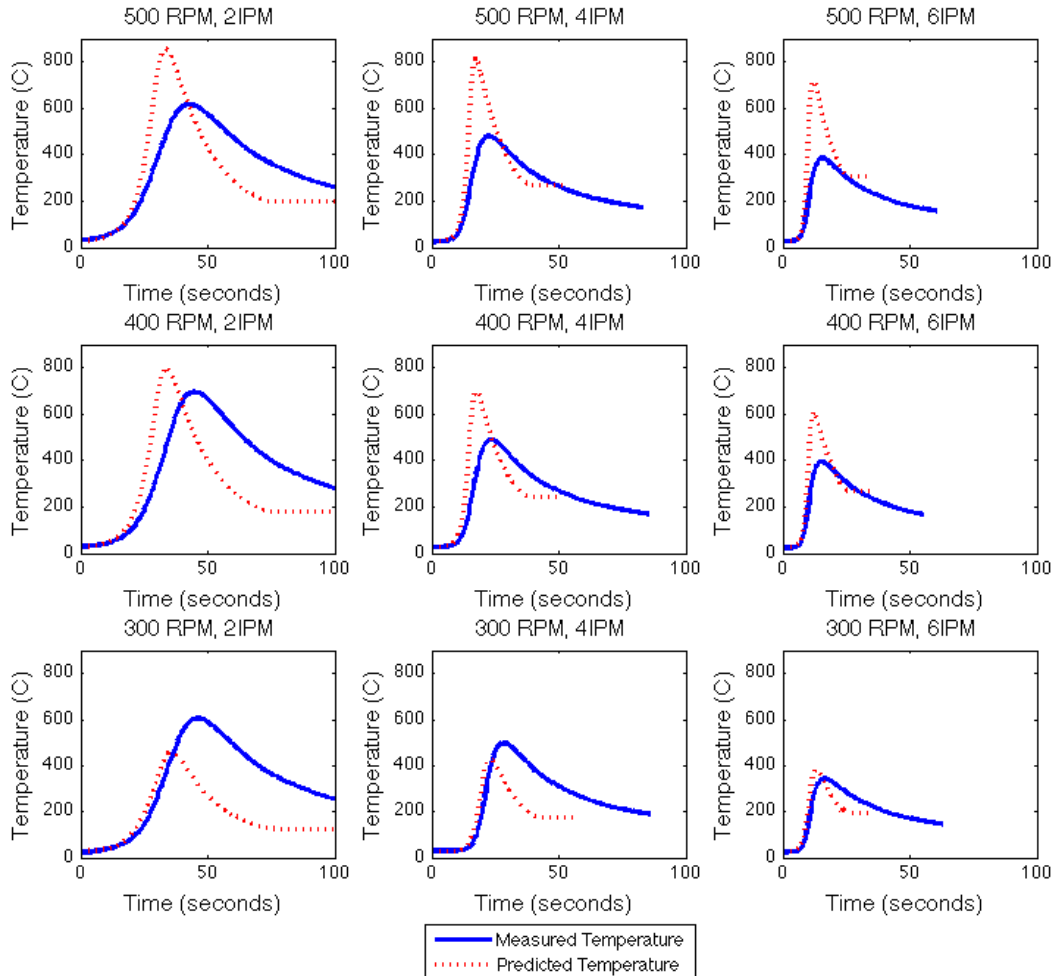
Figure 4-8 Matrix of plots showing the predicted and measured advancing side HAZ temperature profiles at a distance 0.157 in (3.988 mm) away from processing path centerline

111

The measured/predicted ratio of the HAZ temperature profiles is shown in Figure 4-9.

Figure 4-9 shows the ratio of the predicted to measured temperature profiles is most sensitive to

changes in travel speed.
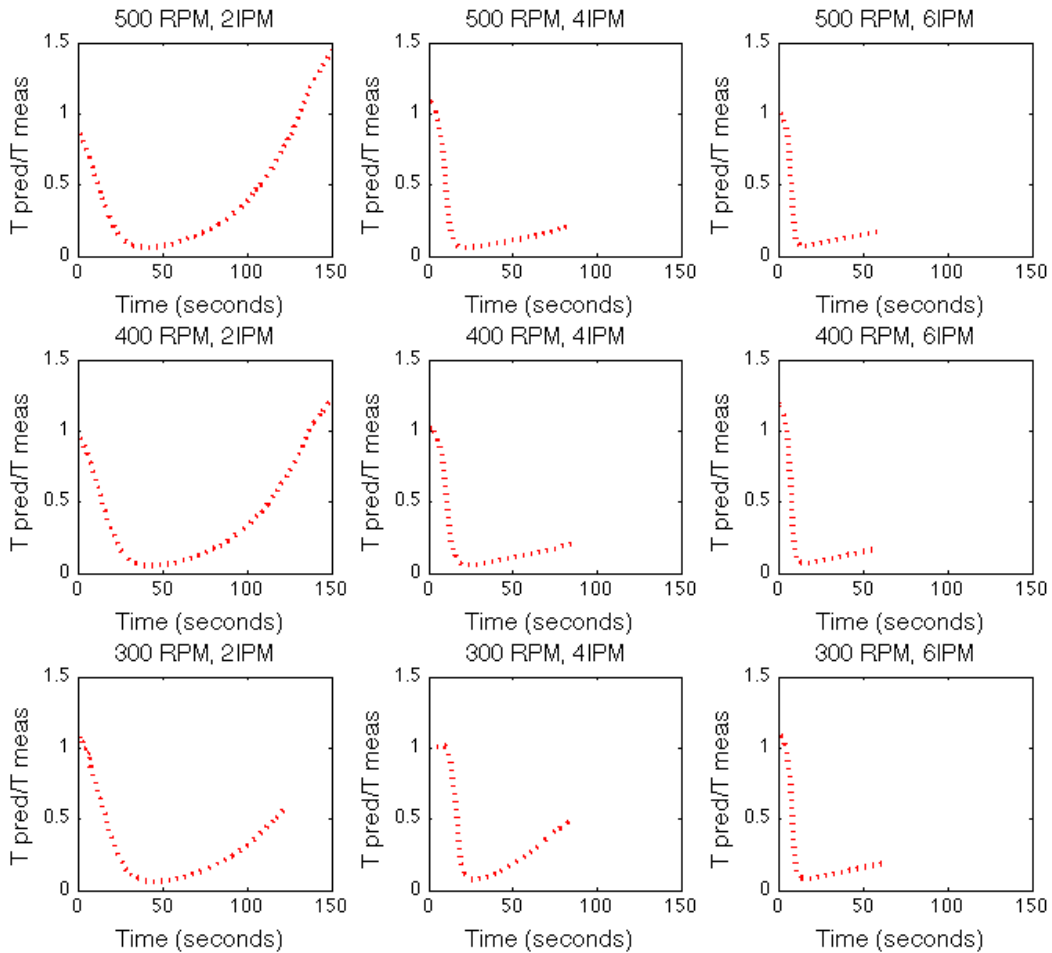
Figure 4-9   Matrix of plots showing the ratio of measured to predicted temperature profiles as a function of time.

The predicted to measured cooling rate ratio as a function of travel and rotational speed, shown in Figure 4-10, shows that the highest ratio is seen at the highest rotational speed and the minimum is seen at the intermediate rotational speed. At the low and high rotational speeds, the ratio increases with increasing travel speed. These observations indicate that the model's predictability of cooling rate is best at the intermediate rotational speed and worsens at low and high rotational speeds and with increasing travel speed.
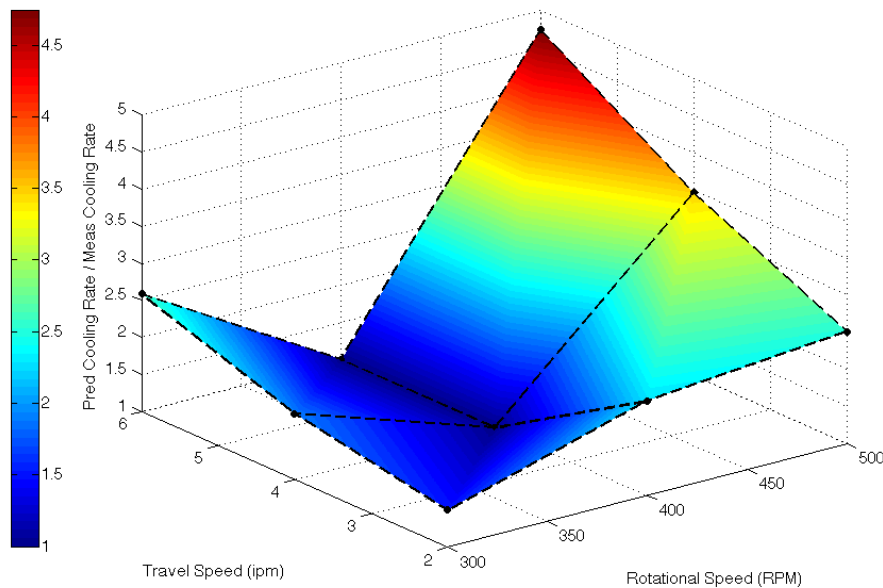
Figure 4-10 Plot of ratio of predicted to measured cooling rates as a function of travel and rotational speed.

Figure 4-11 shows how the predicted to measured peak HAZ temperature ratio varies over travel or rotational speed. For HAZ peak temperature, the ratio increases with increasing

travel speed and increasing rotational speed. The lowest ratio occurs at the lowest rotational and

travel speed and highest occurs at the highest rotational travel speed.
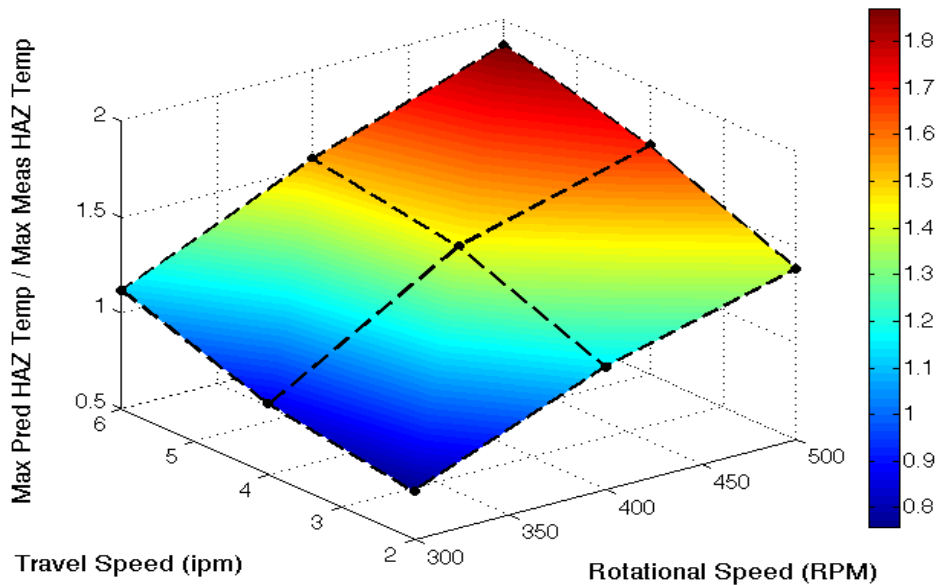
Figure 4-11 Predicted HAZ peak temperature as a function of travel and rotational speed.

4.5.1.3 Power

Figure 4-12 shows how predicted power from probe and shoulder surface varies as a

function of travel and rotational speed. Figure 4-13 shows the same for measured power output.

Predicted power and measured power both increase with increasing rotational speed, indicating

good predictive capability with respect to changes in rotational speed. Predicted power shows

little sensitivity to changes in travel speed while measured power does show sensitivity;

decreases with decreasing travel speed suggesting poor correlation between predicted and

measured data with respect to travel speed. To quantify these differences, the ratio of measured power to predicted power as a function of travel and rotational speed are shown in Figure 4-14. The figure shows that measured power is approximately 3 to 6.7 times higher than predicted values. The highest difference occurs at the low rotational speed indicating that while the model provides qualitative agreement with respect to changes in rotational speed, the error to quantitatively predict power worsens with increasing rotational speed, particularly at the low rotational speed.
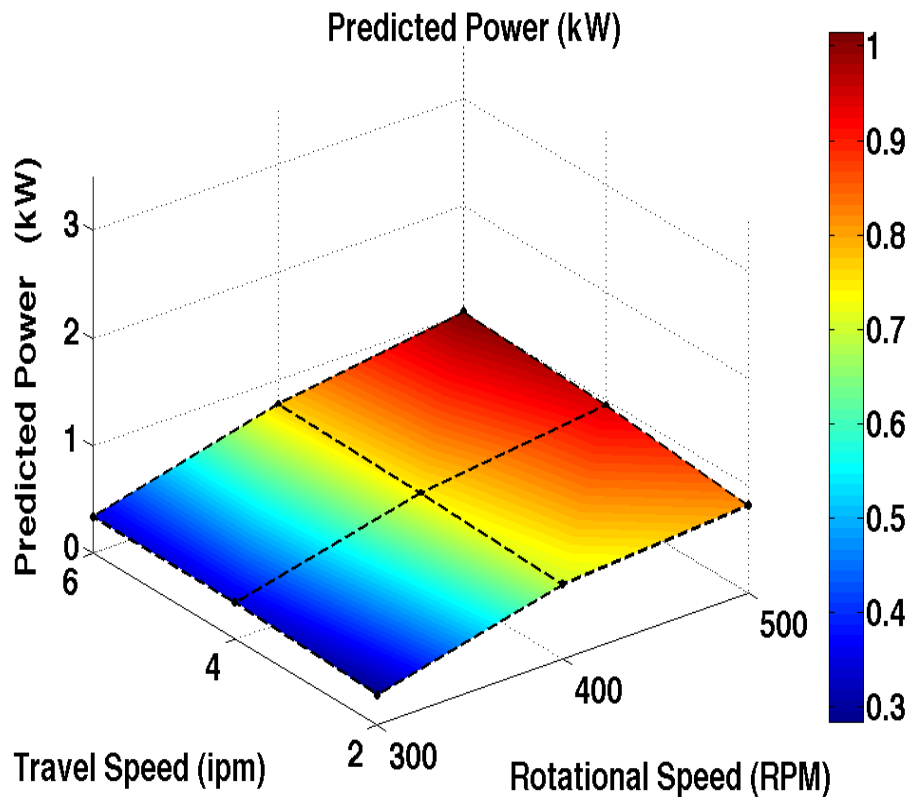
Figure 4-12 Plot of predicted power as a function of travel and rotational speeds.
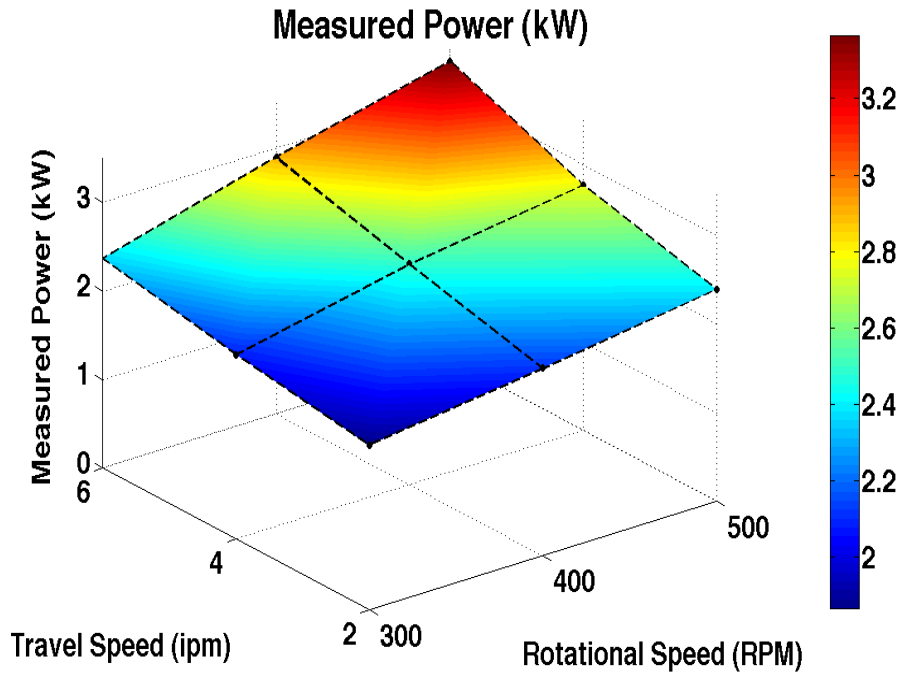
Figure 4-13 Plot of measured power as a function of travel and rotational speeds.
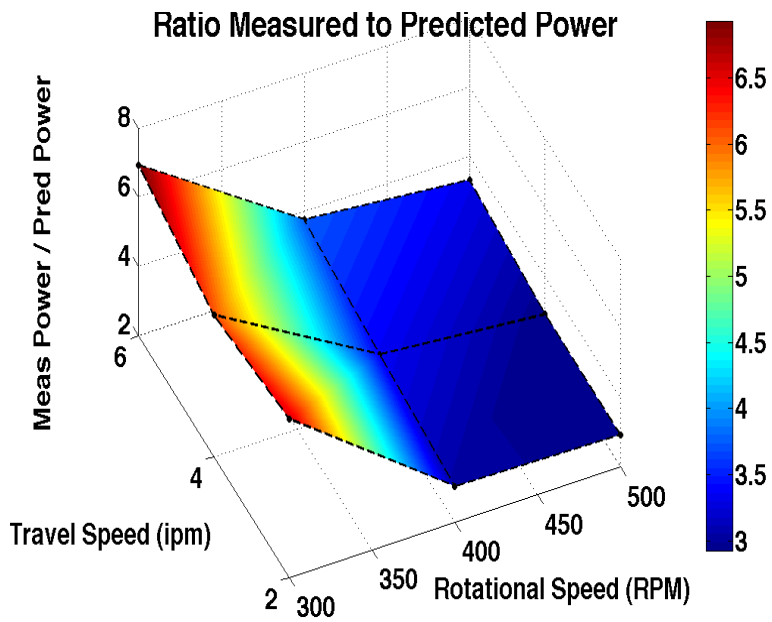
Figure 4-14 Plot of the ratio of measured/predicted power as a function of travel and rotational speed.

A measure of goodness of fit can be quantified by normalizing both predicted and measured power by their respective maximum power value and plotting them against each other as shown in Figure 4-15. The plot shows an R^2 value of 0.6346 indicating a good correlation, albeit not perfect, between predicted and measured power over the entire range of processing parameters. Examining the goodness of fit within each set of rotational speeds (see Figure 4-16), the correlation between predicted and measured power increases substantially for the intermediate ($R^2 = 0.9924$) and high ($R^2 = 0.9378$) rotational speeds and faired less favorable at the low rotational speed ($R^2 = 0.5080$).
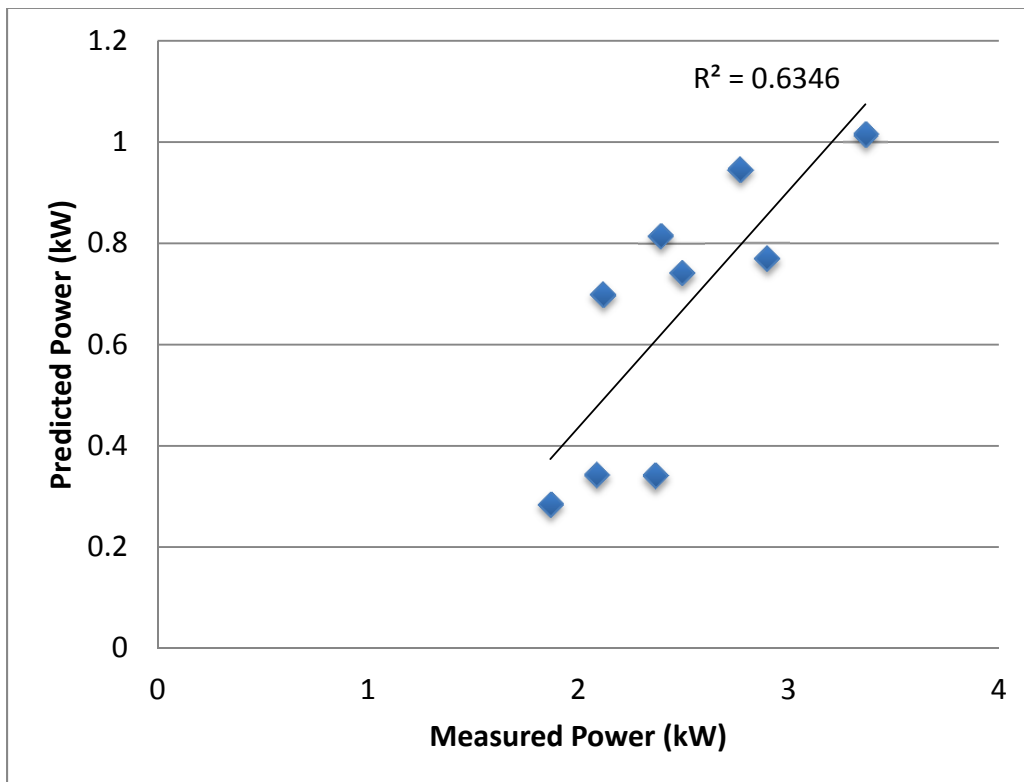
Figure 4-15 Predicted power versus measured power
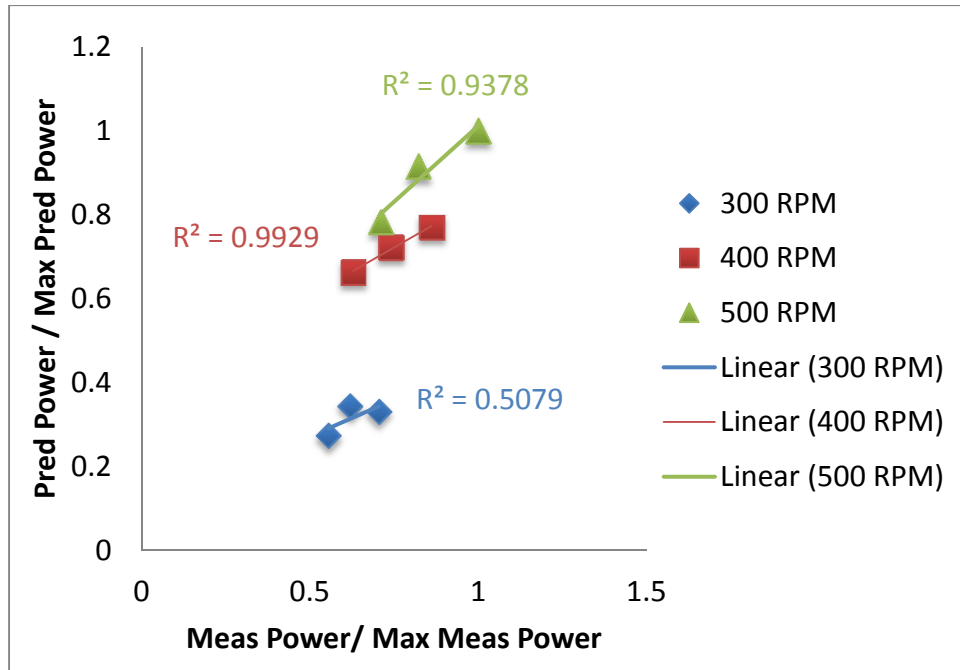
Figure 4-16   Predicted power versus normalized measured power evaluated within rotational speed sets.

4.5.1.4 X-Force

Predicted X-force for probe and shoulder surfaces are plotted Figure 4-17 as a function of travel and rotational speed. The plot shows a gradual increase in predicted X-force with decreasing rotational speed and increasing travel speed. Again, the largest increase is observed at the low rotational speed; approximately 40% higher than that at the intermediate and up to 50% higher than that at the high rotational speed. The measured X-force as a function of travel and rotational speed is shown in Figure 4-18. This plot shows an increase in measured X-force with increasing travel speed but unlike the predicted X-force data, the measured X-force does not show a linear relationship with respect to rotational speed.
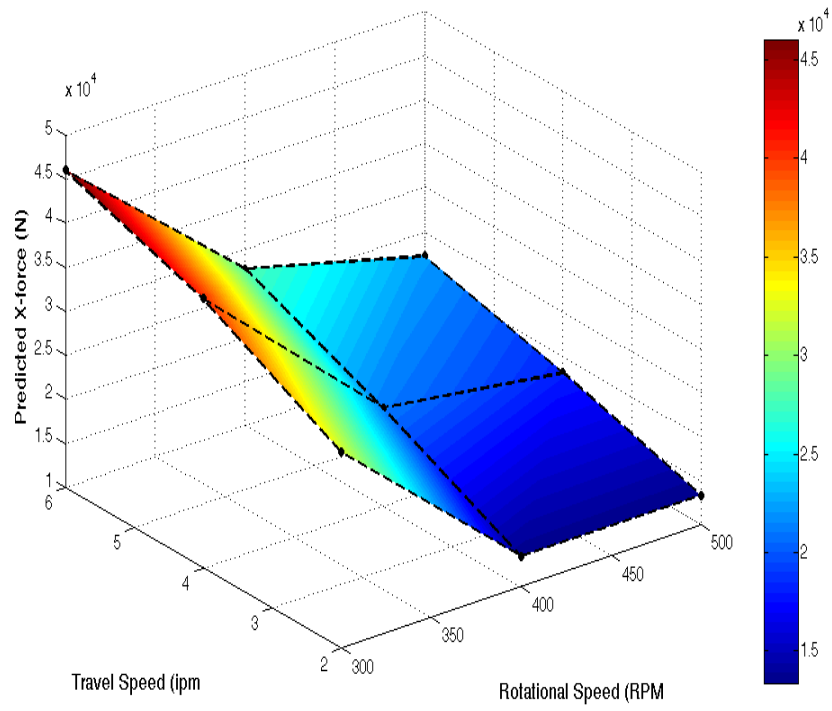
Figure 4-17 Plot of predicted X-force as a function of travel and rotational speed.
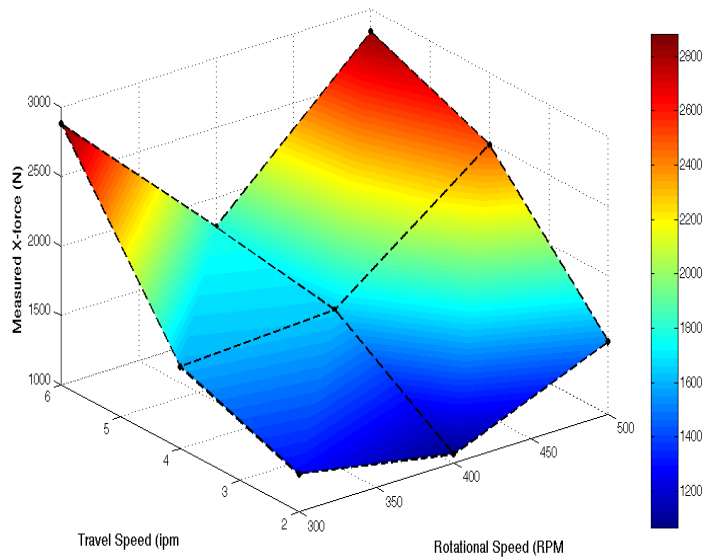
Figure 4-18 Plot of measured X-force as a function of travel and rotational speeds.

For the measured X-force data set, the magnitude of X-forces are highest at the low and high rotational speeds relative to those at the intermediate rotational speed; approximately 40% to 55% higher. To quantify differences, the ratio of predicted: measured X-force as a function of travel and rotational speed are plotted in Figure 4-19. Figure 4-19 shows an increase in the ratio with increasing rotational speed. Predicted X-force is 7 - 9 times higher at the high, 12 to 15 times higher at the intermediate and 16 to 25 times higher at the low rotational speeds. This indicates that the error quantitatively increases as rotational speed decreases. Similar to trend observed with power ratio, the greatest discrepancy occurs at the low rotational speed.
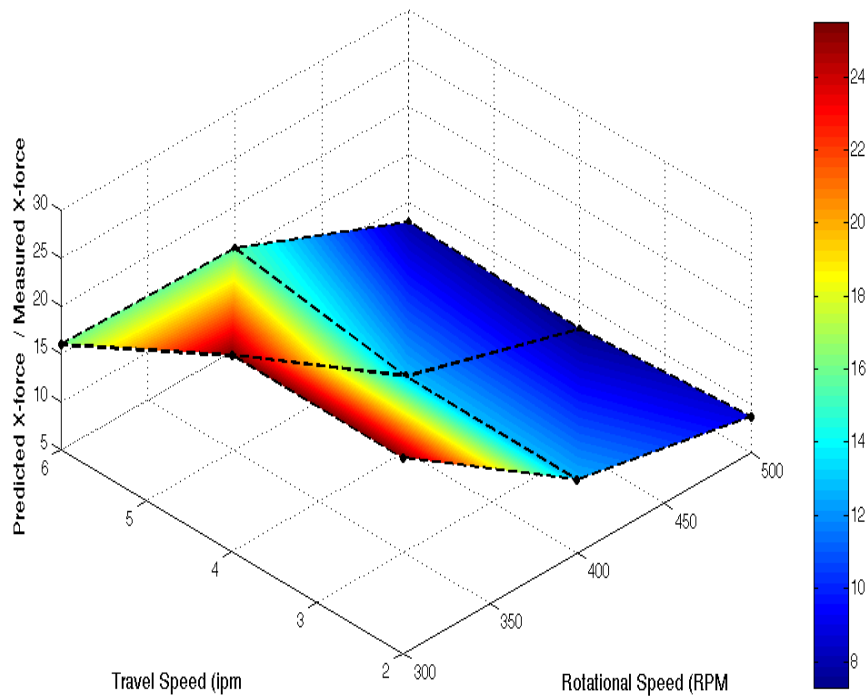
Figure 4-19 Plot of the ratio of predicted to measured X-force as a function of travel and rotational speeds.

A measure of goodness of fit can be quantified by normalizing both predicted and measured X-force by their respective maximum X-force value and plotting them against each other as shown in Figure 4-20. The plot shows a poor goodness of fit measure ($R^2 = 0.1985$) over the entire range of processing parameters. However, examining the goodness of fit correlation within each set of rotational speeds (see Figure 4-21), the correlation between predicted and measured X-force increases substantially for the intermediate ($R^2 = 0.9117$), high ($R^2 = 0.9525$) rotational speeds and low rotational speed ($R^2 = 0.8081$). Similar to evaluation with power, the highest correlation exists at the intermediate rotational speed and the lowest correlation exists at the low rotational speed.
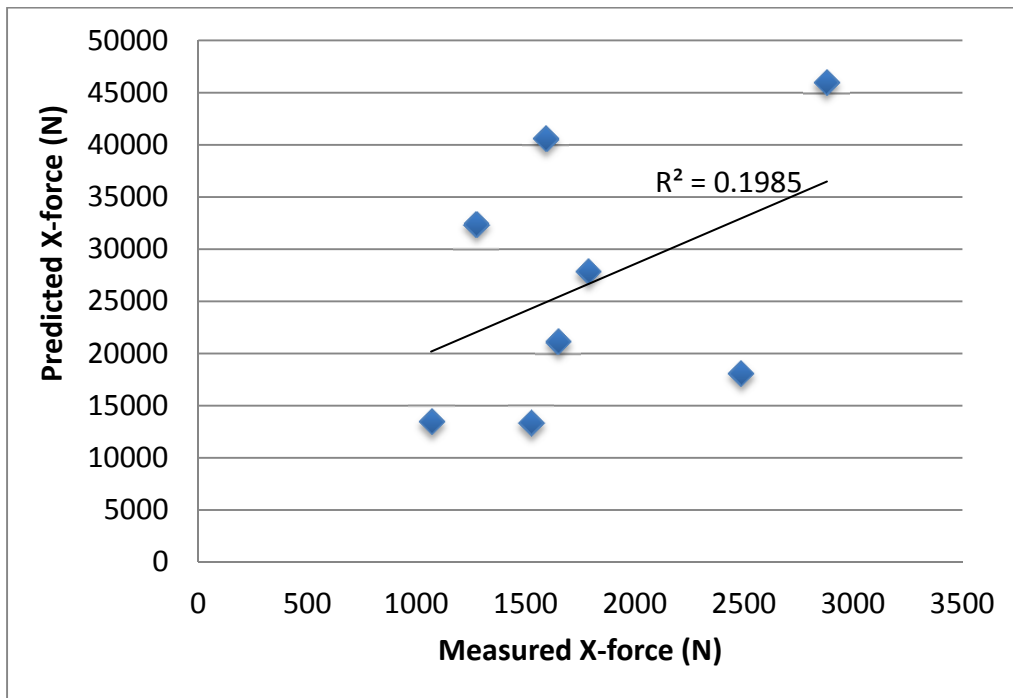
Figure 4-20 Normalized predicted X-force data plotted against normalized measured X-force data.
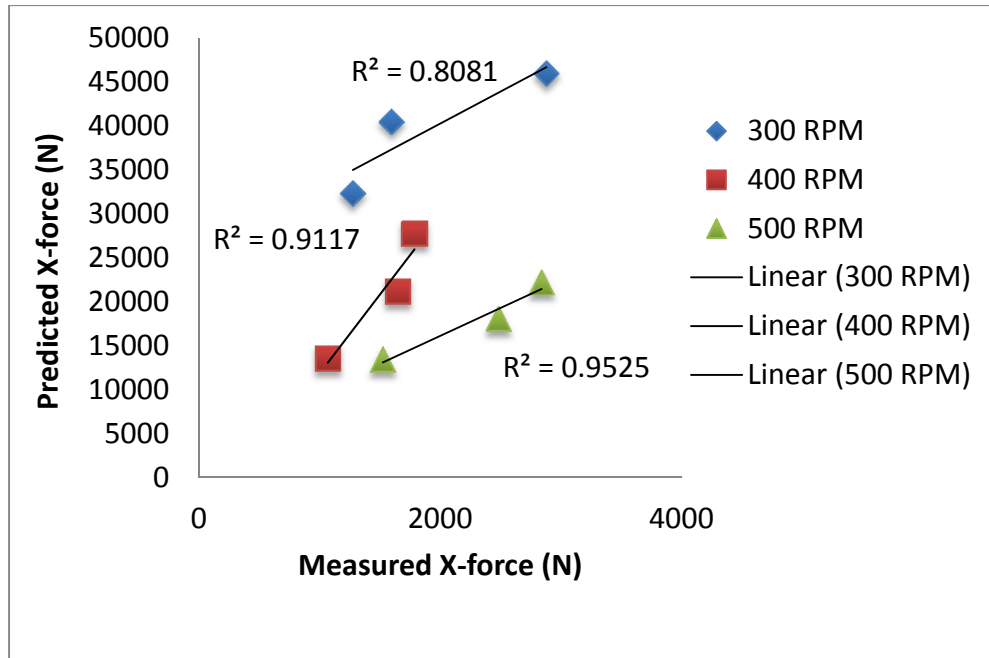
Figure 4-21 Predicted X-force plotted versus measured X-force data.

4.5.2   State Variable Distributions

The 2-dimensional state variable distribution at the exit surface is shown in Figure 4-22. Note that the advancing side is to the left and retreating side is to the right of each figure. An outline of the probe and shoulder is superimposed in all figures for reference. Observations of Figure 4-22 suggest that the state variable distribution is symmetric with respect to the axial centerline of the probe and that a sharper transition between base metal and stir zone exists on the advancing side compared to that on the retreating side.

To quantify trends, the mean of the exit state variable, normalized by the initial state value, is plotted as a function of travel and rotational speed as shown in Figure 4-23. The plot shows the highest average exit state variable value at the lowest rotational speed and decreases with increasing rotational speed and decreasing travel speed.
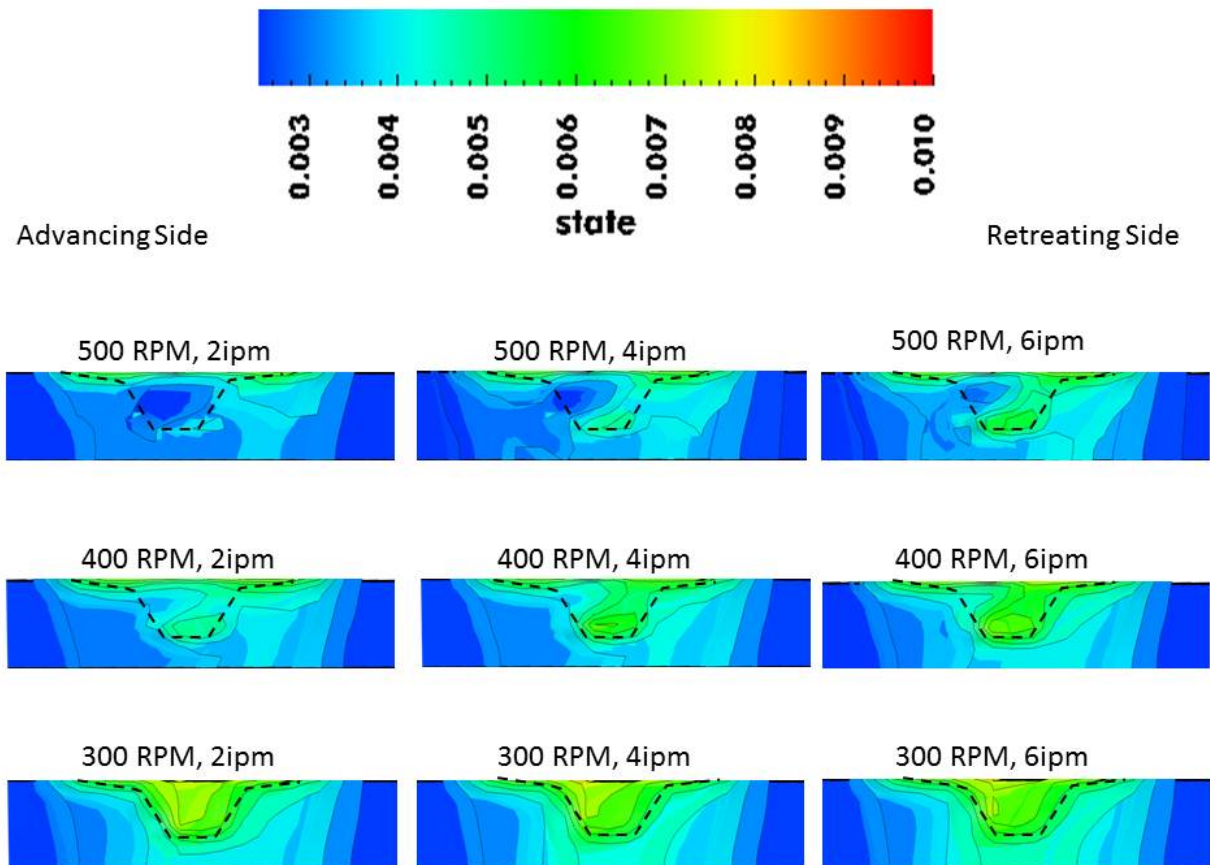
Figure 4-22 Two-dimensional cross-section of state variable distributions for all nine processing conditions.

To quantify the difference between predicted state and measured hardness values, both representative of the material's strength, the normalized values of each were plotted as a function travel and rotational speeds. The state variable was normalized by the initial state variable value and the measured hardness was normalized by its base metal hardness. The plot of the predicted/measured strength ratio as a function of travel and rotational speed is shown in Figure 4-24. The plot shows that the predicted strength is qualitatively 76 to 81% greater than the measured hardness at the highest rotational speed and between 65 to 70 % higher at the low

rotational speed. This indicates that the error increases with increasing rotational speed and no

clear trend is observed with change in travel speed.
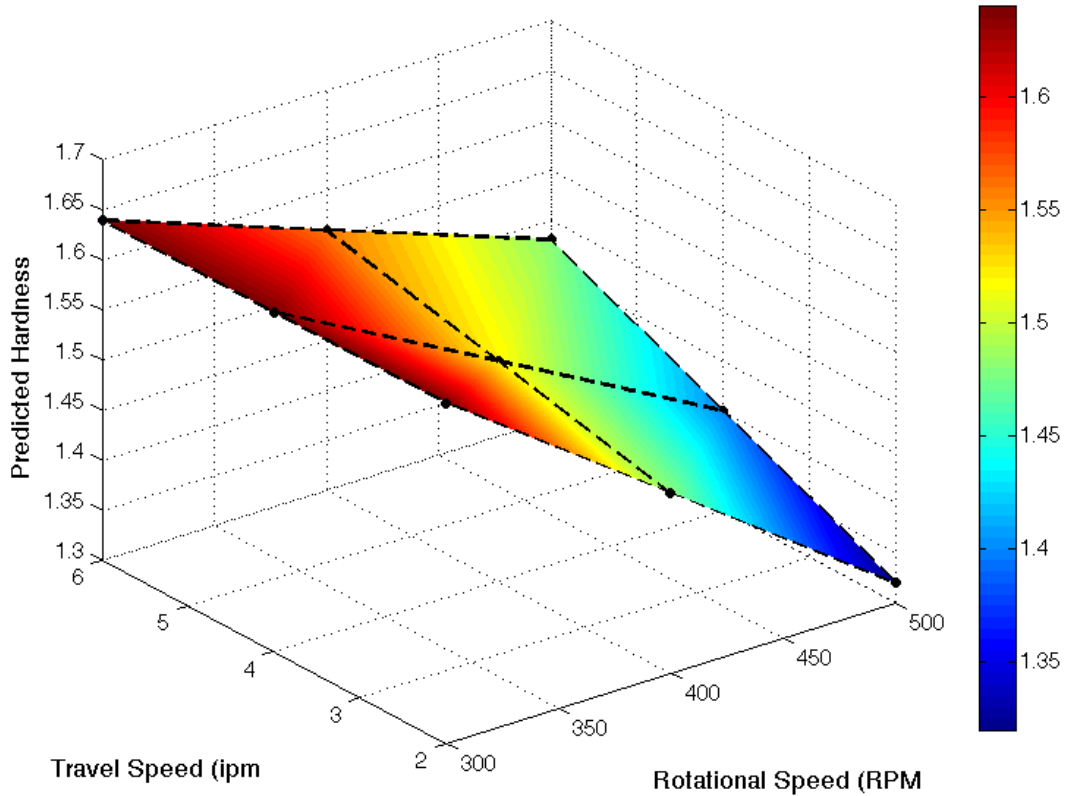
Figure 4-23 Predicated state normalized by the initial state variable as a function of travel and rotational speed.

4.5.3   Physical Simulations

Physical simulations were conducted to assess the accuracy of constitutive relations in

predicting flow stress and to provide a physical representation of grain size and hardness for a

specific thermomechanical history which can then be compared against experimental data. The results from this evaluation are presented in the following paragraphs.
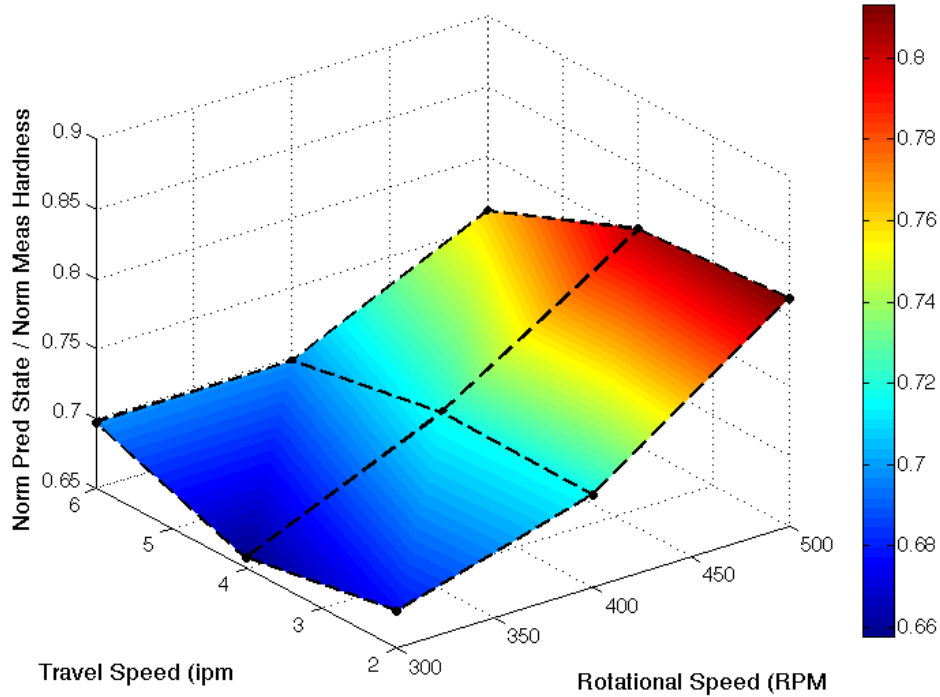
Figure 4-24 Plot of the ratio of the normalized predicted state to normalized measured hardness as a function of travel and rotational speed

4.5.3.1 Thermomechanical Histories

Strain and strain rate histories of selected streamlines shown in Figure 4-25 and Figure 4-26, respectively. These streamlines were extracted from a low (300 RPM, 2 IPM) and high (500 RPM, 2 IPM) rotational speed condition at a distance of 0.155 in (3.937 mm) away from the probe centerline on the retreating side. While the strain and strain rate histories are almost

125

identical for these two streamlines, they exhibit large difference in peak temperature and cooling rates as shown in Figure 4-27. The peak temperature of the lower rotational speed condition peaks at 482.6ºC while the higher rotational speed condition peaks at 947.9ºC; approximately two times greater at the higher rotational speed. The cooling rate from the higher rotational speed curve is also twice the cooling rate relative to the lower rotational speed curve (50ºC/s vs. 25ºC/s). These differences in peak temperature should result in differences in microstructure, grain size and properties since these variables are controlled in large part by peak temperature, amount of plastic deformation and cooling rate for a given chemical composition.
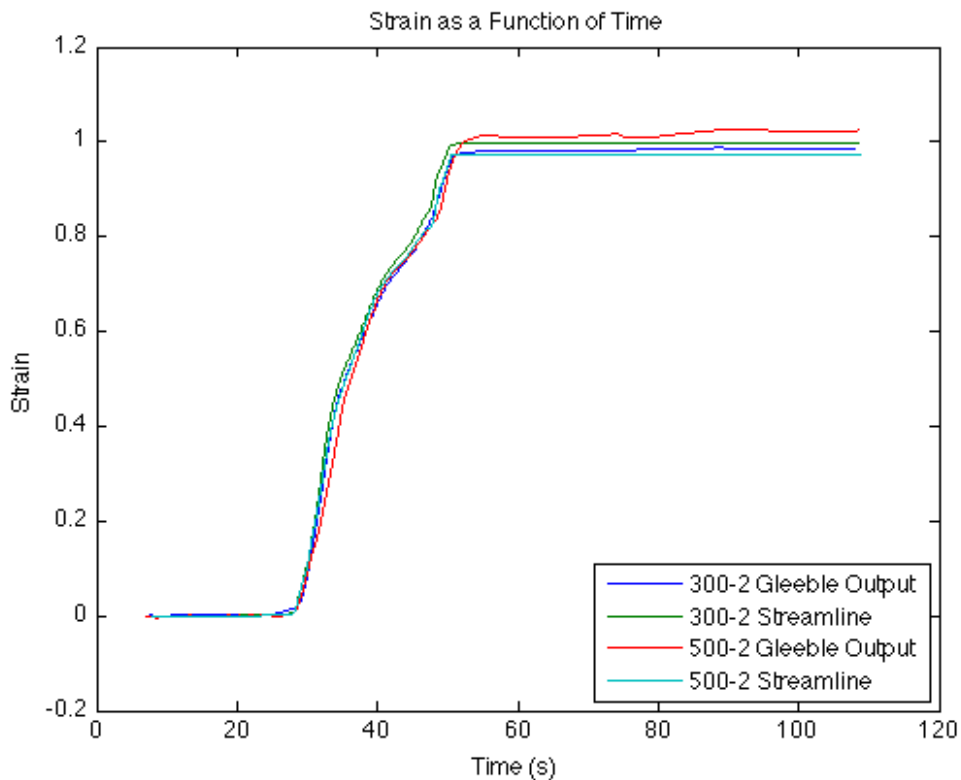
Figure 4-25 Gleeble and streamline strain histories as a function of time.

126
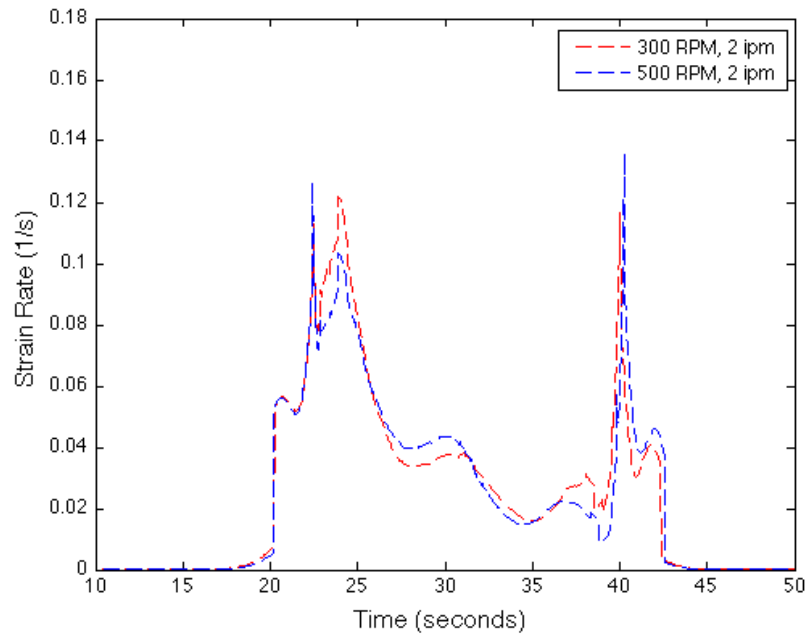
Figure 4-26 Streamline strain rate histories as a function of time
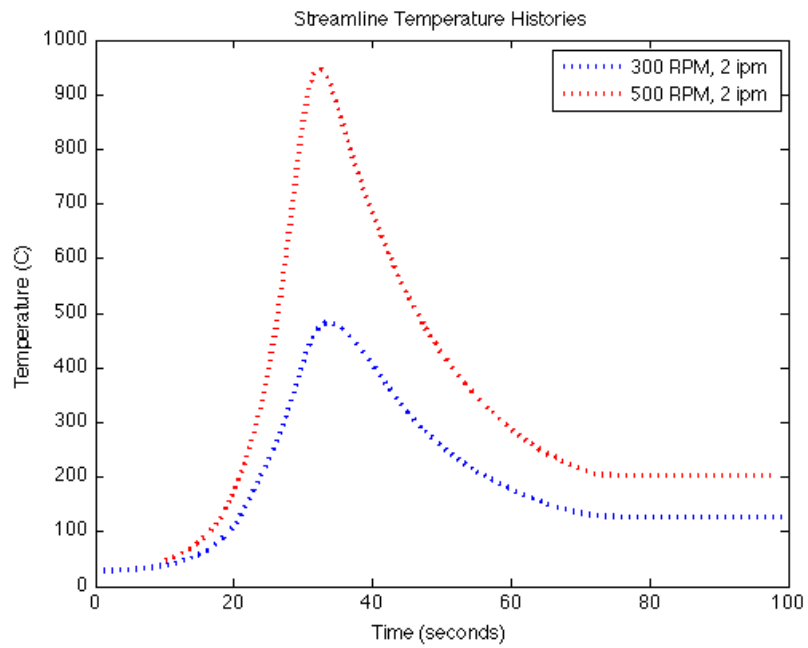
Figure 4-27 Streamline temperature histories as a function of time.

4.5.3.2 Grain Size

Average grain size measurements from the compressed specimens are listed in Table 4-6. The specimen compressed at the lower temperature had a grain size of 22.3 μm while the grain size of that compressed at the higher temperature, high rotational speed measured 31.6 μm. In both cases, the average grain size was smaller than base metal grain size (shown in Figure 4-29 (c) for reference). The reductions in grain size from unaffected base metal is 36% less for the lower peak temperature streamline and 10% for the higher peak temperature streamline.
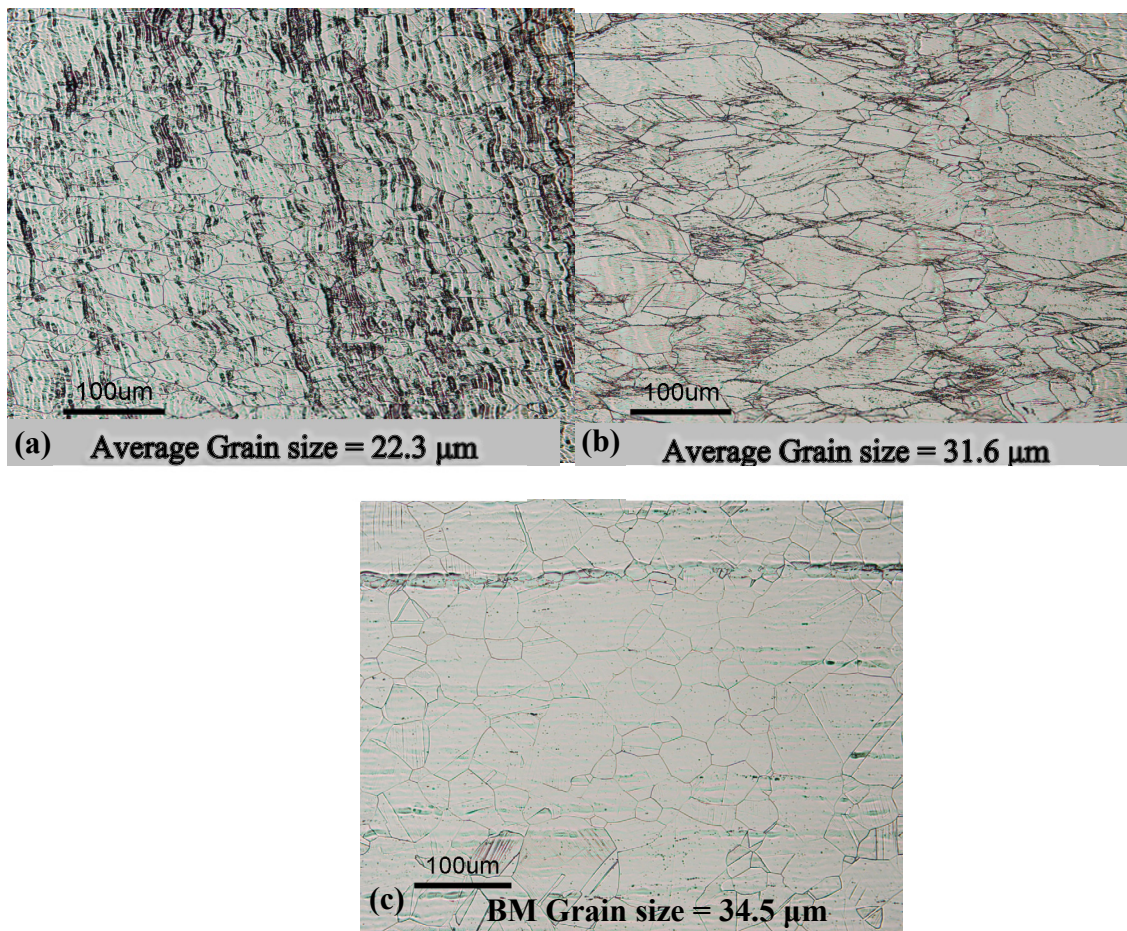
Figure 4-28 Comparison of microstructure of (a) lower temperature compression specimen, (b) higher temperature compression specimen and (c) unaffected base metal.

Table 4-6 ASTM E112 Grain Size Measured using Abrams 3 Circle Procedure

ID#	MAG	Number of Intercepts					AVE	G.S. (μm)	ASTM
		1	2	3	4	5			
P6	400	56	50	59	58	57	56	22.3214	7.676
P7	400	32	40	43	55	28	39.6	31.5657	6.676
BM	400	30	44	37	38	32	36.2	34.5304	6.417

4.5.3.3 Hardness

The average measured Vicker's microhardness resulting from the lower peak temperature compression test is 324 ± 16.38 Hv while the average hardness resulting from the higher peak temperature compression test is 281 ± 13.52 Hv. Figure 4-29 and Figure 4-30 show the measured hardness maps taken for experimentally processed 304L SS at 300 RPM, 2 IPM and 500 RPM, 2 IPM, the simulated conditions. The approximate location of the streamline extracted for physical simulation from is demarked by a circle in each figure for reference. The measured hardness, estimated from Figure 4-29 and Figure 4-30 is approximately 220 Hv at the streamline location. Figure 4-31 is a box plot showing the cross-sectional hardness distribution of Figure 4-29 and Figure 4-30 and the estimated measured value and hardness of Gleeble compression test specimen. Although quantitatively the value is incorrect, the value of Gleeble hardness for the high rotational speed condition is closer to the measured data than the low rotational speed condition.   This indicates the model provides a more accurate prediction of thermomechanical history for the high rotational speed and not very well for the low rotational speed condition.

| □330-350 | □310-330 | ■290-310 | ■270-290 | ■250-270 |
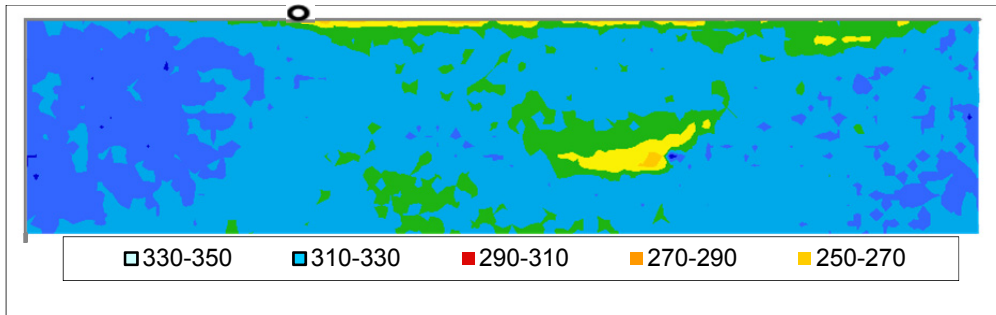
Figure 4-29 Cross-sectional hardness map for specimen processed at 300 RPM, 2 IPM. A circle demarks the location of streamline selected for physical simulation.

| □330-350 | □310-330 | ■290-310 | ■270-290 | ■250-270 |
| ■230-250 | ■210-230 | ■190-210 | ■170-190 | ■150-170 |
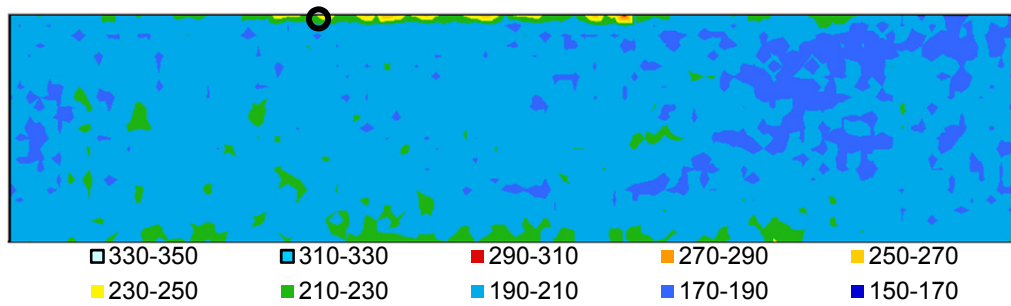
Figure 4-30 Cross-sectional hardness map for specimen processed at 500 RPM, 2 IPM. A circle demarks the location of streamline selected for physical simulation.
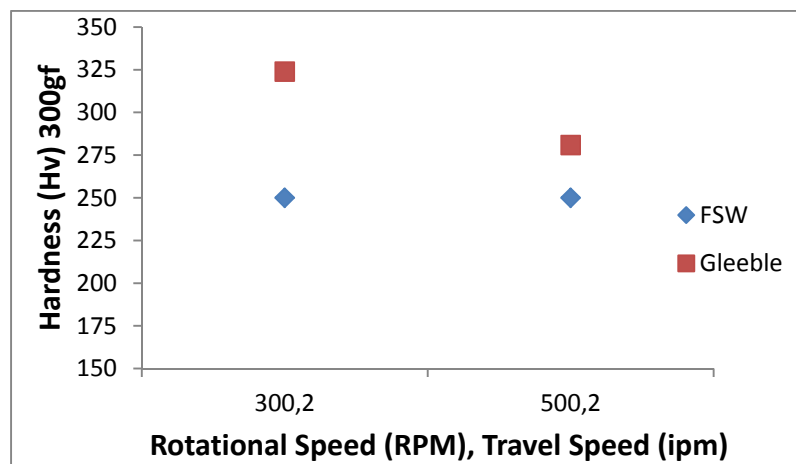
Figure 4-31 Box plot of cross-sectional hardness distributions shown in Figure 4-29 and Figure 4-30.

130

4.5.3.4 Flow Stress Curves

The streamline flow stress curves for the low and high rotational speed conditions were calculated using their respective thermomechanical histories and constitutive Equations 4-1 through 4-10. The streamline flow stress curves are shown in Figure 4-32. Both flow stress curve behave similarly, i.e., strain hardening to peak stress then decreasing to a minimum flow stress followed by an increase in flow stress to a stress level slightly lower than the peak stress level. As would be expected, the streamline from the lower rotational speed, lower temperature condition exhibited a higher flow stress than the higher temperature condition indicating a greater amount of work hardening and deformation for the lower peak temperature, low rotational speed condition.
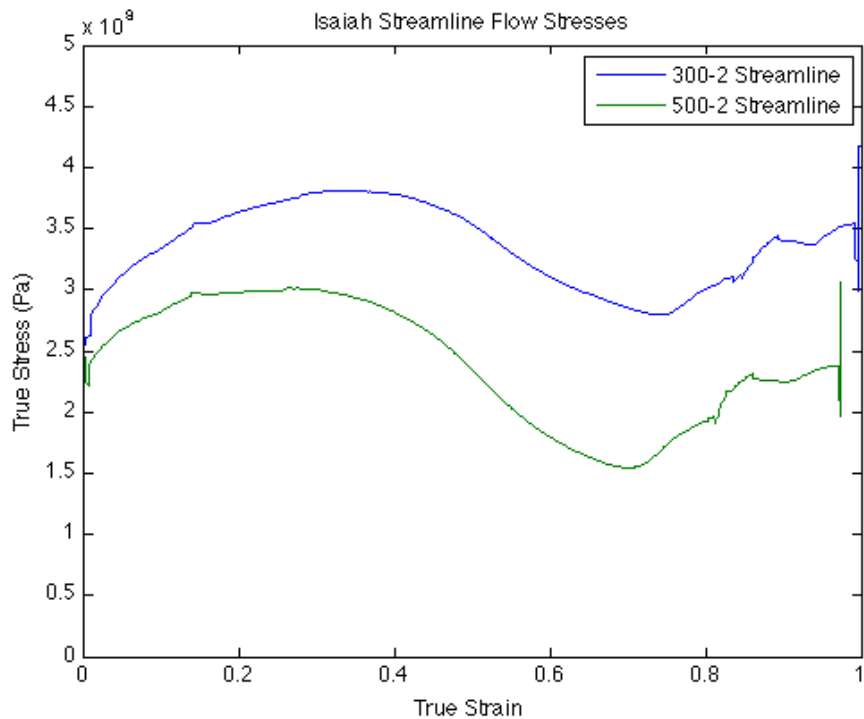
Figure 4-32 Flow stress curves for low and high rotational speed streamlines

The streamline flow stresses are compared against flow stresses calculated from Gleeble thermomechanical histories. The Gleebe flow curves were calculated from the original specimen length, time, and instantaneous L-Gauge measurements. The streamline flow stress of the lower temperature, low rotational speed condition neither shows qualitative nor quantitative agreement (see Figure 4-33) Gleeble flow stress. The streamline flow stress of the higher temperature, high rotational speed condition, shown in Figure 4-34, shows qualitative but not quantitative agreement with Gleeble flow stress. These results indicate the constitutive material model and associated flow stress law does a good job at describing plastic flow behavior over a limited range of processing conditions, i.e., at high rotational speed rather than low rotational speed. These results support previous results that showed poor correlation of predicted power and X-force at the low rotational speed relative to the high and intermediate rotational speeds.
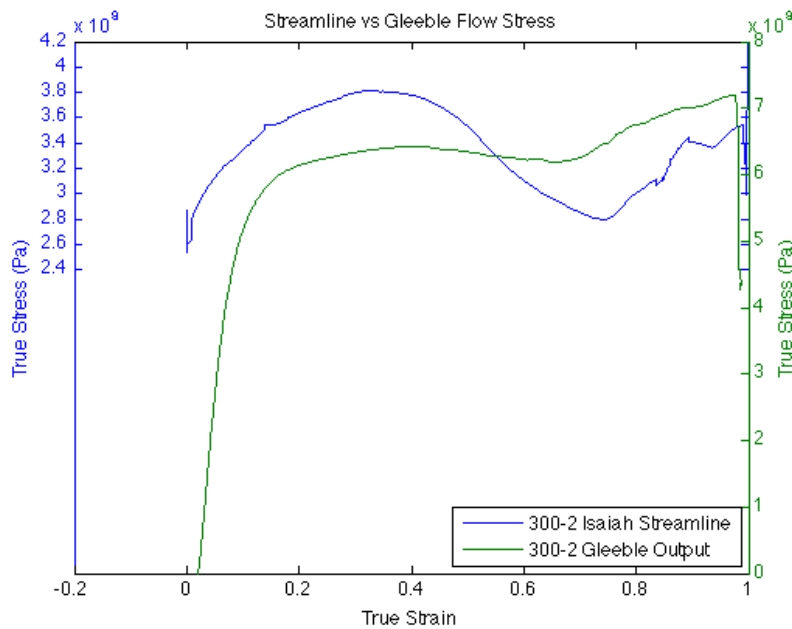
Figure 4-33 Gleeble and streamline flow stress curves for lower temperature, low rotational speed condition.
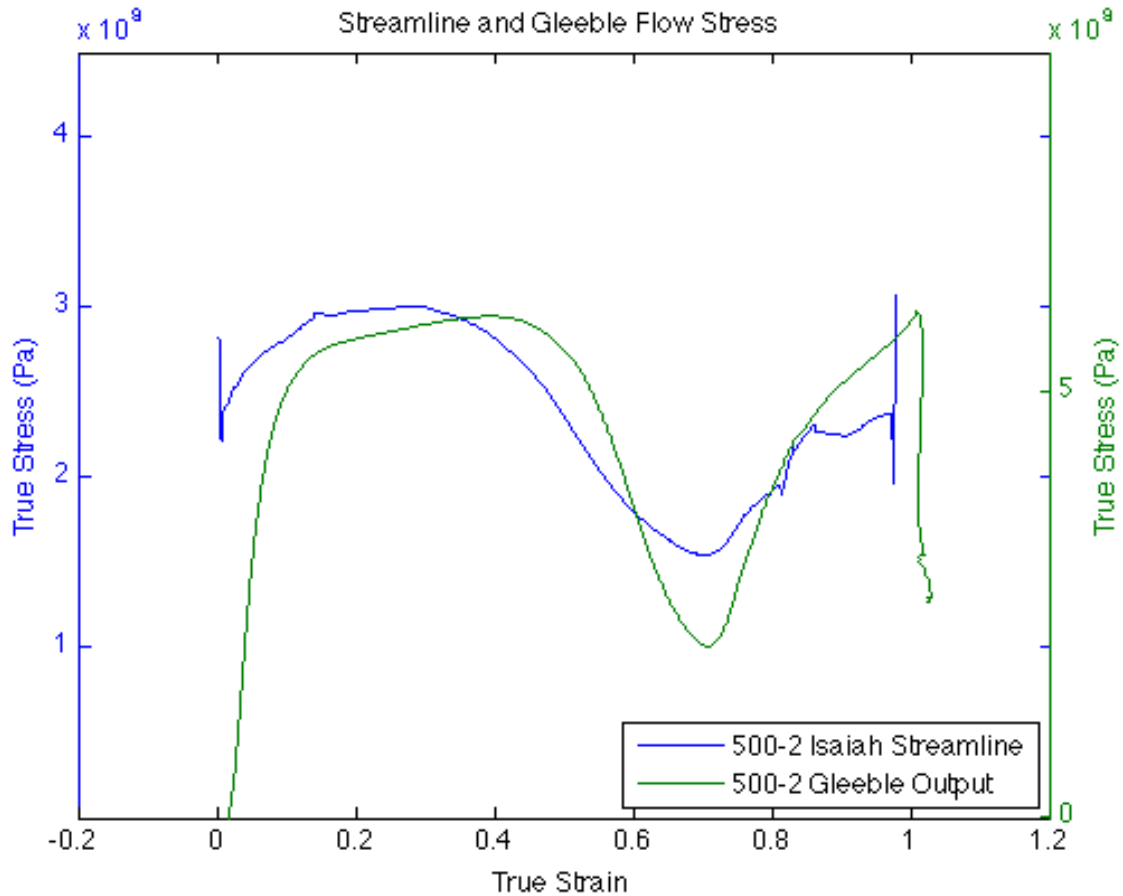
Figure 4-34 Gleeble and streamline flow stress curves for higher temperature, high rotational speed condition.

Comparing the Gleeble flow stress behavior of the lower peak temperature, low rotational speed condition to the higher peak temperature, high rotational speed condition shown in Figure 4-35. The flow stress of the higher peak temperature, high rotational speed condition exhibits a greater amount of thermal softening compared to that at the lower peak temperature, low rotational speed condition.
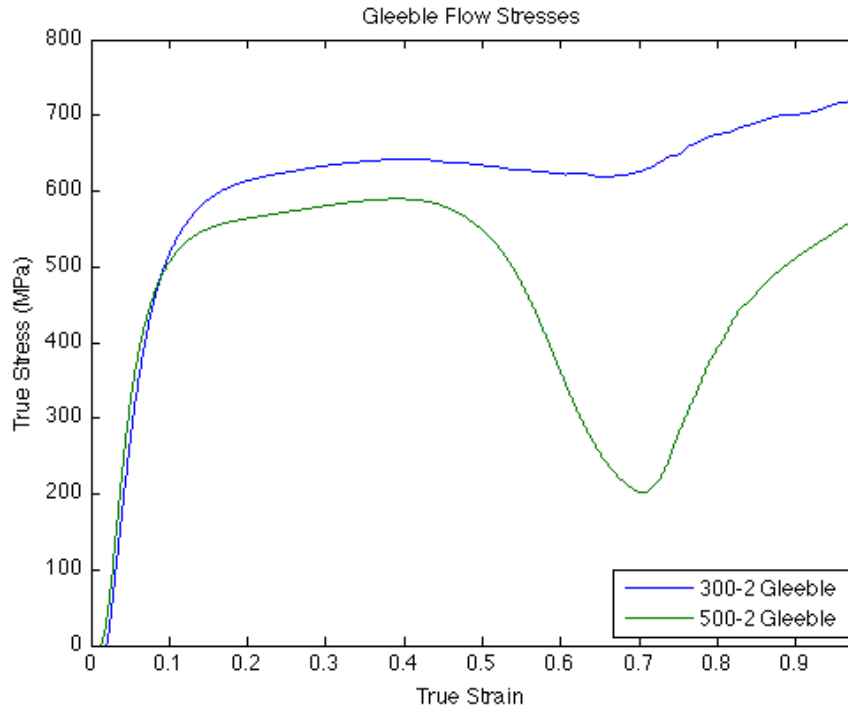
Figure 4-35 Gleeble flow stress curves for low and high rotational speed conditions.

4.5.3.5 Heat Generation due to Deformation

The thermal and mechanical histories show deformation at low temperatures. A simple calculation, as shown in Equation 4-13, was performed to quantify the temperature rise due to deformation.

$$\frac{dT}{dt} = \frac{\sigma * \dot{\varepsilon}}{c_p * \rho} \tag{4-13}$$

where T is the temperature, t is the time, $\dot{\varepsilon}$ is the strain rate, σ is the flow stress, c_p is the specific heat, and ρ is the density.

Figure 4-36 shows the total temperature rise due to deformation accounts for 14% of the total temperature rise for the lower temperature condition. The total temperature rise for the

134

higher temperature test only accounts for 7% of the temperature rise is due to deformation heating. These results support flow stress curves which indicate a greater amount of strain hardening is experienced by the lower peak temperature, lower rotational speed condition.
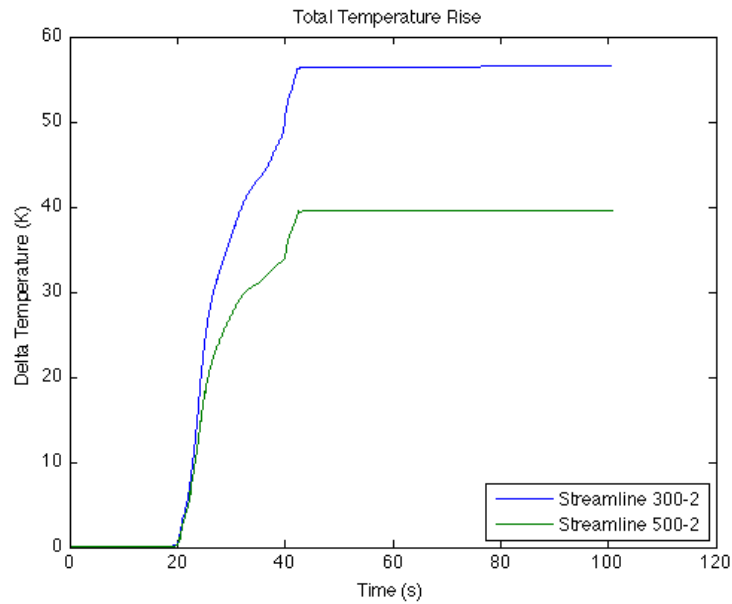
Figure 4-36 Total temperature rise due to deformation.

4.6 Discussion

The model predicted behavior shows some experimentally-observed FSP trends, but there are significant quantitative differences. The greatest difference was observed with X-force whose predicted value ranged from 7 to 25 times greater than the measured value (greatest difference at low rotational speed). Predicted power ranged 3 to 7 times less than the measured value (largest difference at low rotational speed). The remaining output variables evaluated, such as cooling rate, peak HAZ temperature and state variable varied up to 1.8 times greater; the

highest magnitude of difference observed at high rotational speeds. In all cases, the least

quantitative difference is observed at the intermediate rotational speed. At the intermediate

travel speed, the predicted peak temperatures is 0.95 to 0.96 Tm; an ideal peak temperature

regime for this process as reported by others. The predicted temperatures at low rotational speed

are 0.73 to 0.75 Tm and 1.04 to 1.05 Tm at the high rotational speeds. At temperatures above the

material's melting temperature, it seems unlikely to me that the model can accurately model

material properties since they are above the material's melting temperature. It is not surprising

to me that the model does not work well under these conditions. At the other extreme, where the

model predicts temperatures 0.73 to 0.75 Tm, the model provides large departure from measured

data. The author believes that model trends are most reliable at temperatures that are ideal for

material flow for FSP process and not reliable for describing trends above the material's melting

temperature and lower than ideal processing temperatures for the strain rates and strains

predicted within this evaluation.

The flow stress measured in compression tests is approximately half of the flow stress

predicted by the model. While the model lacks quantitative agreement with flow stress, trends of

increasing flow stress with decrease in temperature is consistent with previous results shown in

compression test data and other compression test results reported in Chapter 3. The flow stress

modeled for the higher HAZ peak temperature (total $\varepsilon = 1$ and $\dot{\varepsilon}$ ranging from 0 to 0.12)

quantitatively represents the compression test flow stress behavior, while the flow stress modeled

for the lower HAZ peak temperature, under equivalent strain rate and strain histories, did not.

Similar to previous observation, model predictions at relatively low temperatures for equivalent

strain and strain rate conditions are not reliable.

4.7 Conclusions

Isaiah, a 3D finite element code, was used to simulate friction stir processing of 304L stainless steel over the range of the nine experimental processing parameters (three rotational and three travel speeds) conducted. Streamlines from select simulations were then physically simulated to provide a physical metallographic representation of those specific thermo-mechanical histories.   Results from experimental, numerical and physically-simulated data were used to assess the code in two specific areas; (1) to provide a qualitative and quantitative assessment of how accurate the simulation trends are relative to those observed from experimental data and to **(2)** assess of how well internal constitutive models describe state variable evolution and plastic flow stress of friction stirred material.

The following conclusions are derived from an assessment of predicted temperature results:

The predicted maximum temperature for all nine processing conditions occurred at the probe-to-workpiece interface and ranged from 1237 K (0.73Tm) to 1783 K (1.05Tm). The peak temperatures at the low rotational speed were too cold (0.73 – 0.75Tm) and those at the high rotational speed were too hot (1.04 – 1.05 Tm). The peak temperatures predicted at the intermediate rotational speed were on the upper shelf (0.95-0.96 Tm) of what the expected temperatures for this process.

The predicted peak temperature is most sensitive to changes in rotational speed and almost insensitive to changes in travel speed. Peak temperature increases with increasing rotational speed.

Comparison between the advancing and retreating side peak HAZ temperatures at a distance 0.157 inch from the processing centerline revealed that the advancing side temperature

is equal to or higher than the retreating side's. This difference in peak HAZ temperature increases with increasing travel speeds. The differences in HAZ peak temperatures ranges from 0 to 10°C, 40 to 60°C and 0 to 80°C for the low, intermediate and high rotational speeds, respectively. The heating and cooling rates are similar.

The ratio of the predicted to measured HAZ peak temperature profiles is lowest at the low rotational speed and increases with increasing rotational speed and increasing travel speed.

Comparison of predicted power and X-force data to experimental data revealed the following conclusions:

Measured power decreases with decreasing travel speed and increases with increasing rotational speed while predicted power primarily varies as a function of rotational speed. Measured power is 3 times greater in magnitude than predicted power at high rotational speeds and increases to 6.7 times greater at the lowest rotational speed. Overall, the predicted values correlate with measured power output results, albeit not perfect, (R^2 = 0.6665). The goodness of fit correlation increases when evaluated for a given set of rotational speeds. At intermediate and high rotational speeds, R^2 = 0.9924 and 0.9378, respectively and less favorable at the low rotational speed (R^2= 0.5080).

Predicted X-force values are relatively high at low rotational speeds relative to those at intermediate and high rotational speeds while measured X-force was relatively high at both low and high rotational speeds. Predicted X-forces were up to 25 times higher at the lowest rotational speed and approximately 7 times higher at the highest rotational speed. In both cases, X-force increases with increasing travel speed. Overall, predicted X-force had poor correlation to measured data (R^2=0.0955), however high correlation exists within each set of rotational speeds. R^2=0.808a at low, R^2=0.9525 at intermediate and R^2= 0.9118 at high rotational speeds.

Evaluation and comparison of state variable to hardness revealed the following:

Predicted state increases with increasing travel and rotational speed. The greatest amount of difference between predicted and measured strength is observed at the highest rotational speed. The magnitude of difference increases with increasing rotational speed.

The following conclusions were derived from an assessment of streamlines thermo-mechanical histories and flow stress behavior:

Predicted flow stress is approximately half the flow stress of the compression Gleeble tests. The flow stress of the higher peak temperature streamline has qualitative agreement with compression test flow stress while the flow stress for the lower peak temperature streamline at equivalent strain and strain rate did not. The higher temperature predicted flow stress does have a lower flow stress than the lower peak temperature streamline; which follows theoretical and experimental results.

For the low rotational speed, lower temperature streamline, a temperature rise on the order of 14% of the total temperature rise is due to deformation heating.

The temperature rise for the for the higher rotational speed, higher temperature streamline is approximately 7% of the total temperature which may be indicative that other sources of heat, such as heat conduction played a larger role in the total temperature increase.

In general, Isaiah does provide qualitative trends of process outputs over a limited range of parameters but is not recommended for use as a predictive tool but rather a complimentary tool, particularly if weld data can be used to calibrate the model. Once properly calibrated, the Isaiah code is envisioned to be good tool to help gain insight into the process over the range to which the model has been calibrated.

5   CONCLUSIONS AND RECOMMENDATIONS FOR FUTURE WORK

Three major thrust areas were discussed in this dissertation, experimental, physical simulations and model simulations.

5.1   Experimental

AISI type 304L stainless steel was friction stir processed over the range of the nine experimental processing parameters (three rotational and three travel speeds). These plates were instrumented with thermocouples to obtain temperature profiles at plate mid-thickness for various distances from the centerline. Process output variables were collected, calculated or characterized. Linear regression analysis was used to develop relationships, if any, between input parameters to various output variables. The following conclusions were derived from this evaluation:

High confidence fitted models for spindle torque, spindle power, specific weld energy, cooling rate, and peak HAZ temperature were developed.

Spindle torque is more influenced by changes rotational speed to a greater extent than by changes in travel speed. Spindle torque decreases with increasing rotational speed and decreasing travel speeds with other things being equal.

Spindle power is a function of both travel and rotational speeds and increases with an increase in either parameter.

Specific weld energy has a greater sensitivity to changes in travel speed than to changes in rotational speed, particularly between 2 IPM to 4 IPM. Specific weld energy decreases with an increase in travel speed. Specific weld energy decreased slightly with decreasing rotational.

A high confidence correlation between hardness or grain size to process parameters was not possible from this experimental data set. However, a low confidence model did show that grain size is inversely proportional to travel speed.

These relationships developed for spindle torque, spindle power and grain size in 304L SS are in good agreement with qualitative trends reported for aluminum alloys.

The peak HAZ temperature decreases as travel speed increases. Little to no change is observed with changes in rotational speeds. The insensitivity of temperature to changes in rotational speed is surprising since a large number of authors report increased in temperature with increasing rotational speed. However, it is reasonable to speculate that at distances away from the stir zone region, particularly for low thermal diffusivity materials, the effects of changing processing parameters may not be as significant.

Similarly, cooling rates are mostly affected by changes in travel speed. Changes in rotational speed had little to no effect on the change in cooling rate.

5.2   Physical Simulations

Controlled physical simulations conducted on 0.25 in (6.40 mm) diameter 304L SS cylindrical specimens using a Gleeble 1500 system at strain rates of 10 s^{-1}, 50 s^{-1}, and 100 s^{-1} each at peak temperature of 900˚C, 1000˚C, and 1100˚C provided the following conclusions:

The flow curves observed for 304L SS are characteristic of low stacking fault energy materials. The curves exhibit a strain or work hardening during the linear yielding portion of the curve followed by an exponential increase of stress after yielding. In this exponential portion of the curve, work hardening and recovery occur simultaneously, called dynamic recovery (DRV). The onset of dynamic recrystallization (DRX) occurs at peak strain where flow stress begins a gradual decent from the peak stress. The primary softening mechanism for specimens deformed at 900°C is DRV while DRX is the main softening mechanism at the higher deformation temperatures.

The regression model developed to predict peak stress, σ_p, as a function of temperature and strain rate shows that σ_p increases as the deformation temperature decreases and strain rate increases. The regression model developed to predict grain size as a function of peak temperature and strain rate indicates that grain size decreases with decreasing temperature and increasing strain rate. Since peak stress is a function of temperature and strain rate, a regression model was also developed that shows grain size dependence on peak stress. Temperature and strain rate can be correlated with hardness, however, the R^2 value of 0.636 indicates there are other unknown variables outside the scope of this dissertation that should be included to increase model fit.

5.3   Model Simulations and Comparisons to Experimental Data

Model simulations were conducted over a range of three rotational speeds and three travel speeds representing the welding envelope in friction stir processing experimental trials. Simulations were conducted by using a realistic computational model domain representing actual

tool size and geometry (convex shoulder and tapered probe design) and processing conditions, i.e., single-sided, partial penetration processing in 304L SS plate. A summary of the regression analysis are illustrated in Figure 2-43. The cross hatch symbol by the output process variable indicates that trends from model predictions did not match those for the measured FS data.

Table 5-1 Summary of Measured and Predicted Trends

		Travel Speed		Rotational Speed	
		Measured	Predicted	Measured	Predicted
Peak Temp	⊘	decreasing (red)	flat (red)	increasing (green)	increasing (green)
Peak HAZ Temp	✓	decreasing (green)	decreasing (green)	increasing (green)	increasing (green)
Cooling Rate	⊘	none	decreasing (red)	peak/inverted-V (red)	increasing (red)
Power	⊘	increasing (red)	flat (red)	increasing (green)	increasing (red)
X-Force	⊘	increasing (green)	increasing (green)	V-shape (red)	increasing (red)
Hardness	⊘	increasing (green)	increasing (green)	none	decreasing (red)

The predicted maximum temperatures at all nine processing conditions occurred at the probe-to-workpiece interface. The peak temperatures ranged from 1237 K (0.73Tm) to 1783 K (1.05Tm). The homologous temperatures at the low rotational speed were too cold (0.73 – 0.75) and those at the high rotational speed were too hot (1.04 – 1.05). The peak temperatures predicted at the intermediate rotational speed were on the upper shelf (0.95-0.96) of the expected values for this process. Results indicate that the predicted peak temperature is most sensitive to changes in rotational speed and almost insensitive to changes in travel speed. Peak temperature increases with increasing rotational speed.

Comparison between the advancing and retreating side peak HAZ temperatures at a distance 0.157 inch from the processing centerline revealed that the advancing side temperature is equal to or higher than the retreating side's. This difference (advancing side – retreating side) peak HAZ temperature increases with increasing travel speeds. These differences range from 0 to 10°C, 40 to 60°C and 0 to 80°C for the low, intermediate and high rotational speeds, respectively. In all nine cases, the heating and cooling rates are similar for both advancing and retreating sides. The ratio of the predicted to measured HAZ peak temperature profiles is lowest at the low rotational speed and increases with increasing rotational speed and increasing travel speed.

Measured power decreases with decreasing travel speed and increases with increasing rotational speed while predicted power primarily varies as a function of rotational speed. Measured power is 3 times greater in magnitude than predicted power at high rotational speeds and approximately 6.7 times greater at the lowest rotational speed. The trend predicted power relative to measured power is concerning, particularly since the model over predicted all other values. Overall, predicted power correlates with measured power output results, albeit not perfect, (R^2 = 0.6665). The goodness of fit correlation increases when evaluated for a given set of rotational speeds. At intermediate and high rotational speeds, R^2 = 0.9924 and 0.9378, respectively and less favorable at the low rotational speed (R^2= 0.5080).

Predicted X-force values are relatively high at low rotational speeds relative to those at intermediate and high rotational speeds while measured X-force was relatively high at both low and high rotational speeds. Predicted X-forces were up to 25 times higher at the lowest rotational speed and approximately 7 times higher at the highest rotational speed. These high predicted values are also concerning. In both cases, X-force increases with increasing travel

speed.   Overall, predicted X-force had poor correlation to measured data (R^2=0.0955), however high correlation exists within each set of rotational speeds. R^2=0.808a at low, R^2=0.9525 at intermediate and R^2= 0.9118 at high rotational speeds.

Predicted state increases with increasing travel and rotational speed. The greatest amount of difference between predicted and measured strength is observed at the highest rotational speed.

5.4   Physical Simulations of Model Streamlines and Comparisons to Model

Physical simulations were conducted to replicate the model predicted thermomechanical histories along a single streamline, to provide a physical metallographic representation of those specific thermomechanical histories and means to evaluate the model's constitutive equations since the Gleeble's boundary conditions are frictionless. One streamline was extracted from a low rotational speed condition and the second from a high rotational speed condition, both at 2 IPM.

Predicted flow stress is approximately half the flow stress of the compression Gleeble tests. The flow stress of the higher peak temperature streamline has qualitative agreement with compression test flow stress while the flow stress for the lower peak temperature streamline at equivalent strain and strain rate did not.   The higher temperature predicted flow stress does have a lower flow stress than the lower peak temperature streamline; which is in agreement with experimental results in Chapter 3.

For the low rotational speed, lower temperature streamline, a temperature rise on the order of 14% of the total temperature rise is due to deformation heating. The temperature rise for

the for the higher rotational speed, higher temperature streamline is approximately 7% of the total temperature which may be indicative that other sources of heat, such as heat conduction played a larger role in the total temperature increase.

In general, Isaiah does provide qualitative trends of process outputs over a limited range of parameters but is not recommended for use as a predictive tool but rather a complimentary tool, particularly if weld data can be used to calibrate the model. Once properly calibrated, the Isaiah code is envisioned to be good tool to help gain insight into the process over the range to which the model has been calibrated.

5.5   Recommendations for Future Work

The following recommendations are provided for future efforts:

Evaluate the effects adiabatic heating, chemical composition, presence and distribution of second phases to temperature dependent material constants and other material model variables such as activation energy, strain rate sensitivity, strain hardening and softening mechanisms and determine to account for critical temperature dependent variables within the model.

Perform regression analysis on a larger data set for those related to grain size and strain rate to obtain higher confidence models. Performing additional regression models to interaction effects is also recommended.

Evaluate means to properly model boundary conditions, particularly at the tool to workpiece interface.

Understand why predicted power is under predicted while peak temperatures and forces are over predicted.

REFERENCES

1. Posada, M., et al., *Friction stir weld evaluation of DH-36 and stainless steel weldments.* Friction Stir Welding and Processing TMS, 2001: p. 159-171.

2. K. Okamota, S.h., M. Inagaki, S.H-C., Park, Y.S. Sato, H. Kokawa, T.W. Nelson and C.D. Sorensen *Metallurgical and mechanical properties of friction stir welded stainless steels.* 4th International Symposium on Friction Stir Welding, 2003.

3. Reynolds, A., et al., *Structure, properties, and residual stress of 304L stainless steel friction stir welds.* Scripta materialia, 2003. 48(9): p. 1289-1294.

4. Reynolds, A.P., M. Posada, J. DeLoach, M.J. Skinner, J. Halpin and T.J. Lienert *FSW of Austenitic Stainless Steels.* 3rd International Symposium on Friction Stir Welding, 2001.

5. Park, S., et al., *Microstructural characterisation of stir zone containing residual ferrite in friction stir welded 304 austenitic stainless steel.* Science and Technology of Welding &# 38; Joining, 2005. 10(5): p. 550-556.

6. Sterling, C.J., *Effects of friction stir processing on microstructure and mechanical properties of fusion welded 304L stainless steel*, in *Mechanical Engineering*2004, Brigham Young University: Provo.

7. H. Kokawa, S.H.-C., Park, Y.S. Sato, K. Okamota, S. Hirano and M. Inagaki *Microstructural evolution of 304 austenitic stainless steel during friction stir welding.* Proceedings of the Fourteenth International Offshore and Polar Engineering Conference, 2004.

8. Park, S.H.C., et al., *Rapid formation of the sigma phase in 304 stainless steel during friction stir welding.* Scripta materialia, 2003. 49(12): p. 1175-1180.

9. Clark, T.D., *An analysis of microstructure and corrosion resistance in underwater frictin stir welded 304L stainless steel*, in *Mechanical Engineering*2005, Brigham Young University: Provo.

10. Okamota, K., Hirano, S., Inagaki, M., Park, S.H. C., Sato, Y.S. , Kokawa, H. , Nelson, T.W., and Sorensen, C.D. , *Metallurgical and mechanical properties of friction stir welded stainless steels*, in *4th International Symposium on Friction Stir Welding*14-16 May 2003: Park City, Utah, USA.

11. Park, S.H.C., et al., *Corrosion resistance of friction stir welded 304 stainless steel.* Scripta materialia, 2004. 51(2): p. 101-105.

12. Sato, Y.S., T.W. Nelson, and C.J. Sterling, *Recrystallization in type 304L stainless steel during friction stirring.* Acta materialia, 2005. 53(3): p. 637-645.

13. Sato, Y., M. Urata, and H. Kokawa, *Parameters controlling microstructure and hardness during friction-stir welding of precipitation-hardenable aluminum alloy 6063.* Metallurgical and Materials Transactions A, 2002. 33(3): p. 625-635.

14. Rhodes, C., et al., *Fine-grain evolution in friction-stir processed 7050 aluminum.* Scripta materialia, 2003. 48(10): p. 1451-1455.

15. Yang, B., et al., *Banded microstructure in AA2024-T351 and AA2524-T351 aluminum friction stir welds: Part I. Metallurgical studies.* Materials Science and Engineering: A, 2004. 364(1): p. 55-65.

16. Hassan, K.A.A., A.F. Norman, D.A. Price, P.B. Prangell, *Stability of nugget zone grain structures in high strength Al-alloy friction stir welds during solution treatment.* Acta Materialia, 2003. 51(7): p. 13.

17. Reynolds, A., et al., *Relationships between weld parameters, hardness distribution and temperature history in alloy 7050 friction stir welds.* Science and Technology of Welding &# 38; Joining, 2005. 10(2): p. 190-199.

18. Long, T., Tang, W., Reynolds, A.P., *Process Response Parameter Relationships in Aluminum Alloy Friction Stir Welds.* Science and Technology of Welding and Joining, 2007. 12(4): p. 6.

19. P. Kalya, K.K., R.S. Mishra and J.A. Baumann, *Specific Energy and Temperature Mechanistic Model for Friction Stir Processing of AL-F357*, 2007, The Minerals, Metals and Materials Society (TMS).

20. Hamilton, C., Dymek, S., and Sommers, A., *Characteristic Temperature Curves for Aluminum Alloys During Friction Stir Welding.* Welding Journal, 2010. 89(September): p. 189-s-194-s.

21. Cui, S., Z. Chen, and J. Robson, *A model relating tool torque and its associated power and specific energy to rotation and forward speeds during friction stir welding/processing.* International Journal of Machine Tools and Manufacture, 2010. 50(12): p. 1023-1030.

22. Owen, C.B., *Two Dimensional Friction Stir Welding Model and Experimental Validation*, in *Mechanical Egineering*2006, Brigham Young University: Provo.

23. Lee, W.S. and C.F. Lin, *Impact properties and microstructure evolution of 304L stainless steel.* Materials Science and Engineering: A, 2001. 308(1): p. 124-135.

24. Kim, S.I. and Y.C. Yoo, *Dynamic recrystallization behavior of AISI 304 stainless steel.* Materials Science and Engineering: A, 2001. 311(1): p. 108-113.

25. Ryan, N. and H. McQueen, *Dynamic softening mechanisms in 304 austenitic stainless steel.* Canadian Metallurgical Quarterly, 1990. 29(2): p. 147-162.

26. Medina, S.F. and C.A. Hernandez, *General expression of the Zener-Hollomon parameter as a function of the chemical composition of low alloy and microalloyed steels.* Acta materialia, 1996. 44(1): p. 137-148.

27. Medina, S.F., and C.A. Hernandez, *Modelling of the Dynamic Recrystallization of Austenite in Low ALloy and Microslloyed Steels.* Acta Materialia, 1996. 44(1): p. 6.

28. Hernández, C.A., S.F. Medina, and J. Ruiz, *Modelling austenite flow curves in low alloy and microalloyed steels.* Acta materialia, 1996. 44(1): p. 155-163.

29. Medina, S.F. and C.A. Hernandez, *The influence of chemical composition on peak strain of deformed austenite in low alloy and microalloyed steels.* Acta materialia, 1996. 44(1): p. 149-154.

30. Barraclough, D. and C. Sellars, *Static recrystallization and restoration after hot deformation of type 304 stainless steel.* Metal Science, 13, 1979. 3(4): p. 257-268.

31. Ryan, N., *Comparison of dynamic softening in 301, 304, 316 and 317 Stainless Steels.* High Temp. Technol., 1990. 8(3): p. 15.

32. Ryan, N. and H. McQueen, *Work Hardening, Strength and Ductility in the Hot Working of 304 Austenitic Stainless Steel.* High Temp. Technol., 1990. 8(1): p. 27-44.

33. Arbegast, W., ed. *Modeling Friction Stir Joining as a Metalworking Process.* Hot Deformation of Aluminum Alloys III, ed. A.B. Z. Jin, T.A. Bieler and B. Radhakrishnan. 2003, TMS. 313-327.

34. Semiatin, S. and J. Holbrook, *Plastic flow phenomenology of 304L stainless steel.* Metallurgical and Materials Transactions A, 1983. 14(8): p. 1681-1695.

35. Peet, M. and A. Shirzadi, *Neural network modelling of hot deformation of austenite.* 2001.

36. El Wahabi, M., J. Cabrera, and J. Prado, *Hot working of two AISI 304 steels: a comparative study.* Materials Science and Engineering: A, 2003. 343(1): p. 116-125.

37. Dehghan-Manshadi, A., M.R. Barnett, and P. Hodgson, *Recrystallization in AISI 304 austenitic stainless steel during and after hot deformation.* Materials Science and Engineering: A, 2008. 485(1): p. 664-672.

38. Padilha, A.F., R.L. Plaut, and P. Bios, *Annealing of cold-worked austenitic stainless steels.* ISIJ International(Japan), 2003. 43(2): p. 135-143.

39. Barbucci, A., G. Cerisola, and P. Cabot, *Effect of cold-working in the passive behavior of 304 stainless steel in sulfate media.* Journal of the Electrochemical Society, 2002. 149: p. B534.

40. Lee, W.S. and C.F. Lin, *The morphologies and characteristics of impact-induced martensite in 304L stainless steel.* Scripta materialia, 2000. 43(8): p. 777.

41. Voort, G.V., ed. *ASM Handbook, Metallography and Microstructures*. Vol. 9. 2004, ASM International. 1184.

42. Singh, J., *Influence of deformation on the transformation of austenitic stainless steels.* Journal of Materials Science, 1985. 20(9): p. 3157-3166.

43. Meyers, M., et al., *Microstructural evolution in adiabatic shear localization in stainless steel.* Acta materialia, 2003. 51(5): p. 1307-1325.

44. Ryan, N. and H. McQueen, *Comparison of static softening in 300 series stainless steels under iso-and anisothermal conditions.* Materials science and technology, 1991. 7(9): p. 818-826.

45. Seidel, T. and A. Reynolds, *Two-dimensional friction stir welding process model based on fluid mechanics.* Science and Technology of Welding &# 38; Joining, 2003. 8(3): p. 175-183.

46. Colegrove, P. and H. Shercliff, *Development of Trivex friction stir welding tool Part 2 &# 8211; three-dimensional flow modelling.* Science and Technology of Welding &# 38; Joining, 2004. 9(4): p. 352-361.

47. Colegrove, P.A., H.R. Shercliff, *Development of Trivex Friction Stir Welding Tool Part 1 - Two Dimensional Flow Modeling and Experimental Validation.* Science and Technology of Welding and Joining, 2004. 9(4): p. 6.

48. Colegrove, P.a.H.R.S., *Modelling the Friction Stir Welding o Aerospace Alloys*, in *Proceedings from teh 5th International Symposium on Friction Stir Welding*2004: Metz, France.

49. Askari, A., et al., *Modeling and analysis of friction stir welding processes.* Friction Stir Welding and Processing VI, 2001: p. 43-54.

50. Schmidt, H., J. Hattel, and J. Wert, *An analytical model for the heat generation in friction stir welding.* Modelling and Simulation in Materials Science and Engineering, 2004. 12: p. 143.

51. Zhu, X. and Y. Chao, *Numerical simulation of transient temperature and residual stresses in friction stir welding of 304L stainless steel.* Journal of Materials Processing Technology, 2004. 146(2): p. 263-272.

52. Cho, J.H., Dawson, P.R., Boyce, B.E. *2D Modeling of Friction Stir Welding by Eulerian Formulation*. in *American Institute of Physics*. 2004. American Institute of Physics.

53. Dewhurst, T., Dawson, PR, *A Finite Element Program for Viscoplastic Flow and Heat Transfer in Three Dimensions*, 1985.

54. Cho, J., D. Boyce, and P. Dawson, *Modelling of strain hardening during friction stir welding of stainless steel.* Modelling and Simulation in Materials Science and Engineering, 2007. 15: p. 469.

55. Cho, J.H., D.E. Boyce, and P.R. Dawson, *Modeling strain hardening and texture evolution in friction stir welding of stainless steel.* Materials Science and Engineering: A, 2005. 398(1): p. 146-163.

56. Nandan, R., Roy, G.G, DeBroy, T., *Numerical Simulation of Three Dimensional Heat Transfer and Plastic Flow During Friction Stir Welding.* Metallurgical and Materials Transactions A, 2006. 37A(April): p. 11.

57. Nandan, R., et al., *Numerical modelling of 3D plastic flow and heat transfer during friction stir welding of stainless steel.* Science and Technology of Welding &# 38; Joining, 2006. 11(5): p. 526-537.

58. Nandan, R., Roy, G.G, Lienert, T.J., DeBroy, T., *Three-Dimensional Heat and Material Flow During Friction Stir Welding of Mild Steel.* Acta materialia, 2007. 55: p. 12.

59. Forrest, D.R., Nguyen, J.P., Posada, M., Deloach, J.J. Boyce, D., Cho, J., Dawson, P. . *Simulation of HSLA-65 Friction Stir Welding.* in *7th International Conference on Trends and Welding Research*. 2006. Pine Mountain, GA.

60. Posada, M., *Friction Stir Welding of HSLA-65 Steel*, in *ONR Seaborne Marterials Review*2003: Naval Surface Warfare Center, Carderock Divison, W. Bethesda, MD.

61. Norton, S., *Friction Stir Weld Physical Simulation*, in *Welding Engineering*2006, The Ohio State University.

62. Sinfield, M., Lippold, J.C., Alexandrov, B.T. *Physical Simulation of Friction Stir Weld Microstructure of High-Strength Low Alloy Steel (HSLA-65)*. in *7th International Friction Stir Technology Symposium*. 2007. Japan.

63. Dawson, P.R., 2004.

64. Roebuck, B., Lord, J.D. and Varma, R.K., *Guidelines for the Measurement of Flow Stress in Hot Axisyetric Compression Tests, Best Practices in Measurement Series* N.P. Laboratory, Editor 1996: Teddington, Middlessex, UK.

65. Kuykendall, K., *An Evaluation of Constitutive Laws and their Ability to Predict Flow Stress over Large Variations in Temperature, Strain and Strain Rate Characteristic Friction Stir Welding*, in *Mechanical Engineering*August 2001, Brigham Young Universtiy.

APPENDIX A

APPENDIX A-1: MEGA STIR TOOL DRAWING
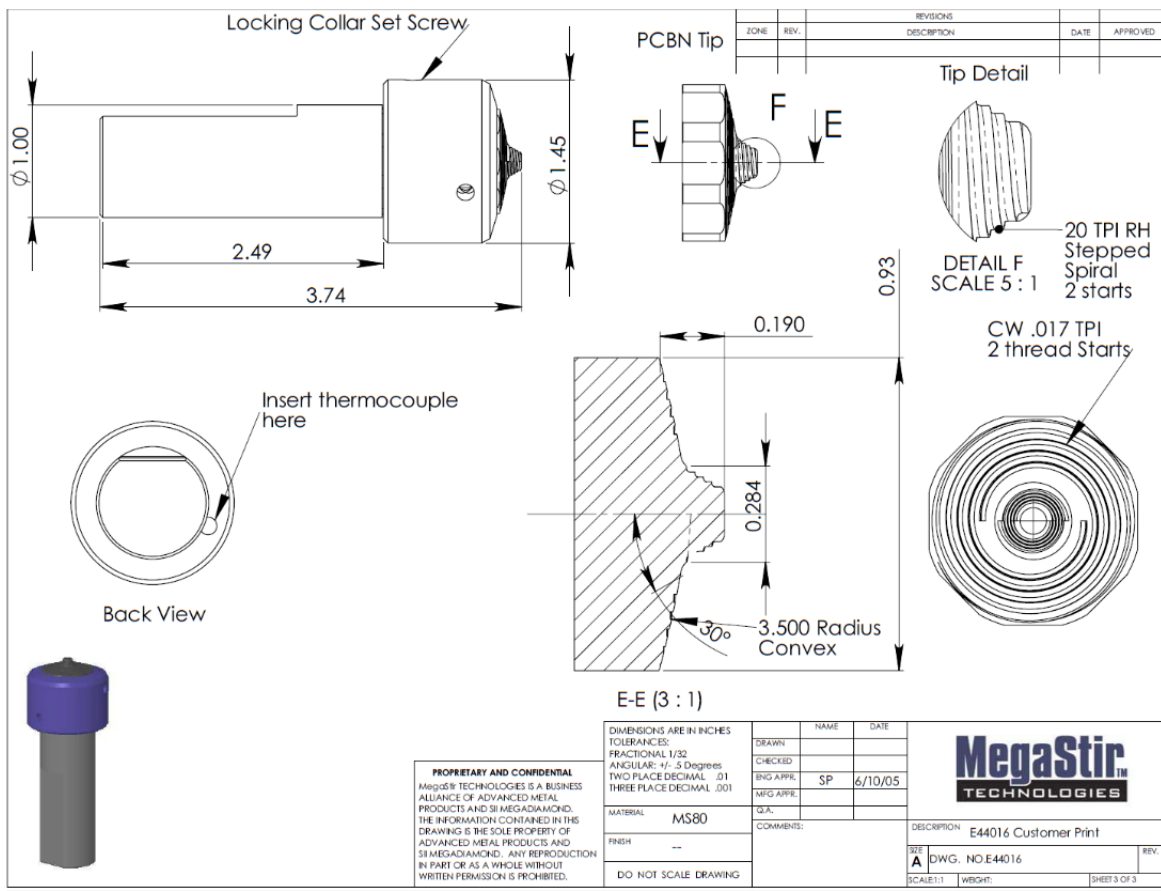
Figure A- 1 E44016 MegaStir tool design used in experimental trials

APPENDIX A-2 REGRESSION SUMMARY OUTPUT FOR LN SPINDLE TORQUE

Table A-1 Regression Summary Output for ln Spindle Torque

SUMMARY OUTPUT		Ln Spindle Torque (Nm)				
Regression Statistics						
Multiple R	0.98074557					
R Square	0.96186188					
Adj R Square	0.94914918					
Std Error	0.0362539					
Observations	9					

ANOVA						
	df	SS	MS	F	Sig F	
Regression	2	0.1988906	0.099445309	75.6614597	5.54725E-05	
Residual	6	0.0078861	0.001314346			
Total	8	0.2067767				

	Coefficients	Std Error	t Stat	P-value	Lower 95%	Upper 95%	Lower 95.0%	Upper 95.0%
Intercept	4.11759825	0.0228993	179.8133998	1.996E-12	4.061565716	4.173630779	4.061565716	4.173630779
Ln (Norm RPS)	-0.423514	0.0577942	-7.32796874	0.00032998	-0.56493129	-0.28209672	-0.56493129	-0.282096721
Ln (Norm TS)	0.26322985	0.0266414	9.880475365	6.2028E-05	0.198040652	0.328419041	0.198040652	0.328419041

RESIDUAL OUTPUT

Observation	Predicted Y	Residuals	Std Residuals
1	4.04475251	0.0409291	1.303607218
2	4.22720954	-0.032552	-1.03679321
3	4.33394005	-0.010994	-0.35016321
4	3.92291512	0.0006032	0.019213662
5	4.10537215	-0.019509	-0.62136195
6	4.21210267	0.0248962	0.792953297
7	3.8284107	-0.006405	-0.20401715
8	4.01086773	-0.043116	-1.37325617
9	4.11759825	0.0461476	1.469817513

APPENDIX A-3 REGRESSION ANALYSIS FOR LN(SPINDLE POWER) (KW)

Table A-2 Regression Analysis for ln(Spindle Power) (kW)

SUMMARY OUTPUT			Ln (Spindle Power) (kW)					
Regression Statistics								
Multiple R	0.98511974							
R Square	0.9704609							
Adj R Square	0.96061453							
Standard Error	0.0362539							
Observations	9							
ANOVA								
	df	SS	MS	F	Sig F			
Regression	2	0.25908461	0.129542305	98.560305	2.5775E-05			
Residual	6	0.00788607	0.001314346					
Total	8	0.26697068						
	Coefficients	Std Error	t Stat	P-value	Lower 95%	Upper 95%	Lower 95.0%	Upper 95.0%
Intercept	1.16747648	0.02289928	50.98309823	3.82E-09	1.11144395	1.223509016	1.111443954	1.22350902
Ln(RPM/max RPM)	0.57648599	0.05779419	9.974809073	5.876E-05	0.43506871	0.717903279	0.43506871	0.71790328
Ln (TS/max TS)	0.26322985	0.02664142	9.880475365	6.203E-05	0.19804065	0.328419041	0.198040652	0.32841904

RESIDUAL OUTPUT				
Observation	Predicted Y	Residuals	Std Residuals	
1	0.58380512	0.0409291	1.303607218	
2	0.76626215	-0.032552	-1.03679321	
3	0.87299267	-0.010994	-0.35016321	
4	0.74964981	0.00060325	0.019213662	
5	0.93210683	-0.0195088	-0.62136195	
6	1.03883735	0.0248962	0.792953297	
7	0.87828894	-0.0064055	-0.20401715	
8	1.06074597	-0.0431159	-1.37325617	
9	1.16747648	0.04614757	1.469817513	

APPENDIX A-4 REGRESSION OUTPUT SUMMARY OF LN(SPECIFIC WELD ENERGY) (KJ/IN) AS A FUNCTION OF LN(RPM/MAX RPM) AND LN(TS/MAX TS)

Table A-3 Regression Output Summary of ln(Specific Weld Energy(SWE)) (kJ/in) as a Function of ln(RPM/max RPM) and ln(TS/max TS)

SUMMARY OUTPUT			Ln(Weld Energy) (kJ/in)					
Regression Statistics								
Multiple R	0.99654695							
R Square	0.99310582							
Adj R Square	0.99080776							
Std Error	0.0362539							
Observations	9							
ANOVA								
	df	SS	MS	F	Sig F			
Regression	2	1.13598841	0.567994205	432.1498	3.2768E-07			
Residual	6	0.007886074	0.001314346					
Total	8	1.143874484						
	Coefficients	Std Error	t Stat	P-value	Lower 95%	Upper 95%	Lower 95.0%	Upper 95.0%
Intercept	3.47006158	0.022899285	151.5358061	5.57E-12	3.41402905	3.52609411	3.41402905	3.52609411
Ln(RPM/max RPM)	0.57648599	0.057794188	9.974809073	5.88E-05	0.43506871	0.71790328	0.43506871	0.71790328
Ln(TS/max TS)	-0.7367702	0.026641415	-27.6550681	1.48E-07	-0.8019593	-0.671581	-0.80195935	-0.671581
RESIDUAL OUTPUT								
Observation	Predicted Y	Residuals	Std Residuals					
1	3.9850025	0.040929099	1.303607218					
2	3.47431235	-0.03255199	-1.03679321					
3	3.17557776	-0.01099401	-0.35016321					
4	4.15084719	0.000603248	0.019213662					
5	3.64015704	-0.01950878	-0.62136195					
6	3.34142245	0.024896198	0.792953297					
7	4.27948632	-0.00640549	-0.20401715					
8	3.76879617	-0.04311585	-1.37325617					
9	3.47006158	0.04614757	1.469817513					

APPENDIX A-5 REGRESSION OUTPUT SUMMARY OF LN(COOLING RATE ΔT_{8-5}) (°C/S) AS A FUNCTION OF LN(RPS/MAX RPS) AND LN(TS/MAX TS)

Table A-4 Regression Output Summary of ln(Cooling Rate ΔT_{8-5}) (°C/s) as a Function of ln(RPS/max RPS) and ln(TS/max TS)

SUMMARY OUTPUT		Ln Cooling Rate (ΔT_{8-5}) (°C/s)							
Regression Statistics									
Multiple R	0.9922856								
R Square	0.984630711								
Adj R Square	0.979507615								
Std Error	0.058356484								
Observations	9								
ANOVA									
	df	*SS*	*MS*	*F*	*Sig F*				
Regression	2	1.309028504	0.654514252	192.1944603	3.63046E-06				
Residual	6	0.020432876	0.003405479						
Total	8	1.329461379							
	Coefficients	*Std Error*	*t Stat*	*P-value*	*Lower 95%*	*Upper 95%*	*Lower 95.0%*	*Upper 95.0%*	
Intercept	4.097533976	0.036860078	111.1645506	3.57234E-11	4.007340615	4.187727337	4.007340615	4.187727337	
Ln (RPS/max RPS)	-0.103180189	0.093029031	-1.109118174	0.309844637	-0.33081403	0.12445365	-0.330814028	0.12445365	
Ln(TS/max TS)	0.839423281	0.042883638	19.57444195	1.15199E-06	0.734490799	0.944355763	0.734490799	0.944355763	
RESIDUAL OUTPUT									
Observation	*Predicted CR*	*Residuals*	*Std Residuals*						
1	3.228040329	-0.034277205	-0.678243518						
2	3.80988421	0.05441806	1.076770873						
3	4.150241061	0.009422967	0.186452383						
4	3.198357239	-0.018513345	-0.3663238						
5	3.780201119	0.051062922	1.010382727						
6	4.12055797	-0.100227795	-1.983208717						
7	3.175333245	0.024441307	0.483620464						
8	3.757177125	-0.028668387	-0.567261767						
9	4.097533976	0.042341476	0.837811353						

APPENDIX A-6 REGRESSION OUTPUT SUMMARY OF LN (COOLING RATE ΔT8-5)(°C/S) AS A FUNCTION OF LN(TS/MAX TS)

Table A-5 Regression Output Summary of ln (Cooling Rate ΔT_{8-5})(°C/s) as a Function of ln(TS/max TS)

SUMMARY OUTPUT			Ln Cooling Rate (ΔT_{8-5}) (°C/s)						
Regression Statistics									
Multiple R	0.99069654								
R Square	0.98147964								
Adj R Square	0.97883387								
Std Error	0.05930804								
Observations	9								
ANOVA									
	df	SS	MS	F	Sig F				
Regression	1	1.3048393	1.304839277	370.96243	2.5343E-07				
Residual	7	0.0246221	0.003517443						
Total	8	1.3294614							
	Coefficients	Std Error	t Stat	P-value	Lower 95%	Upper 95%	Lower 95.0%	Upper 95.0%	
Intercept	9.13882804	0.2829756	32.29545854	7.059E-09	8.469696977	9.8079591	8.469696977	9.807959097	
Ln (TS/max TS)	0.83942328	0.0435829	19.26038492	2.534E-07	0.736366117	0.94248044	0.736366117	0.942480445	

RESIDUAL OUTPUT			
Observation	Predicted Y	Residuals	Std Residuals
1	3.20057694	-0.006814	-0.12282101
2	3.78242082	0.0818815	1.475937465
3	4.12277767	0.0368864	0.664887573
4	3.20057694	-0.020733	-0.37371927
5	3.78242082	0.0488432	0.8804136
6	4.12277767	-0.102447	-1.84664649
7	3.20057694	-0.000802	-0.01446325
8	3.78242082	-0.053912	-0.97178125
9	4.12277767	0.0170978	0.308192619

APPENDIX A-7 REGRESSION OUTPUT SUMMARY OF LN(PEAK TEMPERATURE) (°C) AS A FUNCTION OF LN(RPM/MAX RPM) AND LN(TS/MAX TS)

Table A-6 Regression Output Summary of ln(Peak Temperature) (°C) as a Function of ln(RPM/max RPM) and ln(TS/max TS)

SUMMARY OUTPUT			Ln (Peak Temperature) (°C)						
Regression Statistics									
Multiple R	0.922538257								
R Square	0.851076835								
Adj R Square	0.80143578								
Std Error	0.028240745								
Observations	9								
ANOVA									
	df	*SS*	*MS*	*F*	*Sig F*				
Regression	2	0.02734702	0.013673512	17.14461617	0.003302834				
Residual	6	0.00478524	0.00079754						
Total	8	0.03213226							
	Coefficients	*Std Error*	*t Stat*	*P-value*	*Lower 95%*	*Upper 95%*	*Lower 95.0%*	*Upper 95.0%*	
Intercept	6.866099236	0.01783788	384.9167405	2.07518E-14	6.822451512	6.90974696	6.822451512	6.90974696	
Ln(RPM/max RPM)	0.085833457	0.04502	1.906562621	0.10520815	-0.02432652	0.195993437	-0.024326524	0.195993437	
Ln(TS/ max TS)	-0.114901052	0.02075289	-5.536628153	0.001464136	-0.16568155	-0.064120552	-0.165681553	-0.064120552	
RESIDUAL OUTPUT									
Observation	*Predicted Y*	*Residuals*	*Std Residuals*						
1	6.948485015	0.02224506	0.909550572						
2	6.868841675	-0.0092268	-0.377261922						
3	6.822253307	-0.0176388	-0.72121033						
4	6.973177762	0.0161575	0.660643986						
5	6.893534422	0.01482068	0.605984163						
6	6.846946054	-0.0204008	-0.834144062						
7	6.992330944	-0.046317	-1.893796032						
8	6.912687604	0.01585021	0.648079607						
9	6.866099236	0.02450988	1.002154018						

APPENDIX A-8 REGRESSION OUTPUT SUMMARY OF LN(PEAK TEMPERATURE) AS A FUNCTION OF LN(TS/MAX TS)

Table A-7 Regression Output Summary of ln(Peak Temperature) as a Function of ln(TS/max TS)

SUMMARY OUTPUT		Ln(Peak Temperature) (°C)						
Regression Statistics								
Multiple R	0.8722698							
R Square	0.7608547							
Adj R Square	0.7266911							
Standard Error	0.0331324							
Observations	9							

ANOVA								
	df	SS	MS	F	Sig F			
Regression	1	0.02444798	0.02444798	22.27091	0.0021595			
Residual	7	0.00768428	0.00109775					
Total	8	0.03213226						

	Coefficients	Std Error	t Stat	P-value	Lower 95%	Upper 95%	Lower 95.0%	Upper 95.0%
Intercept	6.8450995	0.01646147	415.825418	1.23E-16	6.8061743	6.8840247	6.806174331	6.884024734
Ln(Ts/Max TS)	-0.114901	0.02434754	-4.7192061	0.00216	-0.172474	-0.057328	-0.17247383	-0.05732827

RESIDUAL OUTPUT

Observation	Predicted Y	Residuals	Std Residuals
1	6.9713312	-0.0006012	-0.019397
2	6.8916879	-0.032073	-1.0348632
3	6.8450995	-0.040485	-1.3062842
4	6.9713312	0.01800403	0.58091558
5	6.8916879	0.0166672	0.53778171
6	6.8450995	-0.0185543	-0.598671
7	6.9713312	-0.0253172	-0.8168831
8	6.8916879	0.03684992	1.18899475
9	6.8450995	0.04550959	1.46840655

APPENDIX A-9 REGRESSION OUTPUT SUMMARY OF LN(AVERAGE STIR ZONE HARDNESS) (HV) 300gf AS A FUNCTION OF LN(RPM/MAX RPM) AND LN(TS/MAX TS)

Table A-8 Regression Output Summary of ln(Average Stir Zone Hardness) (Hv) 300gf as a Function of ln(RPM/max RPM) and ln(TS/max TS)

SUMMARY OUTPUT				LN(Average Stir Zone Hardness) (Hv) 300gf				
Regression Statistics								
Multiple R	0.78925699							
R Square	0.62292659							
Adjusted R Square	0.49723545							
Standard Error	0.03054942							
Observations	9							
ANOVA								
	df	*SS*	*MS*	*F*	*Sig F*			
Regression	2	0.009250564	0.004625282	4.95601045	0.05361394			
Residual	6	0.005599603	0.000933267					
Total	8	0.014850167						
	Coefficients	*Std Error*	*t Stat*	*P-value*	*Lower 95%*	*Upper 95%*	*Lower 95.0%*	*Upper 95.0%*
Intercept	5.36423756	0.019296126	277.995571	1.4621E-13	5.31702164	5.41145348	5.317021642	5.41145348
Ln(RPM/max RPM)	-0.0873649	0.048700383	-1.7939259	0.12298253	-0.2065304	0.03180067	-0.20653042	0.03180067
Ln(TS/max TS)	0.05808226	0.022449439	2.587247721	0.04136457	0.00315046	0.11301406	0.003150462	0.11301406

RESIDUAL OUTPUT

Observation	Predicted Y	Residuals	Std Residuals
1	5.34505589	0.020055261	0.758044464
2	5.38531545	-0.0288372	-1.08998232
3	5.40886578	0.037846591	1.430517386
4	5.31992259	-0.00878722	-0.33213752
5	5.36018214	-0.03484073	-1.31690266
6	5.38373247	-0.02290755	-0.86585469
7	5.30042768	-1.0355E-06	-3.9141E-05
8	5.34068723	0.03314986	1.252991348
9	5.36423756	0.004322029	0.163363135

APPENDIX A-10 REGRESSION OUTPUT SUMMARY OF LN(AVERAGE STIR ZONE HARDNESS) (HV) 300 gf AS A FUNCTION OF LN(TS/MAX TS)

Table A-9 Regression Output Summary of ln(Average Stir Zone Hardness) (Hv) 300 gf as a Function of ln(TS/max TS)

SUMMARY OUTPUT		Ln(Average Stir Zone Hardness) (Hv) 300gf						
Regression Statistics								
Multiple R	0.648597608							
R Square	0.420678858							
Adj R Square	0.337918694							
Std Error	0.035057128							
Observations	9							
ANOVA								
	df	*SS*	*MS*	*F*	*Sig F*			
Regression	1	0.006247	0.00624715	5.083108	0.0588			
Residual	7	0.008603	0.001229					
Total	8	0.01485						
	Coefficients	*Std Error*	*t Stat*	*P-value*	*Lower 95%*	*Upper 95%*	*Lower 95.0%*	*Upper 95.0%*
Intercept	5.385611937	0.017418	309.202179	9.77E-16	5.3444255	5.4267984	5.34442546	5.426798415
Ln(TS/max TS)	0.058082261	0.025762	2.25457493	0.0588	-0.0028351	0.1189996	-0.00283509	0.118999607
RESIDUAL OUTPUT								
Observation	*Predicted Y*	*Residuals*	*Std Residuals*					
1	5.321802052	0.043309	1.32068372					
2	5.362061607	-0.00558	-0.1702609					
3	5.385611937	0.0611	1.86321911					
4	5.321802052	-0.01067	-0.3252739					
5	5.362061607	-0.03672	-1.1197593					
6	5.385611937	-0.02479	-0.7558644					
7	5.321802052	-0.02138	-0.6518297					
8	5.362061607	0.011775	0.35908596					
9	5.385611937	-0.01705	-0.5200005					

APPENDIX A-11 REGRESSION OUTPUT SUMMARY OF LN(HARDNESS IQR) (HV) AS A FUNCTION OF ROTATIONAL AND TRAVEL SPEED

Table A-10 Regression Output Summary of ln(Hardness IQR) (Hv) as a Function of Rotational and Travel Speed

SUMMARY OUTPUT			LN(IQR)					
Regression Statistics								
Multiple R	0.92051371							
R Square	0.84734549							
Adj R Square	0.79646065							
Std Error	0.08731887							
Observations	9							

ANOVA								
	df	*SS*	*MS*	*F*	*Sig F*			
Regression	2	0.2539325	0.12696626	16.652219	0.00355737			
Residual	6	0.0457475	0.00762458					
Total	8	0.29968						

	Coefficients	*Std Error*	*t Stat*	*P-value*	*Lower 95%*	*Upper 95%*	*Lower 95.0%*	*Upper 95.0%*
Intercept	2.69904025	0.0551538	48.9366383	4.883E-09	2.56408383	2.83399667	2.56408383	2.833996671
LN(RP/RPM$_{max}$)	-0.4022262	0.1391994	-2.8895679	0.0277092	-0.742835	-0.0616175	-0.742835	-0.06161747
LN(TS/TS$_{max}$)	0.32054423	0.0641668	4.99548158	0.0024634	0.16353365	0.47755481	0.16353365	0.477554813

RESIDUAL OUTPUT

Observation	Predicted Y	Residuals	Std Residuals
1	2.55235388	-0.018657	-0.2467202
2	2.77453821	-0.040171	-0.5312154
3	2.90450771	0.1061132	1.40323554
4	2.43664061	0.0143645	0.18995534
5	2.65882494	-0.149226	-1.9733532
6	2.78879444	0.0266143	0.35194599
7	2.34688642	0.0510089	0.67453864
8	2.56907075	0.0628181	0.83070343
9	2.69904025	-0.052865	-0.6990902

APPENDIX A-12 REGRESSION OUTPUT SUMMARY OF LN(GRAIN SIZE) (μm) AS A FUNCTION OF ROTATIONAL AND TRAVEL SPEED

Table A-11 Regression Output Summary of ln(Grain Size) (μm) as a Function of Rotational and Travel Speed

SUMMARY OUTPUT			Ln(Grain Size) (μm)							
Regression Statistics										
Multiple R	0.855562654									
R Square	0.731987455									
Adj R Square	0.553312425									
Standard Error	0.055358145									
Observations	6									
ANOVA										
	df	*SS*	*MS*	*F*	*Sig F*					
Regression	2	0.025109197	0.012554599	4.09675	0.1387499					
Residual	3	0.009193573	0.003064524							
Total	5	0.03430277								
	Coefficients	*Std Error*	*t Stat*	*P-value*	*Lower 95%*	*Upper 95%*	*Lower 95.0%*	*Upper 95.0%*		
Intercept	1.696775473	0.057831517	29.33997852	8.7E-05	1.5127298	1.8808212	1.51272977	1.88082117		
Ln(RPM/max RPM)	0.124733061	0.126297069	0.987616432	0.39615	-0.277201	0.5266667	-0.2772006	0.5266667		
Ln(TS/max TS)	-0.133510665	0.052215272	-2.55692749	0.08344	-0.299683	0.0326616	-0.299683	0.03266164		

RESIDUAL OUTPUT				
Observation	*Predicted Y*	*Residuals*	*Std Residuals*	
1	1.779735087	-0.04102484	-0.95673075	
2	1.687192546	0.017555546	0.40940882	
3	1.815618553	0.046909988	1.093976929	
4	1.723076011	0.048480751	1.130608329	
5	1.668942095	-0.04166426	-0.97164264	
6	1.843451931	-0.03025718	-0.70562069	

APPENDIX A-13 REGRESSION SUMMARY OUTPUT OF LN(GRAIN SIZE) (μm) AS A FUNCTION OF TRAVEL SPEED

**Table A-12 Regression Summary Output of ln(Grain Size) (μm)
as a Function of Travel Speed**

SUMMARY OUTPUT			Ln(Grain Size) (μm)					
Regression Statistics								
Multiple R	0.80302483							
R Square	0.64484887							
Adj R Square	0.55606109							
Std Error	0.05518756							
Observations	6							
ANOVA								
	df	*SS*	*MS*	*F*	*Sig F*			
Regression	1	0.02212	0.022120103	7.262811	0.0543776			
Residual	4	0.012183	0.003045667					
Total	5	0.034303						
	Coefficients	Std Error	t Stat	P-value	Lower 95%	Upper 95%	Lower 95.0%	Upper 95.0%
Intercept	1.65760622	0.04196	39.50449135	2.453E-06	1.5411067	1.7741057	1.541106742	1.774105701
Ln(TS/max TS)	-0.1393746	0.051717	-2.6949603	0.0543776	-0.282963	0.0042141	-0.28296327	0.004214129
RESIDUAL OUTPUT								
Observation	*Predicted Y*	*Residuals*	*Std Residuals*					
1	1.81072484	-0.07201	-1.45892945					
2	1.71411775	-0.00937	-0.18981799					
3	1.81072484	0.051804	1.049481095					
4	1.71411775	0.057439	1.163645779					
5	1.65760622	-0.03033	-0.61441693					
6	1.81072484	0.00247	0.050037494					

APPENDIX A-14 REGRESSION SUMMARY OUTPUT OF LN(PEAK TEMPERATURE) (°C) AS A FUNCTION OF LN(SPECIFIC WELD ENERGY/MAX SWE)

Table A-13 Regression Summary Output of ln(Peak Temperature) (°C) as a Function of ln(SWE/max SWE)

SUMMARY OUTPUT			Ln(Peak Temperature) (°C)					
Regression Statistics								
Multiple R	0.92635893							
R Square	0.858140867							
Adj R Square	0.837875277							
Std Error	0.025518214							
Observations	9							
ANOVA								
	df	SS	MS	F	Sig F			
Regression	1	0.027574	0.027574007	42.34473	0.00033185			
Residual	7	0.004558	0.000651179					
Total	8	0.032132						
	Coefficients	Std Error	t Stat	P-value	Lower 95%	Upper 95%	Lower 95.0%	Upper 95.0%
Intercept	6.991930319	0.016136	433.3242741	9.21E-17	6.95377578	7.0300849	6.953775779	7.030084858
Ln(WE/WE$_{max}$)	0.155260419	0.023859	6.507282515	0.000332	0.0988417	0.2116791	0.098841699	0.211679139
RESIDUAL OUTPUT								
Observation	Predicted Y	Residuals	Std Residuals					
1	6.953557825	0.017172	0.719404202					
2	6.862859153	-0.003244	-0.135912674					
3	6.819824598	-0.01521	-0.637202001					
4	6.973045932	0.016289	0.682415717					
5	6.890633363	0.017722	0.742423914					
6	6.851146041	-0.024601	-1.0306121					
7	6.991930319	-0.045916	-1.923591467					
8	6.906940685	0.021597	0.904777538					
9	6.874418104	0.016191	0.67829687					

APPENDIX A-15 REGRESSION OUTPUT SUMMARY OF LN(PEAK TEMPERATURE) (°C) AS A FUNCTION OF LN(SPINDLE TORQUE/MAX SPINDLE TORQUE)

Table A-14 Regression Output Summary of ln(Peak Temperature) (°C) as a Function of ln(Spindle Torque/max Spindle Torque)

SUMMARY OUTPUT				Ln(Peak Temperature) (°C)				
Regression Statistics								
Multiple R	0.845899996							
R Square	0.715546804							
Adj R Square	0.674910633							
Std Error	0.036134915							
Observations	9							
ANOVA								
	df	*SS*	*MS*	*F*	*Sig F*			
Regression	1	0.0229921	0.022992137	17.60862	0.00405435			
Residual	7	0.0091401	0.001305732					
Total	8	0.0321323						
	Coefficients	*Std Error*	*t Stat*	*P-value*	*Lower 95%*	*Upper 95%*	*Lower 95.0%*	*Upper 95.0%*
Intercept	6.824775802	0.0221354	308.3189126	9.97E-16	6.7724338	6.87711781	6.772433796	6.877117808
LN(τ/τ_{max})	-0.33345626	0.0794651	-4.19626236	0.004054	-0.5213613	-0.1455512	-0.52136128	-0.14555124
RESIDUAL OUTPUT								
Observation	*Predicted Y*	*Residuals*	*Std Residuals*					
1	6.903893116	0.066837	1.977359537					
2	6.867554407	-0.0079395	-0.23488879					
3	6.824775802	-0.0201613	-0.5964679					
4	6.957967463	0.0313678	0.92801082					
5	6.903832506	0.0045226	0.133800108					
6	6.853435428	-0.0268902	-0.79554188					
7	6.99181766	-0.0458037	-1.35509331					
8	6.943217523	-0.0146797	-0.43429644					
9	6.877862116	0.012747	0.377117838					

APPENDIX A-16 REGRESSION SUMMARY OUTPUT OF LN(COOLING RATE) (°C/S) AS A FUNCTION OF LN(SWE/MAX SWE)

Table A-15 Regression Summary Output of ln(Cooling Rate) (°C/s) as a Function of ln(SWE/max SWE)

SUMMARY OUTPUT			Ln(Cooling Rate ΔT_{8-5}) (°C/s)						
Regression Statistics									
Multiple R	0.950730563								
R Square	0.903888603								
Adj R Square	0.890158404								
Std Error	0.135106514								
Observations	9								
ANOVA									
	df	*SS*	*MS*	*F*	*Sig F*				
Regression	1	1.201685	1.201684989	65.832154	8.3286E-05				
Residual	7	0.1277764	0.01825377						
Total	8	1.3294614							
	Coefficients	*Std Error*	*t Stat*	*P-value*	*Lower 95%*	*Upper 95%*	*Lower 95.0%*	*Upper 95.0%*	
Intercept	3.112908552	0.0854299	36.43814664	3.046E-09	2.91089885	3.31491825	2.910898852	3.31491825	
Ln(WE/WE$_{max}$)	-1.024958147	0.1263244	-8.113701591	8.329E-05	-1.3236678	-0.7262485	-1.323667788	-0.7262485	

RESIDUAL OUTPUT

Observation	Predicted Y	Residuals	Std Residuals
1	3.366226172	-0.172463	-1.364632601
2	3.964977248	-0.100675	-0.79660171
3	4.249071666	-0.0894076	-0.707447646
4	3.23757462	-0.0577307	-0.456800639
5	3.781624639	0.0496394	0.392777164
6	4.042301848	-0.0219717	-0.173853245
7	3.112908552	0.086866	0.68733666
8	3.673971176	0.0545376	0.431534385
9	3.888670354	0.2512051	1.987687632

APPENDIX A-17 REGRESSION OUTPUT SUMMARY OF LN(COOLING RATE) (°C/S) AS A FUNCTION OF LN(SPINDLE TORQUE/MAX SPINDLE TORQUE)

Table A-16 Regression Output Summary of ln(Cooling Rate) (°C/s) as a Function of ln(Spindle Torque/max Spindle Torque)

SUMMARY OUTPUT				Ln(Cooling Rate)$\Delta T_{8\text{-}5}$ (°C/s)					
Regression Statistics									
Multiple R	0.80605832								
R Square	0.64973001								
Adj R Square	0.59969144								
Std Error	0.25792314								
Observations	9								
ANOVA									
	df	SS	MS	F	Sig F				
Regression	1	0.86379096	0.863790959	12.9845841	0.008700165				
Residual	7	0.46567042	0.066524346						
Total	8	1.32946138							
	Coefficients	Std Error	t Stat	P-value	Lower 95%	Upper 95%	Lower 95.0%	Upper 95.0%	
Intercept	4.17958824	0.15799797	26.45343081	2.8246E-08	3.805982418	4.553194058	3.805982418	4.553194058	
Ln(τ/τmax)	2.04387126	0.5672043	3.603412835	0.00870017	0.702646213	3.385096306	0.702646213	3.385096306	

RESIDUAL OUTPUT			
Observation	Predicted Y	Residuals	Std Residuals
1	3.69465027	-0.50088714	-2.076087011
2	3.91738305	-0.05308078	-0.220010277
3	4.17958824	-0.01992421	-0.082582262
4	3.36320949	-0.18336559	-0.760017358
5	3.69502176	0.13624228	0.564699702
6	4.00392326	0.01640692	0.068003711
7	3.15572967	0.04404488	0.182558107
8	3.45361708	0.27489166	1.13937643
9	3.85420346	0.28567199	1.184058958

APPENDIX A-18 REGRESSION OUTPUT SUMMARY OF LN(GRAIN SIZE) (μm) AS A FUNCTION OF LN(SPECIFIC WELD ENERGY)

Table A-17 Regression Output Summary of ln(Grain Size) (μm) as a Function of ln(Specific Weld Energy/max Specific Weld Energy)

SUMMARY OUTPUT			Ln(Grain Size) (μm)					
Regression Statistics								
Multiple R	0.82661021							
R Square	0.68328444							
Adj R Square	0.60410555							
Std Error	0.05211579							
Observations	6							
ANOVA								
	df	SS	MS	F	Sig F			
Regression	1	0.023438549	0.023438549	8.629629	0.042489632			
Residual	4	0.010864221	0.002716055					
Total	5	0.03430277						
	Coefficients	Std Error	t Stat	P-value	Lower 95%	Upper 95%	Lower 95.0%	Upper 95.0%
Intercept	1.83452389	0.034968255	52.46255164	7.9E-07	1.737436445	1.93161133	1.737436445	1.93161133
Ln(WE/WE$_{max}$)	0.17726525	0.060343089	2.937623008	0.04249	0.009725973	0.34480452	0.009725973	0.34480452
RESIDUAL OUTPUT								
Observation	Predicted Y	Residuals	Std Residuals					
1	1.79071292	-0.05200267	-1.115607247					
2	1.68715966	0.017588437	0.377322715					
3	1.81296304	0.049565498	1.063322924					
4	1.71887026	0.052686499	1.130277409					
5	1.67378646	-0.04650863	-0.997744312					
6	1.83452389	-0.02132914	-0.457571488					

169

APPENDIX A-19 REGRESSION OUTPUT SUMMARY OF LN(GRAIN SIZE) (μm) AS A FUNCTION OF LN(TORQUE/ MAX TORQUE)

Table A-18 Regression Output Summary of ln(Grain Size) (μm) as a Function of ln(Torque/ max Torque)

SUMMARY OUTPUT				Ln(Grain Size) (μm)				
Regression Statistics								
Multiple R	0.88075136							
R Square	0.77572296							
Adj R Square	0.7196537							
Std Error	0.0438558							
Observations	6							
ANOVA								
	df	SS	MS	F	Sig F			
Regression	1	0.026609446	0.026609446	13.83508	0.020482485			
Residual	4	0.007693324	0.001923331					
Total	5	0.03430277						
	Coefficients	Std Error	t Stat	P-value	Lower 95%	Upper 95%	Lower 95.0%	Upper 95.0%
Intercept	1.67081148	0.028440029	58.74858499	5.03E-07	1.591849302	1.749773663	1.5918493	1.749773663
$Ln(\tau/\tau_{max})$	-0.4594819	0.12353144	-3.71955438	0.020482	-0.80246017	-0.11650365	-0.8024602	-0.116503646
RESIDUAL OUTPUT								
Observation	Predicted Y	Residuals	Std Residuals					
1	1.74033902	-0.001628776	-0.041523071					
2	1.69026655	0.014481538	0.369183858					
3	1.8148501	0.047678442	1.215486261					
4	1.74025551	0.031301254	0.797975824					
5	1.67081148	-0.043533652	-1.10982142					
6	1.86149356	-0.048298806	-1.231301451					

APPENDIX A-20 REGRESSION OUTPUT SUMMARY OF LN(GRAIN SIZE/MAX GRAIN SIZE) (µm) AS A FUNCTION OF LN(CR/MAX CR)

Table A-19 Regression Output Summary of ln(Grain Size/max Grain Size) (µm) as a Function of ln(Cooling Rate/max Cooling Rate)

SUMMARY OUTPUT						ln(Grain Size/max Grain Size) (µm)			
Regression Statistics									
Multiple R	0.693265501								
R Square	0.480617054								
Adj R Square	0.307489406								
Std Error	0.058707493								
Observations	5								
ANOVA									
	_df_	_SS_	_MS_	_F_	_Sig F_				
Regression	1	0.00956797	0.00956797	2.776085	0.194272				
Residual	3	0.010339709	0.00344657						
Total	4	0.019907679							
	Coefficients	_Standard Error_	_t Stat_	_P-value_	_Lower 95%_	_Upper 95%_	_Lower 95.0%_	_Upper 95.0%_	
Intercept	-0.198085213	0.04785072	-4.139649615	0.025593	-0.350368	-0.0458	-0.3503676	-0.0458029	
ln(CR/max CR) (C/s)	-0.123943912	0.074389018	-1.666158732	0.194272	-0.360683	0.112795	-0.360683	0.11279514	

RESIDUAL OUTPUT					PROBABILITY OUTPUT		
Observation	_Predicted Grain Size_	_Residuals_	_Standard Residuals_		_Percentile_	_Grain Size_	
1	-0.078367676	-0.045450616	-0.893954892		10	-0.23525	
2	-0.161476921	0.003696473	0.072704853		30	-0.15778	
3	-0.157382034	0.066410256	1.306203934		50	-0.12382	
4	-0.18081563	-0.054435079	-1.070667686		70	-0.09097	
5	-0.079112756	0.029778966	0.58571379		90	-0.04933	

APPENDIX B

APPENDIX B-1 PHOTOGRAPHS OF ISO-THERMAL UNIAXIAL HOT COMPRESSION TEST SPECIMENS AFTER TESTING
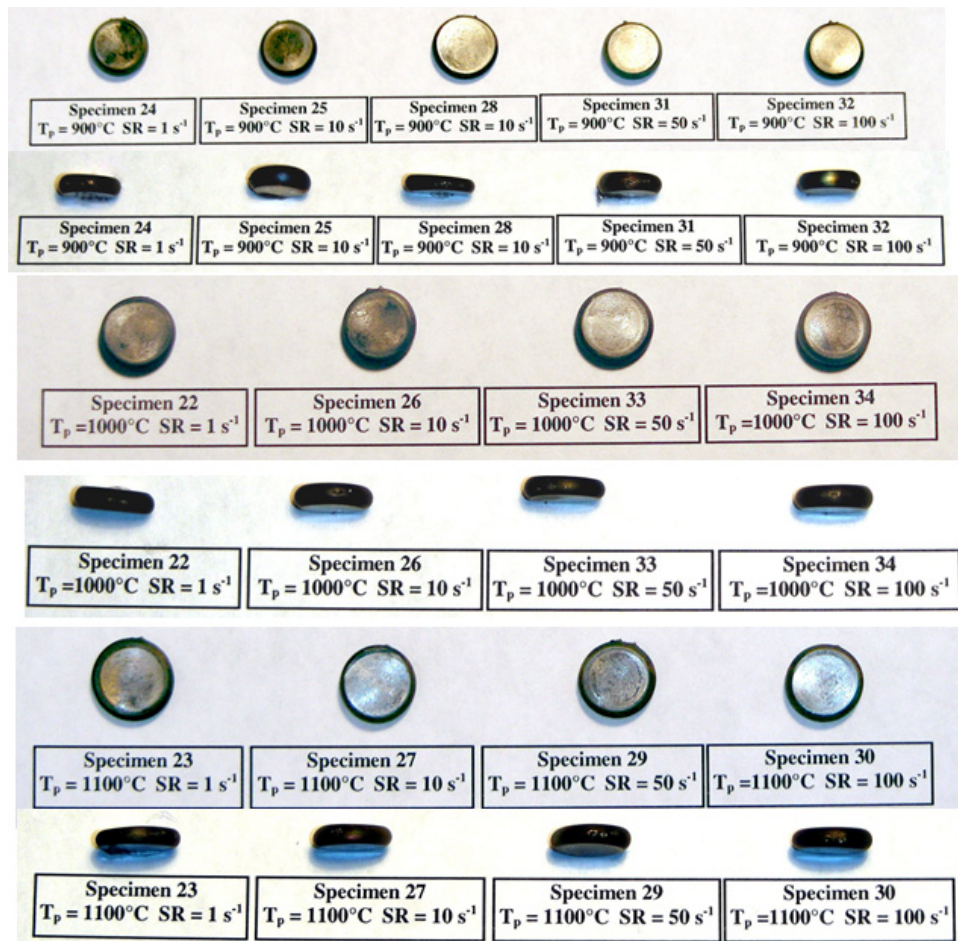
Figure B- 1 Photographs of iso-thermal uniaxial hot compression test specimens after testing.

APPENDIX B-2 LIST OF SHAPE COEFFICIENTS FOR COMPRESSION TEST SPECIMENS

Table B-1 List of Shape Coefficients for Compression Test Specimens

Temperature(^{o}C) _Stain Rate (1/s)	Aspect Ratio	Barrelling Coefficient (B)	Ovality Coefficient (Ov)	Height Coefficient (H)
900_1	1.103	1.0919	1.014	0.046
900_10	1.132	1.0785	1.009	0.030
900_50	1.094	1.1137	1.008	0.042
900_100	1.095	1.0945	1.005	0.031
1000_1	1.104	1.0963	1.017	0.013
1000_10	1.103	1.1436	1.026	0.008
1000_50	1.102	1.1004	1.019	0.048
1000_100	1.103	1.1123	1.022	0.051
1100_1	1.104	1.0856	1.024	0.014
1100_10	1.112	1.0883	1.009	0.032
1100_50	1.103	1.0997	1.018	0.031
1100_100	1.106	1.0984	1.019	0.031

Notes:
- Shaded rows correspond to invalid test data as determined by the criteria listed below for shape coefficients:
- Criteria for valid test:
  - B< 1.10
    - B is the barreling coefficient. It is the ratio of the final volume of the test piece divided by the initial volume. Barreling is caused by friction at the interfaces.
  - H < 0.04
    - H is the height coefficient. It is an indication of the parallelism of the test piece (i.e., uniformity of deformation during compression).

APPENDIX B-3 REGRESSION OUTPUT SUMMARY OF PEAK STRAIN AT ONSET OF DRX AS A FUNCTION OF TEMPERATURE AND STRAIN RATE

Table B-2 Regression Output Summary of Peak Strain at Onset of DRX as a Function of Temperature and Strain Rate

SUMMARY OUTPUT			Peak Strain (in/in)					
Regression Statistics								
Multiple R	0.210615218							
R Square	0.04435877							
Adj R Square	-0.59273538							
Std Error	0.091950602							
Observations	6							
ANOVA								
	df	*SS*	*MS*	*F*	*Sig F*			
Regression	2	0.001177376	0.000588688	0.069627	0.93420528			
Residual	3	0.025364739	0.008454913					
Total	5	0.026542115						
	Coefficients	*Std Error*	*t Stat*	*P-value*	*Lower 95%*	*Upper 95%*	*Lower 95.0%*	*Upper 95.0%*
Intercept	0.340328456	0.431282394	0.78910816	0.487664	-1.032204605	1.712861518	-1.032204605	1.712861518
Temperature (°C)	5.68482E-05	0.000418305	0.135901407	0.900506	-0.001274384	0.00138808	-0.001274384	0.00138808
Strain Rate (in/in)	-0.00035201	0.001019722	-0.345206353	0.752726	-0.003597224	0.002893195	-0.003597224	0.002893195
RESIDUAL OUTPUT								
Observation	*Predicted Y*	*Residuals*	*Std Residuals*					
1	0.387971671	0.009128329	0.128162535					
2	0.356290373	-0.006890373	-0.096741439					
3	0.379575912	-0.004475912	-0.062842191					
4	0.399341306	-0.078441306	-1.101322765					
5	0.385260729	0.129239271	1.814530606					
6	0.367660008	-0.048560008	-0.681786745					

APPENDIX B-4 REGRESSION OUTPUT SUMMARY OF PEAK STRESS AS A FUNCTION OF TEMPERATURE AND STRAIN RATE

Table B-3 Regression Output Summary of Peak Stress as a Function of Temperature and Strain Rate

SUMMARY OUTPUT			Peak Stress (MPa)					
Regression Statistics								
Multiple R	0.96491591							
R Square	0.93106271							
Adjusted R Square	0.88510452							
Standard Error	25.8163031							
Observations	6							
ANOVA								
	df	*SS*	*MS*	*F*	*Sig F*			
Regression	2	27004.37	13502.18678	20.25891	0.018100113			
Residual	3	1999.445	666.4815059					
Total	5	29003.82						
	Coefficients	*Std Error*	*t Stat*	*P-value*	*Lower 95%*	*Upper 95%*	*Lower 95.0%*	*Upper 95.0%*
Intercept	926.797243	121.088	7.653913108	0.004632	541.4410967	1312.15339	541.441097	1312.15339
Temperature (°C)	-0.7169568	0.117444	-6.10465244	0.008832	-1.09071711	-0.3431965	-1.09071711	-0.343196547
Strain Rate (in/in)	0.48675997	0.2863	1.700175299	0.187657	-0.424374	1.39789393	-0.424374	1.397893928
RESIDUAL OUTPUT								
Observation	*Predicted Y*	*Residuals*	*Std Residuals*					
1	286.403698	23.5963	1.179978973					
2	330.212095	-21.0121	-1.050750678					
3	234.178414	-5.16841	-0.25845659					
4	143.012332	-21.0123	-1.050762554					
5	162.482731	0.517269	0.025867036					
6	186.820729	23.07927	1.154123813					

APPENDIX B-5 REGRESSION OUTPUT SUMMARY OF PEAK STRESS AS A FUNCTION OF TEMPERATURE

Table B-4 Regression Output Summary of Peak Stress as a Function of Temperature

SUMMARY OUTPUT			Peak Stress (MPa)						
Regression Statistics									
Multiple R	0.9298599								
R Square	0.86463943								
Adj R Square	0.83079929								
Std Error	31.328794								
Observations	6								
ANOVA									
	df	SS	MS	F	Sig F				
Regression	1	25077.84476	25077.84476	25.550703	0.007207				
Residual	4	3925.973324	981.493331						
Total	5	29003.81808							
	Coefficients	Std Error	t Stat	P-value	Lower 95%	Upper 95%	Lower 95.0%	Upper 95.0%	
Intercept	956.17069	145.4402747	6.574318506	0.0027705	552.3638	1359.97763	552.363751	1359.97763	
Temperature (°C)	-0.7203138	0.142501784	-5.054770337	0.0072069	-1.11596	-0.3246654	-1.1159622	-0.3246654	
RESIDUAL OUTPUT									
Observation	Predicted Y	Residuals	Std Residuals						
1	307.888276	2.111724138	0.075361323						
2	307.888276	1.311724138	0.046811638						
3	235.856897	-6.846896552	-0.244345923						
4	163.825517	-41.82551724	-1.492631664						
5	163.825517	-0.825517241	-0.029460321						
6	163.825517	46.07448276	1.644264947						

APPENDIX B-6 REGRESSION OUTPUT SUMMARY OF GRAIN SIZE AS A FUNCTION OF TEMPERATURE AND STRAIN RATE

Table B- 5 Regression Output Summary of Grain Size as a Function of Temperature and Strain Rate

SUMMARY OUTPUT	Grain Size (µm)							
Regression Statistics								
Multiple R	0.999574503							
R Square	0.999149187							
Adjusted R Square	0.99744756							
Standard Error	0.085							
Observations	4							
ANOVA								
	df	*SS*	*MS*	*F*	*Sig F*			
Regression	2	8.48465	4.242325	587.173	0.0291687			
Residual	1	0.007225	0.007225					
Total	3	8.491875						
	Coefficients	*Std Error*	*t Stat*	*P-value*	*Lower 95%*	*Upper 95%*	*Lower 95.0%*	*Upper 95.0%*
Intercept	-10.59055556	0.430266749	-24.6139298	0.02585	-16.057613	-5.12349815	-16.057613	-5.12349815
Temperature (°C)	0.014225	0.000425	33.47058824	0.019015	0.0088249	0.01962514	0.00882486	0.019625137
Strain Rate (1/s)	-0.006944444	0.000944444	-7.352941176	0.086052	-0.0189447	0.00505586	-0.01894475	0.00505586
RESIDUAL OUTPUT								
Observation	*Predicted Y*	*Residuals*	*Std Residuals*					
1	2.1425	-0.0425	-0.866025404					
2	1.5175	0.0425	0.866025404					
3	4.9875	0.0425	0.866025404					
4	4.3625	-0.0425	-0.866025404					

APPENDIX B-7 REGRESSION OUTPUT SUMMARY OF GRAIN SIZE AS A FUNCTION OF TEMPERATURE

Table B- 6 Regression Output Summary of Grain Size as a Function of Temperature

SUMMARY OUTPUT		Grain Size (μm)							
Regression Statistics									
Multiple R	0.976293672								
R Square	0.953149334								
Adj R Square	0.929724001								
Standard Error	0.44601009								
Observations	4								
ANOVA									
	df	*SS*	*MS*	*F*	*Sig F*				
Regression	1	8.094025	8.094025	40.68882745	0.023706328				
Residual	2	0.39785	0.198925						
Total	3	8.491875							
	Coefficients	*Std Error*	*t Stat*	*P-value*	*Lower 95%*	*Upper 95%*	*Lower 95.0%*	*Upper 95.0%*	
Intercept	-10.9725	2.241172963	-4.895873804	0.03927797	-20.61548897	-1.329511033	-20.61548897	-1.329511033	
Temperature (°C)	0.014225	0.00223005	6.378779464	0.023706328	0.004629867	0.023820133	0.004629867	0.023820133	
RESIDUAL OUTPUT									
Observation	*Predicted Y*	*Residuals*	*Std Residuals*						
1	1.83	0.27	0.741420706						
2	1.83	-0.27	-0.741420706						
3	4.675	0.355	0.974830928						
4	4.675	-0.355	-0.974830928						

APPENDIX B-8 REGRESSION OUTPUT SUMMARY OF COMPRESSION TEST

Table B-7 Regression Output Summary of Compression Test Specimen Average Hardness as a Function of Temperature and Strain Rate

Stepwise Fit for Hardness

Stepwise Regression Control

Stopping Rule: Minimum BIC   → Enter All Make Model

Direction: Backward ▾   ← Remove All Run Model

Rules: Combine ▾

Go   Stop   Step

SSE	DFE	RMSE	RSquare	RSquare Adj	Cp	p	AICc	BIC
4837.3713	12	20.077706	0.6356	0.5749	2.0086233	3	141.2093	140.0415

Current Estimates

Lock	Entered	Parameter	Estimate	nDF	SS	"F Ratio"	"Prob>F"
☑	☑	Intercept	433.833963	1	0	0.000	1
☐	☑	Temp	-0.242	1	5856.4	14.528	0.00248
☐	☑	Strain Rate	0.34056017	1	2580.629	6.402	0.02641
☐	☐	(Temp-1000)*(Temp-1000)	0	1	388.8	0.961	0.34791
☐	☐	(Temp-1000)*(Strain Rate-32.2)	0	1	492.3988	1.247	0.288
☐	☐	(Strain Rate-32.2)*(Strain Rate-32.2)	0	1	1.423523	0.003	0.95564

Summary of Fit

RSquare	0.635586
RSquare Adj	0.574851
Root Mean Square Error	20.07771
Mean of Response	202.8
Observations (or Sum Wgts)	15

Analysis of Variance

Source	DF	Sum of Squares	Mean Square	F Ratio
Model	2	8437.029	4218.51	10.4648
Error	12	4837.371	403.11	Prob > F
C. Total	14	13274.400		0.0023*

Parameter Estimates

Term	Estimate	Std Error	t Ratio	Prob>|t|
Intercept	433.83396	63.84984	6.79	<.0001*
Temp	-0.242	0.063491	-3.81	0.0025*
Strain Rate	0.3405602	0.1346	2.53	0.0264*

APPENDIX C

APPENDIX C-1 LIST OF COMPRESSION SPECIMEN SHAPE COEFFICIENTS

Table C-1 List of Compression Shape Coefficients

Specimen	Barreling Coefficient	Ovality Coefficient	Length Coefficient	Circularity Coefficient
500 RPM, 2 IPM	1.06	1.01	0.01	0.00
300 RPM, 2 IPM	1.06	1.02	0.02	0.01

Notes:
- Criteria for valid test:
  - B< 1.10
    - B is the barreling coefficient. It is the ratio of the final volume of the test piece divided by the initial volume. Barreling is caused by friction at the interfaces.
  - H < 0.04
    - H is the height coefficient. It is an indication of the parallelism of the test piece (i.e., uniformity of deformation during compression).

APPENDIX C-2 REGRESSION OUTPUT SUMMARY OF LN(MEAN EXIT STATE VARIABLE/MAX STATE VARIABLE) TO LN(RPM/MAX RPM) AND (TS/MAX TS)

Table C-2 Regression Output Summary of ln(Mean Exit State Variable/max State Variable) to ln(RPM/max RPM) and (TS/max TS)

SUMMARY OUTPUT			Mean Exit State Variable					
Regression Statistics								
Multiple R	0.96195986							
R Square	0.92536676							
Adjusted R Square	0.90048902							
Standard Error	0.0244395							
Observations	9							
ANOVA								
	df	*SS*	*MS*	*F*	*Sig F*			
Regression	2	0.044434201	0.0222171	37.19657	0.00041572			
Residual	6	0.003583734	0.000597289					
Total	8	0.048017934						
	Coefficients	Std Error	t Stat	P-value	Lower 95%	Upper 95%	Lower 95.0%	Upper 95.0%
Intercept	-5.6251239	0.015436875	-364.395258	2.88E-14	-5.6628966	-5.5873512	-5.66289658	-5.58735123
LN(RPS/ Max PRS)	-0.311159	0.03896024	-7.9865778	0.000205	-0.4064913	-0.2158267	-0.40649126	-0.21582672
LN(TS/Max TS)	0.05849323	0.017959521	3.2569482	0.017315	0.01454786	0.10243859	0.014547865	0.102438595
RESIDUAL OUTPUT								
Observation	*Predicted Y*	*Residuals*	*Std Residuals*					
1	-5.5304373	0.033668996	1.590769622					
2	-5.4898929	-0.00687542	-0.32484516					
3	-5.4661759	-0.03059238	-1.44540798					
4	-5.6199522	-0.00686927	-0.32455448					
5	-5.5794077	0.006653536	0.31436168					
6	-5.5556908	0.008912058	0.421070809					
7	-5.6893853	-0.02444752	-1.15507979					
8	-5.6488409	-0.00615144	-0.29063903					
9	-5.6251239	0.025701447	1.21432432					